FORMATION AND STABILITY OF NH_4TiOF_3 MESOCRYSTALS

LIU YANQIONG

(*B.Sc. (Hons.), NUS*)

A THESIS SUBMITTED

FOR THE DEGREE OF DOCTOR OF PHILOSOPHY

DEPARTMENT OF MATERIALS SCIENCE AND ENGINEERING

NATIONAL UNIVERSITY OF SINGAPORE

2013

DECLARATION

I hereby declare that the thesis is my original work and it has been written by me in its entirety. I have duly acknowledged all the sources of information which have been used in the thesis.

This thesis has also not been submitted for any degree in any university previously.

_____

Liu Yanqiong

18 December 2012

ACKNOWLEDGEMENTS

First and foremost, I would like to express my heartfelt appreciation and gratitude to my supervisor Professor John Wang for his enormous support, patient guidance, infinite understanding, and kind encouragement along this wonderful journey. I have been inspired by his dedication to research and passion for life.

A special word of gratitude goes to Professor Fred Lange. He was a great supervisor in terms of knowledge, experiences in research, and techniques for supervising. He taught me to approach scientific problems from known knowledge rather than blind experimental work.

I would like to thank Dr Tun Seng Herng for his invaluable inspiration and advices on my research. I also thank my collaborators: Professor Zeng Kaiyang and Dr Amit Kumar from the Department of Mechanical Engineering, Fan Zhen (Advanced Ceramics Lab) and Dr Khuong Phuong Ong from Institute of High Performance Computing.

I am indebted to all former and current members of the Advanced Ceramics Lab: Dr Zhang Yu, Dr Happy Tan, Ms Sim Chow Hong, Ms Fransiska Cecilia Kartawidjaja, Ms Zheng Rongyan, Ms Serene Ng, Dr Wang Yang, Dr Wu Jiagang,

Ms Ke Qingqing, Ms Li Hui, Mr Liu Huajun, Mr Yang Zhengchun, Mr Kang Guangqing, Mr Fan Zhen, Mr Hsu You Wei Benedict, and Mr Ho Kuan-Hung for their support, discussions, and friendship during this memorable journey.

I also wish to convey my appreciation for the laboratory supporting staff from the Department of Materials Science and Engineering: Dr Zhang Jixuan, Ms Serene Chooi, Ms Agnes Lim, Mr Chen Qun, Mr Chan Yew Weng, Mr Henche Kuan, and Ms He Jian. They have assisted me with kind technical support and provided me with adequate information.

Last but not least, I thank my husband, parents, and parents-in-law for their unconditional love and prayers along the way. I'm thankful for all the people I got to know and I thank God for giving me this great opportunity and bringing me through such a wonderful yet challenging journey.

TABLE OF CONTENTS

SUMMARY

In chapter 1, a brief introduction is given to NH_4TiOF_3 mesocrystals and the background of this project. It is shown that mesocrystals are a new class of crystals with interesting structure different from either single crystals or polycrystals. The compound NH_4TiOF_3 is promising as it can convert to the versatile and well-studied materialTiO_2 (anatase). Therefore, it will be interesting to study NH_4TiOF_3 mesocrystals as an example to explore factors affecting formation and properties of mesocrystals. Chapter 2 provides a brief description on the experimental procedures and characterization techniques employed in this project.

In Chapter 3, an investigation is conducted into the growth and anisotropic dissolution of NH_4TiOF_3 mesocrystals, which are shown to partially convert to anatase TiO_2 in an aqueous environment. There is a driving force for the dissolution of the mesocrystal, whereby the metastable NH_4TiOF_3 is converted to stable TiO_2 by losing N and F elements. An anisotropic propagation of dissolution is observed with preferential dissolution in [100] and [010] directions in {001} planes.

In Chapter 4, with the understanding that metastable NH_4TiOF_3 tends to convert to stable TiO_2, the parameters affecting this conversion process were studied, including temperature, presence of surfactant Brij 58 (23 %), and solution pH. Surfactant (Brij 58) molecules appear to facilitate the mesoscale assembly of NH_4TiOF_3 nanocrystals into NH_4TiOF_3 mesocrystals via the interaction of their hydrophobic tails. Raising temperature and increasing solution pH enhance the conversion rate of NH_4TiOF_3 nanocrystals into TiO_2 (anatase) nanoparticles.

In Chapter 5, an investigation is conducted into the contribution from hydrophobicity of surfactant to the formation of NH_4TiOF_3 mesocrystals. The surfactant introduced is a tri-block copolymer F127 (EO_{106}-PO_{70}-EO_{106}) instead of Brij 58 ($C_{16}EO_{20}$). The hydrophobicity of the adsorbed F127 molecules is drastically dependent on the surfactant concentration. Therefore, the formation of NH_4TiOF_3 mesocrystals can be largely manipulated by controlling the colloidal and chemical stabilities of NH_4TiOF_3 nanoparticles as the building blocks by altering the concentration of F127.

In Chapter 6, it is detailed that NH_4TiOF_3 mesocrystals are able to form in the absence of surfactants and in the presence of water-miscible short length organic molecules. To understand this interesting phenomenon, an intrinsic behavior, i.e. ferroelectricity, of NH_4TiOF_3 mesocrystals is further investigated. It is conducted by both computational study and experimental confirmation, where the ferroelectricity of NH_4TiOF_3 mesocrystals is shown by the piezoelectric force microscopy (PFM) technique. The results suggest that spontaneous dipoles arising from ferroelectricity can also contribute to the attractive interparticle forces among the NH_4TiOF_3 nanocrystals and lead to the formation of NH_4TiOF_3 mesocrystals.

The conclusions of this project are summarized in Chapter 7, together with the future works that may be conducted listed in Chapter 8.

LIST OF FIGURES

LIT OF TABLES

LIST OF PUBLICATIONS

1. Yanqiong Liu, Amit Kumar, Zhen Fan, Zhang Yu, Ke Qingqing, Kaiyang Zeng, John Wang, David J. Singh, Khuong Phuong Ong, "Ferroelectricity and Dipole-Dipole Interactions in NH_4TiOF_3 Mesocrystals", accepted by ***Applied Physical Letters***.

2. Yanqiong Liu, Yu Zhang, and John Wang, "From NH4TiOF3 Nanoparticles to NH_4TiOF_3 Mesocrystals: Steric Hindrance versus Hydrophobic Attraction of F127 Molecules", ***CrystEngComm***, 2013, *15*, 791-801.

3. Yanqiong Liu, Yu Zhang, Hui Li, and John Wang, "Manipulating the Formation of NH_4TiOF_3 Mesocrystals: Effects of Temperature, Surfactant, and pH", ***Crystal Growth & Design***, 2012, *12*, 2625-2633

4. Yu Zhang, Hui Li, Yanqiong Liu, and John Wang, "Sonochemical Synthesis and Liquid Crystal Assembly of PS-b-PEO/Titania Aggregates", ***ChemComm***, 2012, *48*, 8538-8540.

5. Yanqiong Liu, Yu Zhang, Happy Tan, and John Wang, "Formation and anisotropic dissolution behavior of NH_4TiOF_3 Mesocrystals", ***Crystal Growth & Design***, 2011, *11*, 2905-2912

6. Yu Zhang, Happy Tan, Hui Li, Yanqiong Liu, Fransiska C. Kartawidjaja, Zheng-Chun Yang, and John Wang, "Hybrid Titania Microspheres of Novel Superstructures Templated by Block Copolymers", ***Chemistry of Materials***, 2011, *23*, 2745–2752

7. Yanqiong Liu and John Wang, "Co-sensitization of TiO_2 by PbS quantum dots and dye N719 in dye-sensitized solar cells", ***Thin Solid Films***, 2010, *518*, e54-e56

CHAPTER 1. INTRODUCTION

1.1 Concept of Mesocrystals

The word *mesocrystal* is an abbreviation for *mesoscopically structured crystal*. The first observation of mesocrystal dates back to 1969 when Petres et al. deduced a porous intermediate structure of $BaSO_4$.[1] In 2003, Colfen and Mann further stated that *mesoscale assembly* of nanocrystals contributed another mechanism for growing single crystals (Figure 1.1).[2] In such a mesoscale assembly process, the crystallized primary nanoparticles are aligned in all crystallographic directions to form "iso-oriented" crystals. This is in sharp contrast to the *classical crystallization* process whereby the crystallized primary nanoparticles grow by ion-by-ion attachment to achieve an amplified single crystal. Later Colfen and Antonietti proposed that mesocrystals are kinetically metastable intermediates, whereby the primary units can still be identified, in a crystallization reaction process, leading to single crystals with typical defects and inclusions.[3] In 2010, Song and Colfen gave a more precise definition that mesocrystals are 3D superstructured crystals consisting of mesoscopically scaled (1-100 nm) crystalline subunitsthat are aligned in a crystallogrpahic register.[4] The 3D mutual order of the subunits may impose difficulty in distinguishing a mesocrystal from a single crystal due to identical diffraction patterns in Transmission Electron Microscopy (TEM), behaviors in polarized light and many other behavior characteristic of single crystals.[3, 5, 6] The coherence length in scattering obtained from X-ray Diffraction (XRD) may be used to set up the borderline between mesocrystals and single crystals. The coherence length of single

crystals is usually bigger than 100 nm, while that of mesocrystals is typically smaller. The *crystalline subunits* in mesocrystals are often interspaced by organic additives, pores, or a second phase such as amorphous matter. This suggests that microscope imaging could be employed to differentiate between mesocrystals and single crystals. However, if the surface of the constituting nanocrystals is not sufficiently stablized, a mesocrystal will readily transform to a single crystal via a crystallographic fusion process. The significant difference between the architectures of mesocrystals and single crystals however reveals that the formation mechanism of mesocrystals is completely different from the classical crystal growth that leads to single crystals.

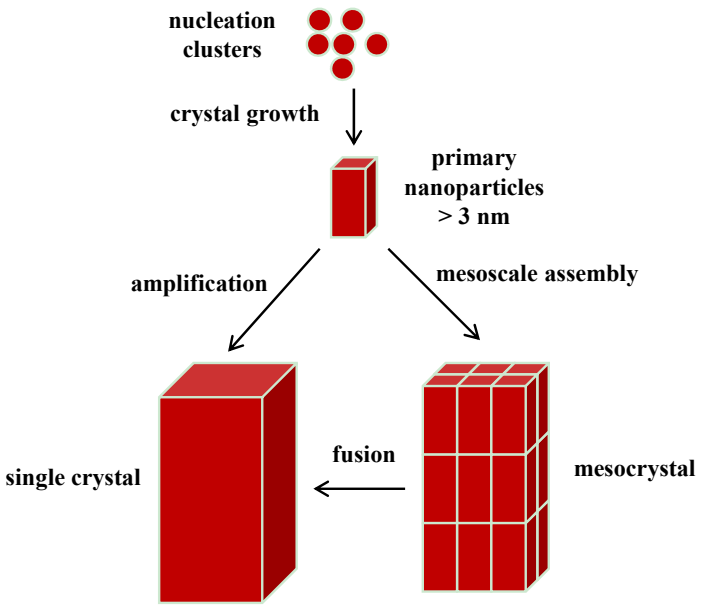

Figure 1.1 Alternative mechanisms of growth for single crystals.

1.2 Formation Mechanisms of Mesocrystals

Without crystallization, precursor ions condense without periodic arrangements on the atomic scale and form amorphous solids (Figure 1.2). In contrary, crystallization

refers to a process whereby the atoms are arranged periodically. Crystalline matericals include polycrystals, single crystals and mesocrystals. In polycrystals, the patches where the atoms are periodically arranged are not crystallographically aligned. In single crystals, the atoms are arranged periodically throughout the whole crystal except some minor random defects. For mesocrystals, the patches where the atoms are periodically arranged are crystallographically aligned but inter-spaced by impurities or defects, e.g. organic occlusions, solvent, amorphous counterparts, voids, etc. Classically, crystallization starts from clustering of the *primary building blocks*, such as atoms, ions or molecules. If the cluster reaches a critical size, further growth via ion-by-ion attachment will lead to unit cell replication and consequently growth of single crystals. This process is shown in Figure 1.2 by the route *precursor ions -> nanocrystal -> single crystal*. If the clusters randomly aggregate without crystallographic alignment, polycrystals are resulted. This is shown in Figure 1.2 by the route *precursor ions -> nanocrystal -> polycrystal*. Non-classically, crystal growth proceeds typically via the integration of classically crystallized subunits, which could be completely covered, partially covered or not covered at all by organic molecules (nanocrystals 1, 2, 3 in Figure 1.3, and nanocrystals in Figure 1.2, respectively). The integration process is called *oriented attachment* or *mesoscale assembly*. Oriented attachment is widely observed in 1D or 2D materials. Mesoscale assembly also proceeds via oriented attachment and usually leads to 3D hierarchically structured mesocrystals.

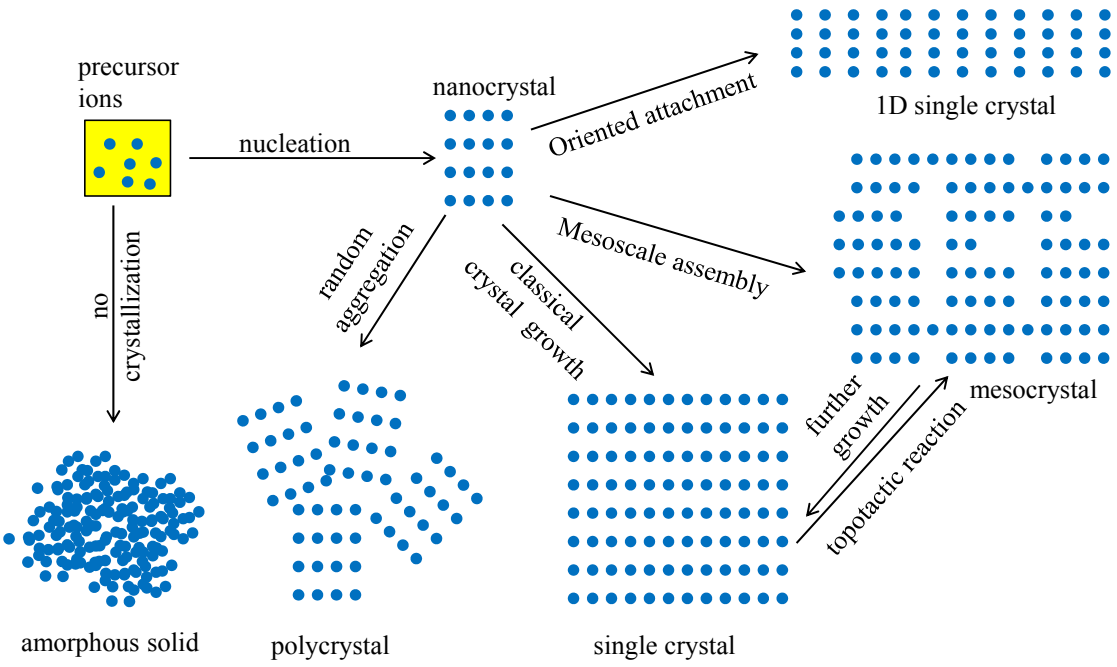

Figure 1.2 Schematic illustration of different possible formation mechanisms of various solids in the absence of organic additives.

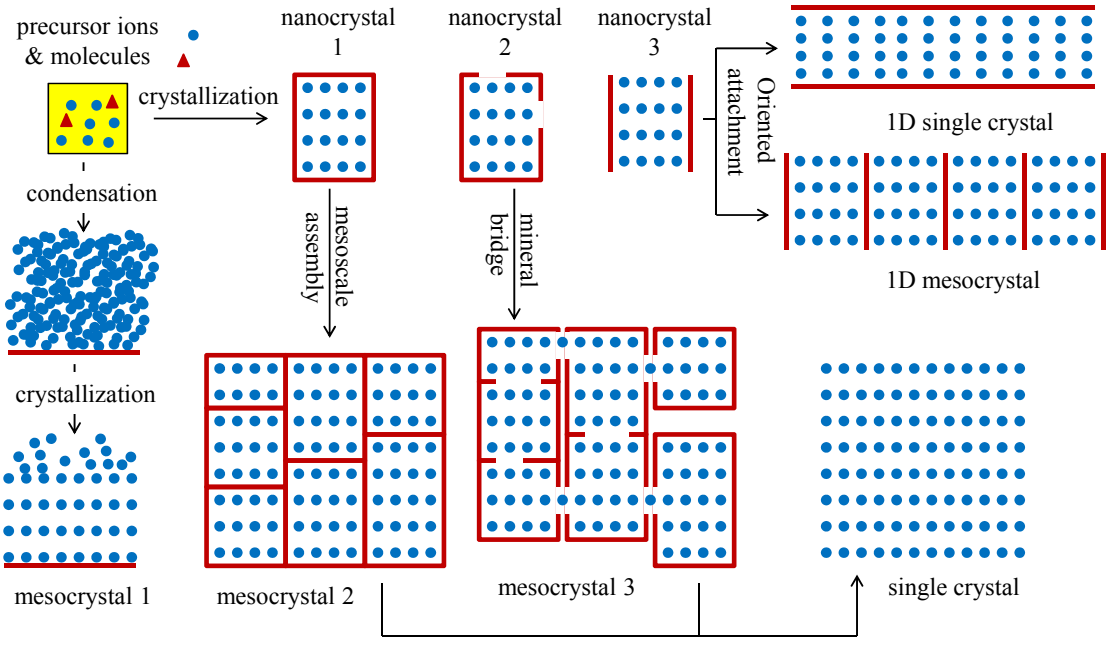

Figure 1.3 Schematic illustration of different possible formation mechanisms of various solids in the presence of organic additives.

Figure 1.4 shows the three possible routes from nanocrystals to microparticles. (a) **Ostwald ripening**. If the nanocrystal reaches a critical size, further growth via ion-by-ion attachment will lead to unit cell replication and consequently crystal growth. Otherwise, the nanocrystal will disintegrate, i.e. dissolve back into the solution, and the dissolved ions will contribute to growth of the larger nanocrystals which have reached the critical size. This is a typical process whereby the larger nanocrystals grow at the expenses of the smaller ones due to the thermodynamic driving force. (b) **Cluster-cluster random aggregation**. Nanocrystals are highly unstable due to high surface/volume ratio and random aggregation effectively relieves the high surface energy. However, in the resultant aggregates, interfaces between non-aligned nanocrystals give rise to relatively high interfacial energy. (c) **Oriented attachment.** The nanocrystals can attach to each other in an oriented manner such that all nanocrystals are crystallographically aligned. The resultant structure may undergo a crystallographic fusion and restructuring process at the boundary to form single crystals in the case whereby no organic additives are strongly attached at the interfaces.

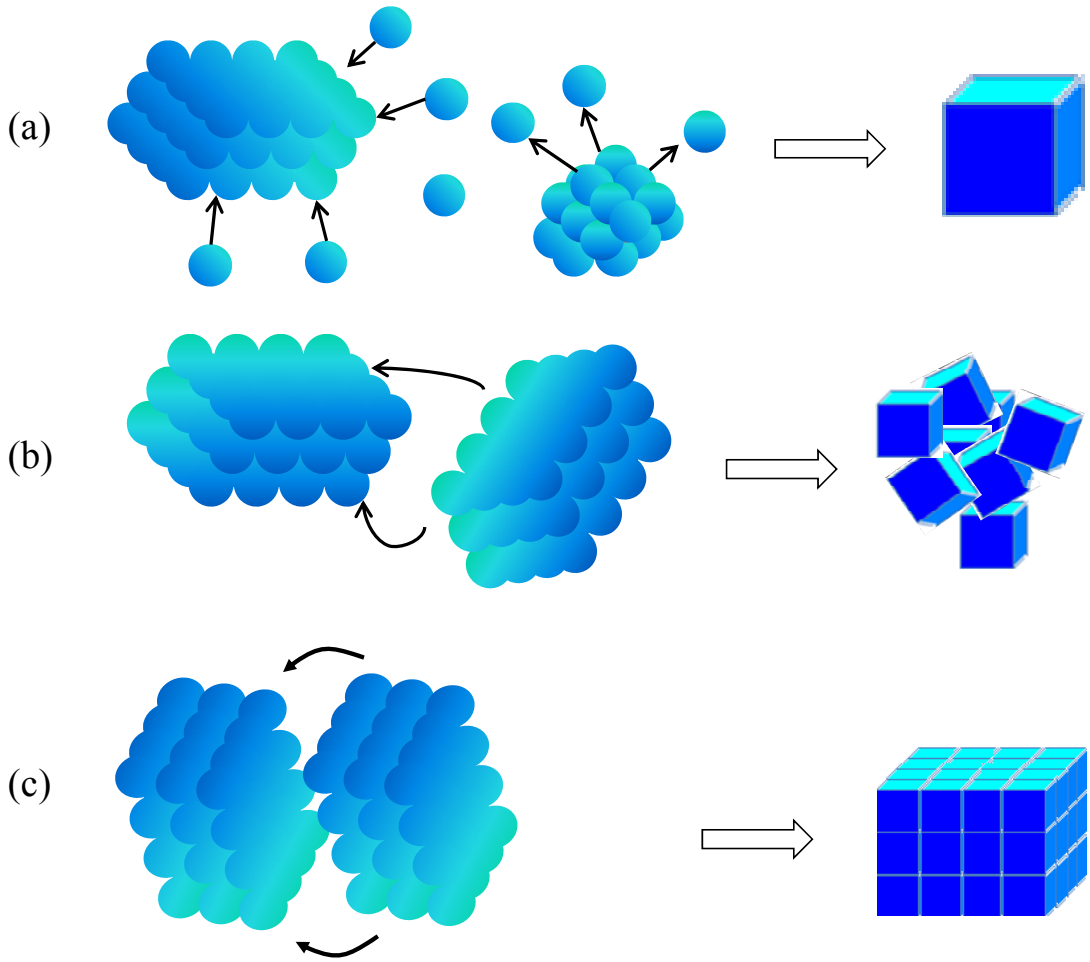

Figure 1.4 Three possible routes from nanocrystals to microparticles. (a) Ostwald ripening, (b) Cluster-cluster random aggregation, (c) Oriented attachment.

1.2.1 Interparticle Forces

In order to realize the directional aggregation of oriented attachment, various mechanisms have been reported. First of all, the mechanisms of colloidal stabilization shed light on manipulating the interaction among nanocrystals. Interparticle forces among particles in aqueous solution include attractive *Van der Waals force* that exists essentially in all materials, repulsive *hydration/solvation force* caused by water or other water-interacting molecules adsorbed on the surfaces,

attractive or repulsive *electrostatic force* due to ions on the surfaces, and attractive *hydrophobic force* imposed by hydrophobic polymer chains that are anchored to the particle surfaces in an aqueous solution. The general colloidal stabilization strategies in aqueous solution include three categories as shown in Figure 1.5, namely, polymeric stabilization, electrostatic stabilization, and electrosteric stabilization. Understanding these strategies will definitely provide insights for modifying them to achieve oriented attachment of nanocrystals in colloidal systems. Successful modifications will also be discussed in detail for each of the strategies.

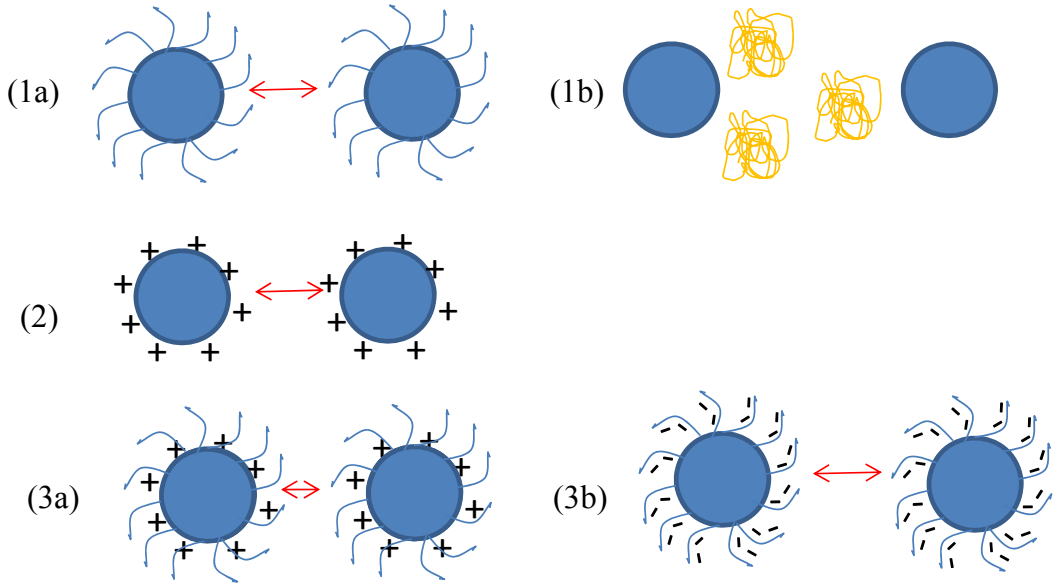

Figure 1.5 General colloidal stabilization methods in aqueous solution. (1) Polymeric stabilization: (1a) steric stabilization, (1b) depletion stabilization; (2) Electrostatic stabilization; (3) Electrosteric stabilization: (3a) charges and nonionic polymer, (3b) polyelectrolytes.

1.2.1.1 Polymeric Stabilization

Colloidal polymeric stabilization includes two general methods: steric stabilization and depletion stabilization.

Steric stabilization utilizes the steric hindrance of long dangling hydrophilic polymeric chains which are attached to the surfaces of nanocrystals so that the close contacts of the nanocrystals are hindered. This method hints that oriented attachment can be induced by the selective adsorption of hydrophilic polymers on certain crystallographic surfaces so that nanocrystals may aggregate via the exposed crystallographic surface. Examples for such polymers include double hydrophilic block copolymers (DHBCs) consisting of a hydrophilic block attached to inorganic minerals and another hydrophilic block that contributes to steric hindrance. Helices of $BaCO_3$ fibers with a diameter in the range of 200-500 nm and lengths as long as a few millimeters are formed in the presence of a DHBC (polyethylene glycol-b-[(2-[4-dihydroxyphosphoryl] -2-oxabutyl) acrylate ethyl ester]).[7] The helical $BaCO_3$ fibers are composed of nanocrystals with a diameter of ~30 nm and length of ~200 nm. The nanocrystals assemble towards helices because of the selective adsorption of the polymers on the (110) face of $BaCO_3$ nanocrystals. Very thin triangles, truncated triangular nanoprisms, and hexagons of Au were prepared by self-reduction of $HAuCl_4$ in the presence of a DHBC PEG-b-hexacyclen because of the specific adsorption of the polymer on (111) faces.[8] This was evidenced by molecular modeling that the span distance of the neighboring $–NH_2$ of PEG-b-hexacyclen matches well with the distance of the neighboring Au atoms in the (111) face. This is shown in Figure 1.3 by the route *precursor ions & molecules -> nanocrystal 3 -> 1D single crystal*. This method also hints that selective / preferential adsorption of hydrophobic chains anchored to certain crystallographic surfaces will drive oriented attachment at these crystallographic surfaces. For

example, $BaCrO_4$ chains and 2D superlattices have been prepared utilizing the hydrophobic tails of AOT molecules adsorbed specifically to the side surfaces of prismatic $BaCrO_4$ nanocrystals.[9] The distance in-between two neighboring $BaCrO_4$ nanocrystals is ~2 nm corresponding to the thickness of interdigitated surfactant layer. This is shown in Figure 1.3 by the route *precursor ions & molecules -> nanocrystal 3 -> 1D mesocrystal*.

Depletion stabilization makes use of the energy barrier that the free macromolecules need to overcome when they move to higher concentration regions to make way for the aggregating nanocrystals. However, when two particles have come so close that the region in between them is free of macromolecules, flocculation of these two particles is more favorable.[10] This stabilization method suggests that free macromolecules are not favored in the case of oriented attachment since precise control is not feasible.

1.2.1.2 Electrostatic Stabilization

Electrostatic stabilization operates via the electrostatic repulsion between net surface charges caused by ionization of surface atoms, binding of solution ions, ion exchange between surface and solution. A typical example is cetyltrimethylammonium bromide (CTAB $(C_{16}H_{33})N(CH_3)_3Br$) coated Au nanocrystals are stabilized by the bilayer structure of CTA^+ ions on the surfaces.[11] In accordance with this method, oriented attachment may be realized via selectively neutralizing some crystallographic faces of the electrostatically stabilized nanocrystals so that assembly can proceed via the neutralized crystallographic faces. For example, 3-mercaptopropionic acid molecules preferentially interdigitate the less

dense CTAB bilayer at the ends of Au nanorods and induce their end-to-end assembly at pH 9.6; whereas, 11-mercaptoundecanoic acid molecules can penetrate through the dense CTAB bilayer at the sides of Au nanorods and induce side-to-side assembly of Au nanorods at pH 6.2.[12] This is shown in Figure 1.3 by the route *precursor ions & molecules -> nanocrystal 3 -> 1D single crystal*. Another excellent example is the formation of pearl-like structure of anatase by controlling pH so that isoelectric point (IEP) of a certain crystallographic surface (i.e. (001)) is achieved and oriented attachment may continue via these surfaces.[13] This is shown in Figure 1.2 by the route *precursor ions -> nanocrystal -> 1D single crystal*. Oriented attachment may also be possible if the nanocrystals intrinsically consist of alternate layers of positively and negatively charged atoms in one crystallographic direction. A good example is the formation of ZnO nanorods after reflux of the starting sol that is composed of ZnO nanocrystals.[14] The atomic layers perpendicular to *c*-axis alternately consist of Zn^{2+} and O^{2-} ions.[15] This is shown in Figure 1.2 by the route *precursor ions -> nanocrystal -> mesocrystal*.

1.2.1.3 Electrosteric Stabilization

Electrosteric stabilization includes two general methods: (1) a combination of charges & nonionic polymers, and (2) polyelectrolytes. Charges and nonionic polymers are applied to impose both electrostatic stabilization by the surface charges and steric stabilization by the nonionic polymers which dangle in the solution. Modification of this stabilization method for realizing oriented attachment would be the selective adsorption of both charges and polymers on all the crystallographic surfaces except those surfaces that attachment is to occur. One typical example is the

growth of pearl-like TiO_2 necklaces by functionalization of preformed TiO_2 nanoparticles of 5 nm with a ligand $(HOCH_2)_3CNH_2$.[16] $(HOCH_2)_3CNH_2$ molecules bind to all surfaces except (001) because of their preferential desorption from (001) during reflux. The amino function is positively charged and imparts repulsive electrostatic force between adsorbed surfaces. Consequently, these bound $(HOCH_2)_3CNH_2$ molecules direct the assembly of the functionalized TiO_2 nanoparticles along the [001] axis. This is shown in Figure 1.2 by the route *precursor ions -> nanocrystal -> 1D single crystal*. Polyelectrolytes are ionic polymers which ionize in water to impose electrostatic stabilization and also dangle in water to act as steric barriers. Selective adsorption of polyelectrolytes on specific planes can also direct oriented attachment of nanocrystals. For example, poly(styrene-alt-maleic acid) molecules adsorb on positively charged calcite {001} faces leading to "surface stabilization and growth along *c*-axis direction".[17] This is shown in Figure 1.3 by the route *precursor ions & molecules -> nanocrystal 3 -> 1D mesocrystal*.

1.2.2 Physical Fields

Apart from the interference of additives discussed above, inherent properties such as electric dipoles and magnetic dipoles can also induce crystallographic alignment and thereby oriented attachment of nanocrystals if the interaction force is strong enough. For the cases whereby such interaction is nonexistent or not strong enough, external fields such as electric fields or magnetic fields can be applied to induce electric dipoles or magnetic dipoles and/or facilitate the crystallographic alignment process. The electric dipoles, magnetic dipoles, electric fields and magnetic fields have to be anisotropic with respect to the nanocrystals such that the latter can be

aligned crystallographically. These strategies can form either 1D single crystals or mesocrystals as shown by the two routes in Figure 1.2: *precursor ions -> nanocrystal -> 1D single crystal* and *precursor ions -> nanocrystal -> mesocrystal*.

1.2.2.1 Electric Dipoles

Electric dipoles can be a bulk property, for example, the spontaneous dipoles in ferroelectric materials such as $BaTiO_3$.[18] It is straightforward that directed aggregation of $BaTiO_3$ nanocrystals is easily observed.[19, 20] Electric dipoles can also be caused by alternating positively and negatively charged atomic layers. For example, the dipoles in PbSe arise from the noncentrosymmetric arrangement of Pb- and Se-terminated {111} facets,[21, 22] and in ZnO due to alternating Zn^{2+} and O^{2-} {0001} planes.[15] Cho et al. observed the formation of PbSe nanowires and nanorings and attributed the phenomenon to the oriented attachment at {001} facets.[21] Klokkenburg et al. adopted cryogenic TEM technique to observe *in-situ* dipolar structures formed via oriented attachment of PbSe quantum dots.[23] Wide angle electron diffraction pattern shows the 3D superstructure of 7.7 nm PbSe nanocrystals crystallographically oriented with noticeable misorientation. Talapin et al. studied the superlattice structures formed by nearly spherical PbS, PbSe, and InAs, and α–Fe_2O_3 nanocrystals and argued that the hexagonal-close-packed (hcp) and simple hexagonal (sh) packing of the nanocrystals are due to dipole interaction.[24] The intuition came from the fact that entropy-driven packing of hard spheres had been modeled to be fcc structure [25] and kinetically driven packing of hard spheres had been experimentally shown to be fcc structure or random hexagonal-close-packed (rhcp)[26]. Other dipolar quantum dot systems that have been

reported to aggregate via oriented attachment include PbS,[27] CdTe,[28] CdSe,[23, 29] and Pt_3Fe[30]. For ZnO, extensive publications have suggested the dipolar interaction among the ZnO nanocrystals and various structures have been reported.[31-34]

Organic molecules may also exhibit dipolar structures, for example, proteins such as gelatine and D, L-Alanine. Polar organic crystals of D, L-Alanine form mesocrystals in the form of wires in the absence of any additives.[35, 36, 37] Simon et al.[38, 39] suggested that a parallel orientation of triple-helical protein fibers of gelatine gave rise to parallel ordering of dipoles that orientates the growth of fluorapatite – gelatine composites.[38, 39]

1.2.2.2 Magnetic Dipoles

In nature, magnetotatic bacteria can produce magnetic Fe_3O_4 and Fe_3S_4 superstructures which impose them the ability to swim along the earth's magnetic field.[40] Analogous to electric dipoles, magnetic dipoles can also direct the oriented attachment of magnetic nanocrystals and lead to the formation of crystallographically aligned structures. For example, strong magnetic dipolar interactions can help the Fe_3O_4 ferrimagnetic nanocrystals of 53 nm to self-assemble into oriented 1D, 2D, and 3D superstructures in the absence of magnetic field.[41] It has been reported that magnetic $CoPt_3$ nanocrystals can form hcp superlattice.[24, 42] Yao et al. reported self-assembly of hematite mesocrystals α–Fe_2O_3 using a surfactant-free method.[43]

1.2.2.3 Electric Field

Dipolar nanoparticles or anisotropically charged particles are responsive to

external electric field. Therefore, external electric fields are able to impart extra forces that affect the assembly process and consequently morphology of mesocrystals. Ryan et al. applied an electric field of 1 V/μm to CdS nanorods (5 nm x 30 nm) dispersed initially in toluene to produce 2D and 3D assemblies of perpendicularly aligned nanorods on substrate.[44] Gupta et al. reported that alkane functionalized dipolar CdSe nanorods (8 nm x 40 nm) were able to stand perpendicular to substrate in correspondence to the applied external electric field of 10 V/μm, which is also perpendicular to the substrate.[45] Lausser et al. applied an external electric field of 0.1 V/μm to $BaTiO_3$ nanoparticles (< 50 nm) and made the dipoles in different ferroelectric domains to align with the direction of the electric field.[46] The resultant superstructure was a "combined result of nanoparticle alignment by the electric field and crystallographic fusion of the nanoparticles under defined coincidence angles following an oriented attachment process".

1.2.2.4 Magnetic Field

Externally applied magnetic fields are able to align the magnetic moments in magnetic nanocrystals and direct their oriented assembly or induce & align the magnetic moments. For the materials exhibiting no magnetic dipoles, such as paramagnetic, superparamagnetic, and diamagnetic materials, externally applied magnetic fields are able to induce magnetic moments and the resultant various interactions caused by magnetic dipolar interaction may be able to align and assemble the nanocrystals in a crystallographic register.

A systematic study done by Li et al. demonstrated that the strength of magnetic dipolar interaction fatally determines the ability for these nanocrystals to assemble

into mesocrystals.[41] Such strength of magnetic dipolar interaction was manipulated by altering the size of Fe_3O_4 nanocrystals because magnetism is a volume dependent property that features the collective interaction of atomic magnetic dipoles. By applying a weak external magnetic field (around 0.06 T) the Fe_3O_4 nanocrystals of 21 nm self-assembled into crystallographically oriented superstructures. They successfully prepared 2D mesocrystal as large as 10 x 10 μm with a crystallographic direction in [111] perpendicular to substrate when the magnetic field was applied horizontally with respect to the substrate. By changing the direction of magnetic field to perpendicular to the substrate 3D nanorod mesocrystals with 1.2 μm in length, 250 nm in diameter and long axis in [111] were obtained instead. However, when the magnetic dipole interaction was too weak, mesocrystals could not form. For example, with the same external magnetic field the 8 nm Fe_3O_4 nanocrystals cannot self-assemble into oriented superstructure due to the weak magnetic dipolar interaction. Similar results were also reported by Ahniyaz et al. that the formation of 3D mesocrystals of superparamagnetic Fe_3O_4 nanocrystals can be induced by a temporal modulation of the magnetic dipolar interaction by means of an magnetic field.[47]

Other materials, such as Co nanowires,[48] are also formed via the oriented attachment of preformed nanocrystals due to directional attractive dipolar interaction under external magnetic field. Soumare et al. reported the formation of Ni nanofibers and nanowires of micrometer size, and demonstrated that the morphology of nanowires is dependent on the applied external magnetic field, e.g. a smaller field (0.7 T) gave rise to Ni nanowires consisting of nanocrystals clearly observable under

TEM, while a stronger field (1.4 T) gave rise to much smoother Ni nanowires.[49]

Diamagnets are not permanent magnets but are able to create magnetic field in opposition to an externally applied magnetic field. The repelling force may help the diamagnetic nanocrystals align with the magnetic field and form mesocrystals. Excellent examples include pseudo-single-crystallization of L-alanine and lysozyme by applying external magnetic fields.[50, 51, 52]

1.2.3 Organic Matrix

Composite structures consisting of organic matrix (e.g. chitin) and inorganic materials (e.g. $CaCO_3$) are commonly observed in nature. The organic matrix serves as both nucleation sites for the inorganic precursor ions and texture modifier for the nucleated clusters.[53] Almora-Barrios and Leeuw studied the nucleation of hydroxyapatite ($Ca_{10}(PO_4)_6(OH)_2$) at a collagen template, by immersing triple-helical collagen in a stoichiometric solution of Ca^{2+}, PO_4^{3-}, and OH^- ions.[54] The formation of calcium phosphate clusters at the collagen template was initiated by the prevalent electrostatic attractions between Ca^{2+} and oxygen atoms of the glycine and hydroxyproline residues of collagen. Their simulations of collagen—surface interactions revealed that only the (0110) surface of hydroxyapatite interacts strongly with a collagen peptide suggesting a growth-directing effect of the protein matrix. Similarly, Gehrke et al. could reproduce a nacre structure which was comparable to natural nacre after demineralizing $CaCO_3$ and removing proteins in the natural nacre using 10% acetic acid and mineralization formation on the residual matrix by placing it in a solution of calcium chloride, polyaspartic acid, and ammonium carbonate.[55] Grassmann et al.

prepared a composite structure consisting of polyacrylamide hydrogel and highly aligned calcite crystallites, a structure analogous to some biominerals. The calcite aggregates were mineralized in the matrix resulting in an inorganic assembly intergrown with an organic hydrogel network.[56] This is shown in Figure 1.3 by the route *precursor ions & molecules -> crystallization -> mesocrystal 1*.

1.2.4 Mineral Bridges

The building blocks in a mesocrystal can also be interconnected via mineral bridges such that the whole structure can be kept in integrity. The mineral bridges appear to look straightforward to explain the mutual crystallographic orientation of the building blocks. Oaki et al.[57] have observed similar oriented architectures of bridged nanocrystals with incorporated polymers in both real biominerals (shells, the sponge skeletons of echinoderms, a coral, a foraminifera, and eggshells of hens and emus) and their biomimetic architectures ($CaCO_3$ synthesized in the presence of poly(acrylic acid), re-mineralization of sea urchin spines). They proposed that formation of a mesocrystal with mineral bridges started with the formation of nanocrystals. Polymer adsorption onto the nanoparticles surface quenched its further growth. A site without the adsorption layer continued to grow through the adsorbed polymer layer forming the mineral bridges that allowed growth of another nanocrystal. The process can be repeated until the mesocrystal is built up. Such a growth scenario is rather relevant for the mesocrystal formation within an amorphous precursor phase, which is commonly observed for biominerals and biomimetics. The bridges are also observed in other cases.[6, 58] This is shown in Figure 1.3 by the route *precursor ions & molecules -> nanocrystal 2 -> mesocrystal*

3.

1.2.5 Topotactic and Topochemical Reactions

Solid-state reaction of a single crystal or mesocrystal may result in shrinkage of the unit cell and consequently give rise to a mesocrystal of another mineral system. Zhou et al. reported that thermal treatment or boric acid treatment can convert NH_4TiOF_3 mesocrystals to TiO_2 mesocystals.[59, 60] During the topotactic reaction, nitrogen, hydrogen, and fluoride atoms are removed and the resultant structure shrink in unit cell parameters while the relative positions of titanium atoms remain the same. Wang et al. revealed the topotactic reaction from dicalcium phosphate dihydrate (DCPD) to dicalcium phosphate (DCP) by dehydration and further reaction to hydroxyapatite (HAP) by rapid DCP hydrolysis with NaOH solution.[61] DCPD with 2 % gelatin was precipitated in a gelatin gel. Dehydration of DCPD to DCP at 60 ˚C in air kept the macroscopic crystal morphology but a laminated microstructure that consists of DCP mesocrystals and gelatin. Hydrolysis of the DCP structure to HAP at 95 ˚C and pH 13.6 preserves the laminated microstructure. The gelatin inclusions appear to be important in the topotactic reaction as a similar HAP structure cannot be obtained with commercial DCPD crystals. Wang et al. successfully applied the concept of topotactic reaction to obtain preferential growth and ordered arrangement of TiO_2 nanorods from $TiOF_2$ nanocubes.[61] This is shown in Figure 1.2 by the route *single crystal -> mesocrystal*.

While the research on mesocrystals focuses on various interesting mechanisms, lack of studies on their properties limits the progress of studies on mesocrystals.

1.3 NH_4TiOF_3 mesocrystals

Lei Zhou et al. have successfully prepared NH_4TiOF_3 mesocrystals using a titanium precursor $(NH_4)_2TiF_6$, surfactant Brij 58 ($C_{16}H_{33}(OCH_2CH_2)_{20}OH$) and a F-scavenger boric acid (H_3BO_3) in an aqueous solution.[59, 60, 62] Selected area diffraction patterns (SAEDs) at different areas of one individual NH_4TiOF_3 mesocrystal are single-crystal-like and appear appearantly the same. A tentative mechanism was proposed based on three steps: phase separation, matrix-mediated microphase transformation and self-assembly of the building blocks into mesocrystals. In the first step, titanium precursor ions interact with the PEO groups (-$(OCH_2CH_2)_{20}$-) and condense leading to formation of a viscous phase rich in surfactant. In the second step, the viscous phase undergoes a cooperative reorganization of inorganic and organic components and the surfactant matrix induced oriented crystallization leading to primary "square" building blocks. In the last step, the square building blocks self-assemble in a crystallographic register and form the final mesocrystals. It is proposed that hydrophobic interaction of surfactant Brij 58 molecules leads to the mesoscale assembly of NH_4TiOF_3 mesocrystals and preferential adsorption on (100) and (010) surfaces results in plate-like morphology. When the building blocks fuse, the adsorbed surfactant molecules leave the inorganic material and are restored to the aqueous solution, except that some surfactant molecules are occluded in the resultant mesocrystals. Elemental analysis revealed that the products contain impurities: carbon and boron.

Furthermore, Lee and Shih also prepared NH_4TiOF_3 "discoid crystals" on glass substrates at 40˚C and 2 h with mixture of aqueous solutions of H_3BO_3 and

$(NH_4)_2TiF_6$ in the absence of additives.[63] The NH_4TiOF_3 "discoid crystals" show single crystal diffraction patterns under TEM. Yu et al. prepared NH_4TiOF_3 mesocrystals from H_3BO_3 and $(NH_4)_2TiF_6$ in mixture of 2- propanol and water at 80 ˚C for 20 h by hydrothermal method.[64] Feng et al. developed NH_4TiOF_3 mesocrystals from $TiCl_4$ and NH_4F in mixture of water and ethanol or propanol at 180 ˚C and 12 h by hydrothermal method.[65] Therefore, it is apparent that NH_4TiOF_3 tends to grow via the route of mesocrystals without necessary relation to the additives introduced or precursors used.

It has been demonstrated by Zhou et al.[59, 60, 66] that NH_4TiOF_3 mesocrystals (as a raw materials: $(NH_4)_2TiF_6$ and (H_3BO_3)) could be converted to TiO_2 (anatase) mesocrystals via a topotactic reaction by thermal treatment at 450 ˚C or washing with H_3BO_3 solution (0.5 M).[59, 60, 66] The resultant TiO_2 mesocrystals are rather porous and may therefore find applications in dye-sensitized solar cells and photocatalysts. Similarly, Feng et al. could convert their NH_4TiOF_3 mesocrystals (raw materials: $TiCl_4$ and NH_4F in mixture of water and ethanol or propanol) to {001} faceted TiO_2 (anatase) mesocrystals via the topotactic reaction.[65]

1.4 Project Motivation

Mesocrystals are interesting to study because this is a new area. Various mechanisms have been proposed. However, reports on properties and applications are quite limited.

NH_4TiOF_3 is not a well stuided compound. However, it is useful as it can be converted to TiO_2 (anatase), which is a versatile material that finds applications in photocatalysts, photovoltaics, pigments, and UV absorbers. The nanocrystals and

their crystallographic orientations in TiO_2 mesocrystals that are derived from NH_4TiOF_3 mesocrystals may well be different from those of titanium oxides derived from conventional powder processing routes. Therefore, it is worthwhile to further investigate NH_4TiOF_3 mesocrystals, in terms of their formation and conversion to nanocrystalline TiO_2.

Zhou et al. proposed that the hydrophobic interaction of surfactant Brij 58 molecules led to the mesoscale assembly of NH_4TiOF_3 nanocrystals.[59] This proposal is subject to verification by varying the hydrophobicity of surfactant molecules by replacing Brij 58 with surfactant or organic molecules of lower hydrophobicity.

Zhou et al. also proposed that the preferential adsorption of surfactant Brij 58 molecules on (100) and (010) surfaces of NH_4TiOF_3 nanocrystals resulted in plate-like morphology.[59] To verify the proposal that the density of adsorbed Brij 58 molecules varies from one crystallographic surface to another crystallographic surface, the adsorption sites for various surfaces, based on the unit cell structure of NH_4TiOF_3, must be studied. However, little is known about the atomic coordinates for each element in the structure. Therefore, the unit cell structure of NH_4TiOF_3 has to be determined.

Feng et al. developed NH_4TiOF_3 mesocrystals from different precursors in the absence of hydrophobic forces.[65] Based on literature survey, we understand that there are other interparticle forces that can also contribute to the attraction force and alignment of nanocrystals. Therefore, the intrinsic properties, e.g., ferroelectricity, of NH_4TiOF_3 in connection to its unit cell structure that might contribute to the mesoscale assembly of NH_4TiOF_3 nanocrystals will have to be studied.

Zhou et al. also reported that H_3BO_3 (0.5 M) could help convert NH_4TiOF_3 to TiO_2 (anatase).[59] It is therefore important to properly understand why NH_4TiOF_3 should convert to TiO_2 (anatase), in the controlled conditions. The reason will be studied along with the effect of aging NH_4TiOF_3 mesocrystals in the mother liquor which contain the original boric acid (H_3BO_3) and the effect of this conversion process on the formation of NH_4TiOF_3 mesocrystals.

The formation and stability of NH_4TiOF_3 mesocrystals in varying conditions and environments are far from being established, which are the main scopes of the present study. The factors affecting their formation will be studied in detail. The findings in this project will undoubtedly help advance understandings on the formation and growth process of mesocrystals – a new class of crystals. Specifically as detailed in this thesis, various interparticle forces can be tuned to control the formation and growth of mesocrystals, and the stability of the assembling nanocrystals can also strongly affect the formation and growth of mesocrystals.

CHAPTER 2. EXPERIMENTAL PROCEDURES

2.1 Sample Preparation

2.1.1 Preparation of Powder Samples

The mesocrystals were grown in an aqueous solution. Typically, an aqueous solution containing surfactant Brij 58, F127, or other organic additives (e.g. ethanol, ethylene glycol, polyethylene glycol, di-ethylene glycol) was first prepared at 23˚C. Afterwards, an appropriate amount of fluoride scavenger H_3BO_3 (99.8%, Merck) was dissolved in the previously prepared solution. $(NH_4)_2TiF_6$ (99.99%, Aldrich) was then added, and stirring was stopped immediately upon the complete dissolution. The weight ratio of water : H_3BO_3 : $(NH_4)_2TiF_6$ was 50 : 0.618 : 0.990. Mesocrystals were allowed to grow at the static condition at 4˚C, 23˚C or 35˚C for various periods of time. They were then recovered by centrifugation and washing successively for three times. Solvents used for washing were water, acetone and ethanol. Drying was carried out at 60 ˚C for 12 h. *Ex-situ* dissolution of the resultant mesocrystals was performed by dispersing them in water or solutions by hand-shaking. The amount and dispersion time are given in the main text. The calcination condition to form Tio_2 will be detailed in the respective chapter.

2.1.2 Preparation of Particles on Substrates

An aqueous solution containing surfactant Brij 58 was prepared first (Brij 58: 3g; water: 10g). 123.7 mg of fluoride scavenger H_3BO_3 (99.8%, Merck) was then

dissolved. Lastly, 198.0 mg of $(NH_4)_2TiF_6$ (99.99%, Aldrich) was added. When $(NH_4)_2TiF_6$ was well dissolved, a piece of fluorine-doped tin oxide (SnO_2:F) (FTO) coated glass (TEC15, Dyesol) was placed into the solution. NH_4TiOF_3 mesocrystals were allowed to grow under static condition in a PPE tube. After 3 h, the glass was removed from solution and dipped in water to remove excess inorganic impurities and subsequently ultrasonicated for 5 s in ethanol to remove Brij 58 molecules and the particles which were loosely attached to the substrate. Drying was done by purging with N_2. The solid particles in the solution were then recovered by centrifugation and washing successively for three times. The solvents used for washing were water, acetone and ethanol. Drying of the powder was carried out at 60 ˚C for 12 h.

2.2 Sample Characterization

2.2.1 X-Ray Diffraction (XRD)

X-ray Diffraction (XRD) was used to identify the crystalline phases and characterize crystallite size for the particles. It follows the Bragg's law, i.e., when the Bragg condition

$$n\lambda = 2d\sin\theta$$

is satisfied, diffraction occurs, where λ is the wavelength of X-ray, d is interplanar spacing of a crystalline plane, θ is Bragg's angle, and n is an integer representing the order of the diffraction peak. The crystalline size of the phase can be estimated using the Scherrer equation

$$t = \frac{0.9\lambda}{B\cos\theta}$$

where t is the average crystallite size, and B is the line broadening on the basis of full-width at half maximum (fwhm) of the diffraction peak.

In this project, XRD (Bruker AXS D8 Advance, Germany) was used to study the crystalline phase and estimate the crystallite size of the particles. XRD measurements were carried out by using Cu Kα radiation (1.5406 Å) operated at 40 kV and 40 mA with a step size of 0.02^o and a time per step of 0.5 second. It followed a $\theta/2\theta$ Bragg-Brentano geometry, and the 2θ angle was varied from 10^o to 60^o. Grazing Incidence Angle XRD (GIAXRD) method was adopted to minimize the contribution from substrate for the samples grown on FTO glass, where the incidence angle between the beam and substrate surface was fixed at 1.5^o.

2.2.2 X-Ray Photoelectron Spectroscopy (XPS)

XPS spectra were obtained by irradiating the material using X-rays while simultaneously measuring the kinetic energy and the corresponding number of electrons that escape from the top 1-10 nm of the sample. A typical XPS spectrum is a plot of counts of electrons (y-axis) versus the binding energy (x-axis). The binding energy is calculated based on the equation

$$E_{binding} = E_{photon} - E_{kinetic} - \Phi$$

where E_{photon} is the energy of the irradiating X-rays, $E_{kinetic}$ is the measured kinetic energy of the emitted electron and Φ is the spectroscopic work function.

XPS can virtually detect all elements except Hydrogen (H) and Helium (He). Each

element produces a characteristic set of XPS peaks at the respective characteristic binding energies. Thus XPS spectra can be used to identify the elements that exist in the sample. XPS can measure up to 0.1 at% and XPS is done in ultrahigh vacuum to avoid signal loss due to scattering by residual gas.

Besides photoelectron lines, Auger electron lines are also present in XPS spectra. The excited atom may relax by two paths: X-ray process and Auger process. In the X-ray process, an outer shell electron jumps down to an empty core level and the excessive energy is released in the form of an X-ray. In the Auger process, an outer shell electron jumps down to an empty core level and the excessive energy imparts ejection of another outer shell electron from the atom. The shift of binding energy, corresponding to the chemical states, is analyzed. Moreover, the intensity of each peak corresponds to the amount of the atom or chemical status. Therefore, XPS spectra can be used to determine the relative amount of each element present in the sample and its various chemical states.

In this project, the powdered samples were studied by using XPS (Kratos Axis Ultra DLD) employing a monochromatic Al Kα1 source (1486.6 eV).

2.2.3 Transmission Electron Microscopy (TEM)

The transmission electron microscope (TEM) operates like the light microscope but uses electrons instead of light. Electrons make it possible to get much better resolution because of their much shorter wavelength. Electrons emitted by an electron source travel through vacuum in the column of the microscope and through the sample. Instead of glass lenses focusing the light in the light microscope, the

TEM uses electromagnetic lenses to focus the electrons into a very thin beam. Depending on the density of the material present, some of the electrons are scattered from the beam. The unscattered electrons hit a fluorescent screen and thereby give rise to a bright background and a "shadow image" of the specimen with the different parts displayed in varied darkness according to their densities. The image is obtained in the so-called “bright field imaging” mode.

TEM can also operate in three further modes: selected area electron diffraction (SAED), dark field imaging, high resolution TEM (HRTEM) imaging.

SAED mode operates on a selected area of the sample. A fraction of the scattered electrons is scattered to particular angles, i.e., the electron diffraction occurs. In electron diffraction, the planar spacing can be calculated using the following equation

$$r\,d = L\,\lambda$$

where r is the measured distance of a diffraction spot from the center of the transmitted rays, d is the planar spacing, L is the camera length and λ is the wavelength of electrons.

Dark field imaging mode involves tilting the incident illumination until a diffracted, rather than the incident beam passes through the sample, leaving a black background. In single crystal specimens, dark field images of a specimen allow one to "light up" only those lattice defects. In polycrystalline specimens, on the other hand, dark field images serve to light up only that subset of crystals that diffracts the diffracted beam.

HRTEM imaging allows one to image the sample at an atomic scale, providing a valuable tool to study the nanoscale properties of crystalline materials.

Both TEM (JEOL JEM 2010F, 200 kV) and HRTEM (JEOL JEM 3010, 300 kV) were employed to investigate the morphology and crystalline phases of particles and mesocrystals. SAED patterns of particles were obtained using TEM at an accelerating voltage of 200 kV. Dark field imaging was conducted by using the diffracted beam corresponding to (110) as the electron source.

2.2.4 Scanning Electron Microscopy (SEM)

Scanning electron microscopy (SEM) was used to image the sample surfaces and thereby morphology of the particles. It detects secondary or backscattered electrons which are emitted from the surface due to excitation by the primary electron beam. The electron beam is rastered across the sample, with detectors mapping the detected signals with beam position. Energy dispersive X-ray spectroscopy (EDX or EDS) attached to TEM can be used for elemental characterization. It analyzes the elementally characteristic X-rays emitted from relaxation of excited electrons in the sample. The powdered samples were dispersed in ethanol and dropped on glass substrates. Sputter-coating with gold was carried out after drying. They were viewed with a field emission SEM (Philips XL30 FEG) operating at an accelerating voltage of 5 kV. Energy-dispersive X-ray Spectroscopy (EDS, Carl Zeiss AG – SUPRA 40, INCAx-sight) mapping was conducted to monitor elemental distribution.

2.2.5 Ultraviolet-Visible-Near Infrared (UV-VIS-NIR) Spectroscopy

(UV-VIS-NIR) Spectroscopy was used to determine the concentration of Orange II. Ultraviolet or visible light can excite some electrons in materials to higher energy levels. UV-VIS-NIR Spectroscopy measures the intensity of light passing through a

sample (I), and compares it to the intensity of light before it passes through the sample (I_0). The ratio I / I_0 is called the transmittance, and is usually expressed as a percentage (%T). The absorbance, A, is based on the transmittance:

$$A = - log (\%T / 100\%)$$

UV-VIS-NIR absorbance measurements (UV-1601, Shimadzu) were taken in the wavelength range between 300 nm and 600 nm at an interval wavelength of 1 nm. Quartz tubes were used for measurements as quartz maintains a high optical transparency for the intended measurement range.

2.2.6 Fourier Transform Infrared (FTIR) Spectroscopy

FTIR spectroscopy deals with the infrared region of the electromagnetic spectrum. Some of the incident light is absorbed by the sample and some of it is transmitted. No two unique molecular structures show the same infrared spectrum. The resulting spectrum shows the molecular absorption and transmission, creating a molecular fingerprint of the sample. In addition, the intensity of the peaks in the spectrum indicates the amount of material present. The measured signal is decoded by the mathematical method known as Fourier transformation.

In this project, FTIR spectrophotometer (Varian 3100 Excalibur Series) was employed to help identify the chemical compositions in the particles. The spectra were obtained at room temperature in the mid infrared range from 400 to 4000 cm^{-1}, by averaging 64 scans with a nominal resolution of 4 cm^{-1}. The specimens were prepared by grinding the sample particles with KBr powder and pressing the mixture into small pellets.

2.2.7 Thermal Analysis

Thermogravimetric analysis (TGA) is a thermoanalytical technique for studying the weight change with temperature so that the composition of the material can be estimated. In the present project, TGA was performed on a thermogravimetric analyzer (TGA 2950, Du Pont) with a platinum holder in air.

2.2.8 Photocatalytic Activity Measurement

Photocatalysis experiment was carried out under Ultraviolet (UV) irradiation (4 W, λ_{max} = 253.7 nm) for 1 h at room temperature (23˚C). An aqueous solution (3.3E-5 M, 10 g) of Orange II (analytical, Fluka) was decomposed with 5.0 mg of TiO_2. Adsorption equilibrium of Orange II was allowed under magnetic stirring in dark for 1 h prior to UV illumination. The concentration of residual Orange II was determined by measuring UV-VIS-NIR absorbance of the solution after filtering off the TiO_2 particles (Millex Millipore filter mesh size: 200 nm). The portion of residual Orange II after photodegradation (C/C_0) was determined by normalizing the UV-vis absorbance at the wavelength 484 nm to that for the as-prepared Orange II aqueous solution.

2.2.9 Piezoelectric Force Microscopy (PFM)

PFM is a relatively new scanning probe microscopy that employs the piezoelectric effect for contrast. A conductive AFM tip is in contact with sample surface and a voltage is applied across the tip and sample surface. Under the external voltage, ferroelectric or piezoelectric materials would locally expand or contract and result in deflection change of the tip. If the external voltage is in AC mode, sample surface

oscillation can be recorded. Overall, domains with downward or upward polarization can be detected and revealed by regions in different contrast. For polarization components within the surface plane, vector PFM with one vertical and two lateral channels can provide more information. There are four PFM imaging modes: vertical PFM, Lateral PFM, Vector PFM, and piezoelectric lithography. In vertical PFM imaging, the out-of-plane polarization is measured. In lateral PFM, the in-plane component of polarization is detected as lateral motion of the cantilever due to voltage-induced surface shearing. In vector PFM, three components of piezoresponse (vertical PFM and two orthogonal lateral PFM) contribute to the real space reconstruction of polarization orientation. Since the polarization in a ferroelectric material can be altered by external voltage, single domains, domain arrays, and complex patterns can be written without changing the surface. In addition, PFM spectroscopy can locally generate hysteresis loops in ferroelectric materials.

In this project, PFM has been conducted by the collaborators, Prof Zeng Kaiyang and Dr Amit Kumar. Both vertical and lateral Piezoresponse Force Microscopy (PFM, MFP-3D, Asylum Research, USA) were used to investigate the piezoelectric and ferroelectric responses, domain structure and local hysteresis loops for the mesocrystals. A Pt-coated silicon cantilever tip (OLYMPUS OMCL-AC240TM) (Electric-lever, Olympus, Japan) was used.

2.2.10 Brunauer-Emmett-Teller (BET) Analysis

BET surface area is evaluated using a fully automated analyzer by nitrogen multilayer adsorption measured as a function of relative pressure.

Barrett-Joyner-Halenda (BJH) pore size and volume analyses are conducted by the adsorption and desorption technique. Adsorption of nitrogen at the temperature of 77 K gives rise to the adsorption isotherm or BET isotherm, which is mostly observed for porous materials. Monolayer formation of gas molecules on the surface is used to determine the specific surface area, while the principle of capillary condensation can be applied to assess the presence of pores, pore volume and pore size distribution. Prior to the gas adsorption measurement, the sample is degassed at elevated temperature in vacuum to remove volatile impurities under that temperature.

In this project, the instrument employed was a surface area and porosity analyzer (Micromerities ASAP 2020). The samples were degassed at 120 ˚C.

2.2.11 Zeta Potential

Zeta potential is related to the physical behavior of particles suspended in a dispersant. There are two liquid layers surrounding each particle. An inner layer (Stern layer) consists of strongly bound ions, and an outer (diffuse) layer consists of less firmly bound ions. In the outer layer, association between particle and ions gets weaker with distance. A boundary separates the outer layer into two parts: one part moves with the particle as it moves, and another part stays with the bulk dispersant as the particle moves. The potential at this boundary is the Zeta potential.

In this project, zeta potential of the particles was determined *in-situ* by a Malvern Zetasizer (Nanoseries Nano-ZS) which uses a combination of laser Doppler velocimetry and phase analysis light scattering to measure the particle electrophoretic mobility. Electrophoretic mobility refers to the velocity of a charged

particle in a unit electric field. Zeta potential is related to the electrophoretic mobility by the Henry equation of

$$U = \frac{2z\xi \, \mathrm{f}(k\alpha)}{3\eta}$$

where U = electrophoretic mobility, z = Zeta potential, ξ = dielectric constant, η = viscosity, and $\mathrm{f}(k\alpha)$ = Henry's function.

2.2.12 Elemental Analysis

Carbon, Hydrogen, Nitrogen, and Sulfur (CHNS) method can be employed for rapid determination of the carbon, hydrogen, nitrogen, and sulfur contents in organic and other types of materials by measuring the amount of elements released after burning the sample. In this project, the amount of carbon, nitrogen, and hydrogen was determined by this method.

Modular Ion Chromatography (IC) system is used for the independent determination of anions with chemical suppression. In this project, the amount of fluorine was determined by this method.

Inductively Coupled Plasma (ICP) method is widely used in determining metals in solutions for identification and differentiation of elemental metals down to ppb levels. Analysis procedure includes sample preparation by open / closed digestion. In this project, this method was employed to determine the amount of titanium where the instrumentation included Perkin Elmer Dual-view Optima 5300 DV ICP-OES system.

CHAPTER 3. GROWTH AND ANISOTROPIC DISSOLUTION BEHAVIOR OF NH_4TIOF_3 MESOCRYSTALS

3.1 Background

There have been several fundamental studies with ammonium oxofluorotitanates, which are a group of interesting compounds by themselves and also precursors for synthesizing doped TiO_2 for various functional applications.[67-71] Laptash et al. successfully synthesized $(NH_4)_3TiOF_5$, $(NH_4)_2TiOF_4$, and NH_4TiOF_3 by hydrolysis of $(NH_4)_2TiF_6$ (ammonium hexafluorotitanate).[70] A scheme of hydrolysis for group IV hexafluorocomplexes was proposed by Schmitt et al.: $[MF_6]^{2-} + nH_2O \rightarrow [MF_{6-n}(OH)_n]^{2-} + nHF$.[72] Aqueous solutions containing both $(NH_4)_2TiF_6$ and H_3BO_3 have been investigated for synthesizing anatase TiO_2 films, where H_3BO_3 serves as the fluoride scavenger to assist hydrolysis of $[TiF_6]^{2-}$.[73-76] Deki et al. have studied the effect of $[H_3BO_3]/[(NH_4)_2TiF_6]$ concentration ratio on the chemical composition of the deposited thin films on glass substrates.[75] A high $[H_3BO_3]/[(NH_4)_2TiF_6]$ concentration ratio produces anatase TiO_2 film, while a low ratio gives rise to NH_4TiOF_3 film. However, a very low concentration of H_3BO_3 (<0.075 M) results in no deposition regardless of the concentration of $(NH_4)_2TiF_6$. It may be inferred that NH_4TiOF_3 is a metastable phase involved in the conversion of $(NH_4)_2TiF_6$ to anatase TiO_2 in the presence of an appropriate amount of H_3BO_3.

The first report on NH_4TiOF_3 mesocrystals of regular morphology was made by Zhou et al..[59, 62] Well facetted polyhedral platelets with smoothly truncated corners were prepared from an aqueous solution of $(NH_4)_2TiF_6$, H_3BO_3 and nonionic surfactant (Brij 56, Brij 58, or Brij 700). On the basis of the single-crystal-like SAED (selected area electron diffraction) patterns from different areas of a single NH_4TiOF_3 particle, a formation mechanism for oriented assembly of building blocks to mesocrystal was proposed. Feng et al. have reported square platelets of NH_4TiOF_3 mesocrystals prepared from $TiCl_4$ and NH_4F in a mixed solvent of water and ethanol or 2-propanol.[65] The NH_4TiOF_3 mesocrystals were formed in an autoclave operated at 180˚C for 0 h, 6 h or 12 h, respectively. Interestingly, a single anatase phase of TiO_2 was obtained by this method when extending the reaction time in the autoclave to 24 h. As discussed later on, besides these solid platelets, polyhedral platelets of NH_4TiOF_3 mesocrystals with regularly shaped anisotropic holes in the center can also develop, in association with the preferred dissolution in certain crystallographic directions.

The concept “mesocrystal” for mesoscale assembly of the crystallographically oriented building blocks was first described by Colfen et al. in 2005. Mesocrystals are a new class of crystalline materials, besides the widely known single crystals and polycrystals.[3] Mesocrystals can scatter electrons and light like a single crystal. However, they consist of mesoscopically scaled (1-1000 nm) crystalline subunits that are interspaced by organic additives, pores, interlayers, or grain boundaries.[4] Very few studies have been made with the effects of these defects on the material properties. For example, Berman et al. have reported that Calcite ($CaCO_3$)

mesocrystals grown in the presence of sea-urchin protein exhibit reduced brittleness as compared to the pure single crystals.[77] The Calcite ($CaCO_3$) mesocrystals studied occluded carbon of 0.02 wt%.

The formation of inner holes in a crystal has been widely studied.[78-82] It is commonly believed to arise from the ostwald ripening whereby the inner core is sacrificed to grow outer shell.[78, 79] Penn et al. demonstrated that dislocations arose from imperfect oriented attachment in the formation of mesocrystals.[83] It has been suggested that dissolution of mesocrystals and single crystals initiates at these defected sites.[80-82] Tao et al. studied dissolution of $Ca_3(PO_4)_2$ mesocrystals in water, where the defects were randomly located except for the defect-free well-re-constructured thin shell and therefore dissolution pits appeared randomly.[80] Soare et al. observed a randomly aggregated core in CuC_2O_4 mesocrystals caused by the rapid aggregation of nanoparticles in the initial growth stage, where the dissolution behavior of these CuC_2O_4 mesocrystals initiated at center.[81] Li et al. reported that the high density of defects at crystal center caused dissolution holes to appear in ZnO mesocrystals.[82] However, the contributions from occluded species might play an important role in the dissolution of mesocrystals.

In this chapter, we have investigated the formation of well facetted polyhedral NH4TiOF3 mesocrystals and their subsequent anisotropic dissolution in aqueous solution, where these two competing processes are shown to occur concurrently. In particular, we show that the occlusion of surfactant molecules accounts for the formation of initial dissolution sites, as demonstrated by both in-situ and ex-situ studies, giving rise to mesocrystals of hollow center.

3.2 Experimental Details

The mesocrystals were grown in an aqueous solution, according to what has been reported.[12] Typically, an aqueous solution of surfactant Brij 58 (15 g in 50 g of deionized water) was first prepared at 35 ˚C. Afterwards, an appropriate amount of fluoride scavenger H_3BO_3 (618.3 mg) was dissolved in the surfactant solution. $(NH_4)_2TiF_6$ (989.9 mg) was then added, and stirring was stopped immediately upon its complete dissolution. Mesocrystals were allowed to grow at static condition at 35 ˚C for various time periods. They were then recovered by centrifugation and washing successively for three times. Solvents used for washing were water, acetone and ethanol. *Ex-situ* dissolution of the resultant mesocrystals was performed by dispersing them in water by hand-shaking. The amount and dispersion time are given in the respective results discussed below.

3.3 Preferential Dissolution and Solution pH Evolution

Figure 3.1 shows the morphology development of the NH_4TiOF_3 mesocrystals with growth time in the aqueous solution. An irregular morphology is observed at 30 min, followed by a square shape that appears at 1 h. The regularly shaped particles then dominate at 2 h and continue to grow in size till 20 h. A relatively smooth surface texture is observed for 3 h and 9 h. Debris starts to appear at the center of mesocrystal faces at 20 h. Observable holes are developed at the face center after 96 h. At 142 h, the holes propagate preferentially in the directions of truncated corners. They are separated by the accumulated debris in the center, and they continue to grow anisotropically and have developed through thickness by 164 h. The growth front of

holes is thinner than the edges of the mesocrystal, resulting in wedge-like thickness of the residue.

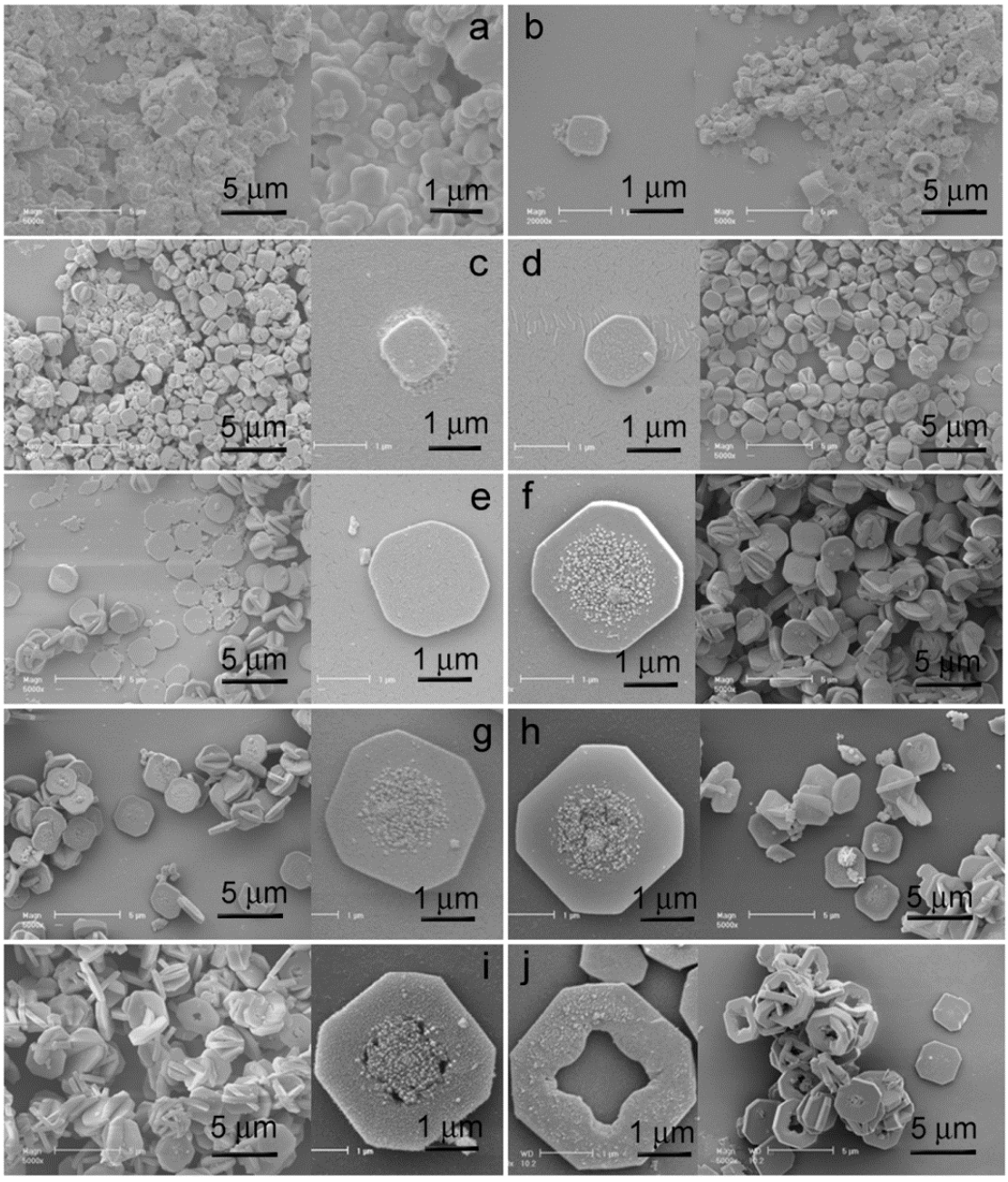

Figure 3.1 SEM images of the as synthesized NH4TiOF3 mesocrystals collected at (a) 30 min, (b) 1 h, (c) 2 h, (d) 3 h, (e) 9 h, (f) 20 h, (g) 40 h, (h) 96 h, (i) 142 h, and (j) 164 h, respectively.

Figure 3.2 shows the *in-situ* variation in pH value of the aqueous solution with reaction time. A general decrease in pH value occurs before 10 h, while a continuous increase is observed afterwards, untill 140 h. According to Schmitt et al.,[72] $(NH_4)_2TiF_6$ undergoes the following hydrolysis:

$$[TiF_6]^{2-} + nH_2O = [TiF_{6-n}(OH)_n]^{2-} + nHF \quad \text{(where "n" is small)} \qquad (3\text{-}1)$$

while HF is a weak acid, it gives the more stable anion in water solution HF_2^-,

$$2HF + H_2O = HF_2^- + H_3O^+ \qquad (3\text{-}2)$$

H_3BO_3 is well known as a scavenger for F^-, where its triangular Lewis structure undergoes to tetrahedral stable structure scavenging F^- from $[TiF_6]^{2-}$,

$$TiF_6^{2-} + B(OH)_3 = B(OH)_3F^- + TiF_5^- \qquad (3\text{-}3)$$

where TiF_5^- hydrolyzes rapidly, following

$$TiF_5^- + 2H_2O = Ti(OH)F_5^{2-} + H_3O^+ \qquad (3\text{-}4)$$

This ensures the acid reaction of the solution, agreeing with the initial decrease in solution pH observed in the present work.

Oligomerization is the main feature of the hydrolyses processes of both titanium and boron compounds.[71, 84] The hydrolysis products oligomerize (or polymerize) to give the layered structure of $TiOF_3^-$ with the O atoms as terminal and the F atoms as bridging[3]:

$$TiF_5^- + H_2O = TiOF_3^- + 2HF \qquad (3\text{-}5)$$

Charge is balanced by NH_4^+ and NH_4TiOF_3 precipitates according to the following process:

$$NH_4^+ + TiOF_3^- = NH_4TiOF_3\downarrow \qquad (3\text{-}6)$$

Further reactions can be expressed as:

$TiF_5^- + B(OH)_3F^- = TiOF_3^- + B(OH)F_3^- + H_2O$, and (3-7)

$TiF_5^- + 3B(OH)_3F^- = TiO_2\downarrow + BF_4^- + B_2O(OH)_2F_4^{2-} + 3H_2O + OH^-$ (3-8)

This gives rise to the increase in solution pH, as shown in Figure 3.2.

A similar process has been described by Zhou et al.[12]:

$4NH_4TiOF_3 + 3H_3BO_3 = 4NH_4^+ + 3BF_4^- + OH^- + 4H_2O + 4TiO_2\downarrow$ (3-9)

The hexafluorotitanate group TiF_6^{2-} can be, in principle, hydrolyzed leading to the formation of TiO_2. However, the process is kinetically slow. It can be driven by the presence of H_3BO_3, which is a well known F-scavenger. NH_4TiOF_3 is an intermediate product that can precipitate in the aqueous solution. At the initial stage (*i.e.* before 10 h), reactions lead to a decrease in pH value of the reaction solution due to the net increase in the $[H_3O^+]$ concentration. However, the further reactions increases pH value of the aqueous solution, as described above.

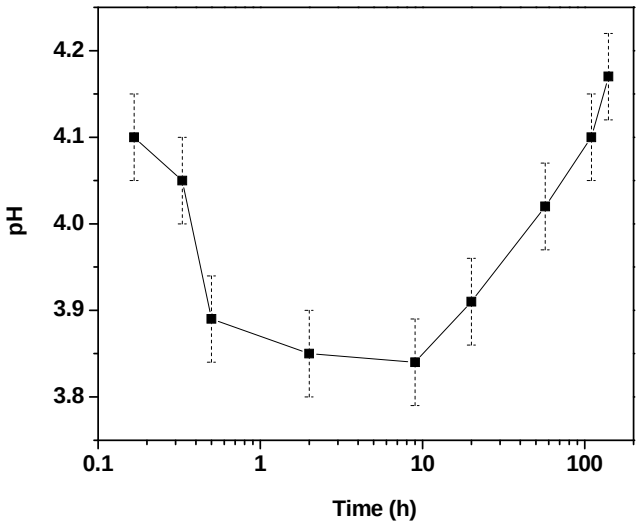

Figure 3.2 Plot of *in-situ* pH value of the reaction solution versus reaction time.

Figure 3.3 shows the evolution of mesocrystal size as a function of growth time. The initial rapid growth in crystal size occurs up to 10 h. However, the growth rate decreases dramatically during this period, as shown by the inset in Figure 3.3. The growth rate continues slowing down after 10 h and approaches zero by 164 h. This observation is consistent with the *in-situ* pH value analysis. The fast growth of mesocrystals at the initial stage (*i.e.* before 10 h) is boosted by the rapid hydrolysis of the raw material $(NH_4)_2TiF_6$ and subsequent formation of NH_4TiOF_3 (*i.e.* a high supersaturation). Conversely, after 10 h, the slow growth rate is attributable to reduction of the starting material $(NH_4)_2TiF_6$ (*i.e.* a low supersaturation).

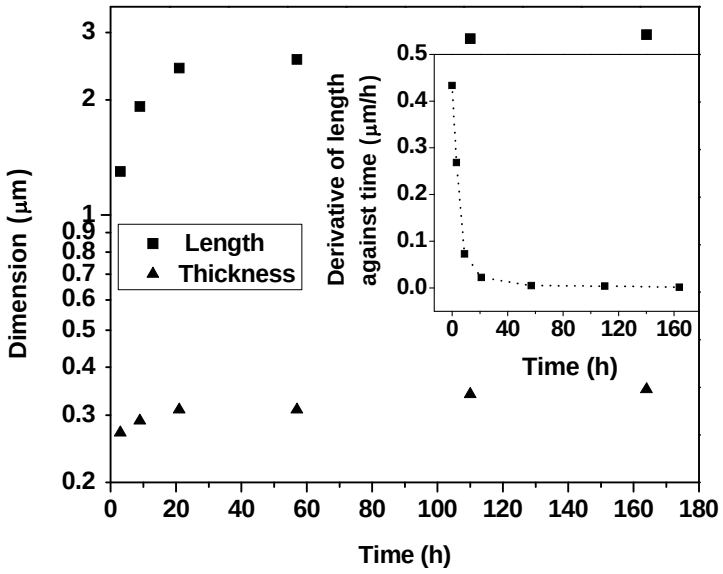

Figure 3.3 Length and thickness of NH_4TiOF_3 mesocrystals as a function of reaction time. The inset is the derivative of length against time.

3.4 Mesocrystal Characterization and Crystalline Phase Evolution

X-ray Diffraction (XRD) phase analysis shows that the crystalline phase in the samples collected at various reaction periods is NH_4TiOF_3, except that TiO_2 is also observed after aging the solution for 2 months (see Figure 3.4). Figure 3.5 shows a representative mesocrystal in the sample collected at 164 h. Its mesocrystalline nature is demonstrated by the nano-pores that are observed with Brunauer-Emmett-Teller (BET) method and HRTEM (see Figures 3.6 and 3.7), supporting that the NH_4TiOF_3 mesocrystals are assembled from individual nano-particles. The Selected Area Electron Diffraction (SAED) patterns (Figures 3.5c and 3.5e) at different areas of the same mesocrystal show the same crystallographic orientation and the single-crystal-like feature, confirming its mesocrystal nature. Unit cell parameters from ref. [59] are used to index the diffraction spots. Indexation results suggest the [001] zone of NH_4TiOF_3. The crystallographic directions [100] and [010] thus determined are shown in Figure 3.5d. This result is further confirmed by the High Resolution TEM (HR-TEM) in Figure 3.5b which shows the lattice fringes with a spacing of 0.38 nm corresponding to the interplanar distance of (020) plane. Moreover, the anisotropic hole at the center of mesocrystals shown in Figure 3.1j is also observed in Figure 3.5d. The variation in contrast (Figure 3.5a) suggests that thickness at the growth front of central hole is smaller than the edges of the mesocrystal. This is consistent with the SEM observation in Figure 3.1j. This further demonstrates that the hole grows from the center of mesocrystal surface ((001) plane), deepens through thickness in [001] direction and propagates anisotropically in (001) plane (*i.e.* fastest in <100> and <010> directions).

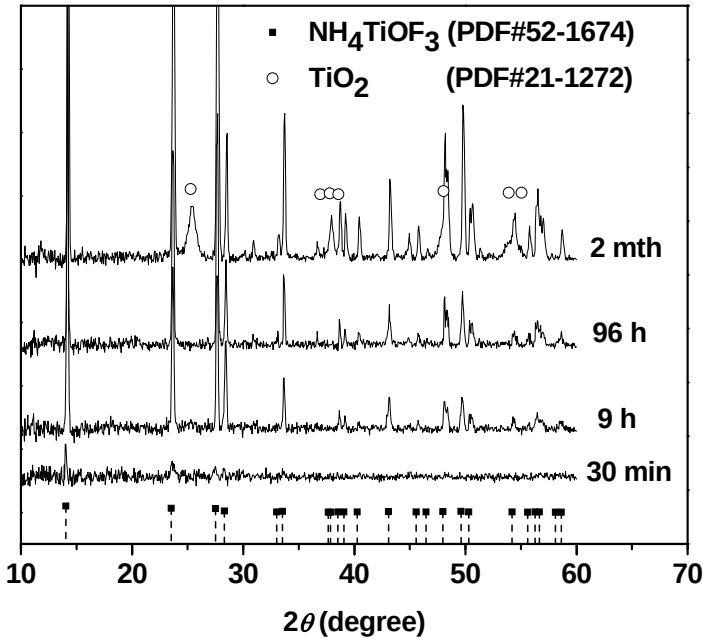

Figure 3.4 XRD of the mesocrystal powder collected at different reaction times.

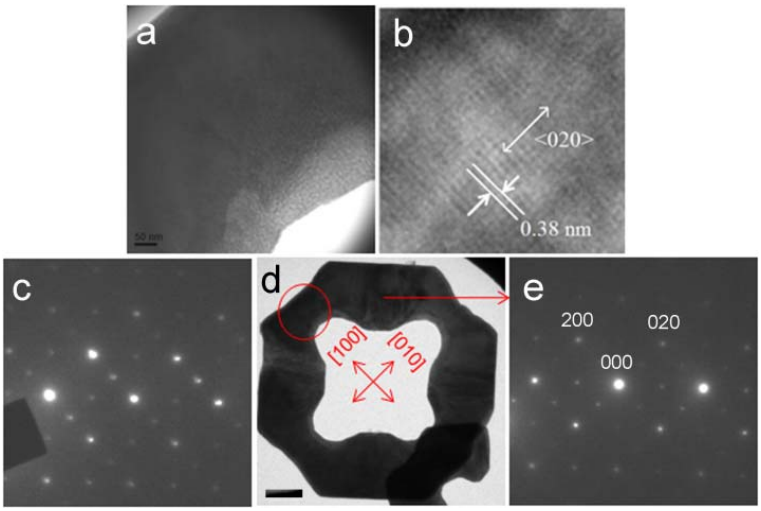

Figure 3.5 TEM of the as-synthesized NH_4TiOF_3 mesocrystals collected at 164 h of reaction time.The area circled in (d) corresponds to (a)-(c); where the scale bar is 0.5 μm; Extra spots in (c) and (e) are attributable to the double diffraction arising from thickness.

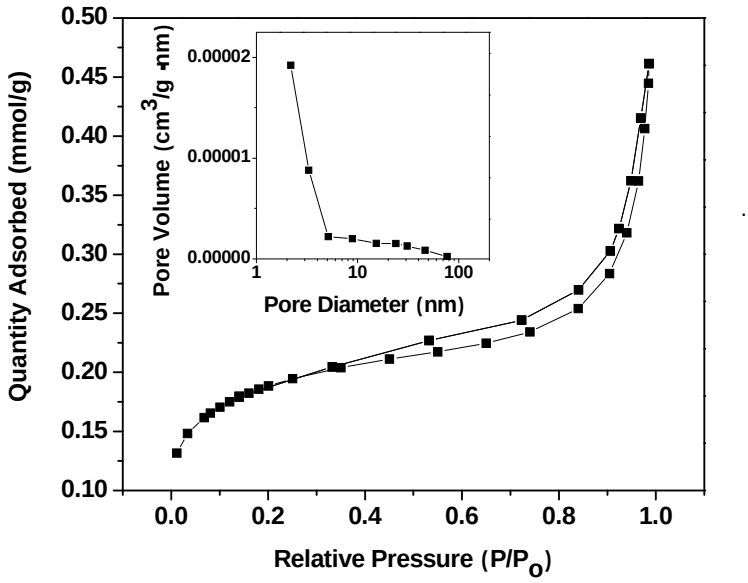

Figure 3.6 N_2 adsorption and desorption isotherm and the pore size distribution in NH_4TiOF_3 mesocrystals collected at 164 h (The pore size distribution is derived from the desorption branch by the Barrett-Joyner-Halenda (BJH) model).

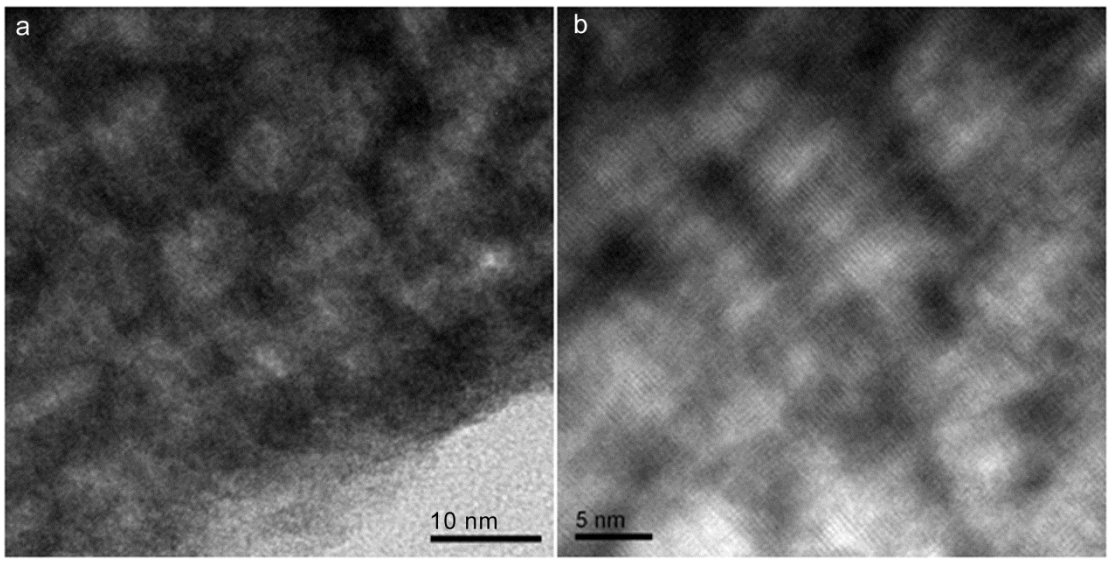

Figure 3.7 (a) and (b) HRTEM of an NH_4TiOF_3 mesocrystal collected at 164 hr showing pores and lattice fringes.

3.5 Origin of Preferential Dissolution

We observed that by shifting the chemical equilibrium in the reaction solution (*i.e.* by adding more deionized water to the reaction solution at 20 h), NH_4TiOF_3 can be eventually converted to TiO_2 with a hole developed in the same anisotropic manner at the mesocrystal center (data is not shown). As described above, NH_4TiOF_3 mesocrystals are first formed in the reaction solution. However, it is a metastable compound and can be converted to the more thermodynamically stable TiO_2. Thus diluting the reaction solution at 20 h converts the preformed NH_4TiOF_3 to TiO_2. In addition, Figure 3.4 shows that by extending reaction time to 2 months, a substantial amount of TiO_2 is detected in the recovered powder. It is also observed that an increased in the initial concentration of H_3BO_3 also facilitates the conversion of NH_4TiOF_3 to TiO_2, with a hole at the mesocrystal center appearing at a shorter reaction time (10 h instead of 96 h in the typical solution). Indeed, Zhou et al. have reported that NH_4TiOF_3 can be completely converted to TiO_2 by H_3BO_3 aqueous solution in a few hours.[12] Therefore, the appearance and growth of the hole at mesocrystal center are thermodynamically driven by the conversion of preformed NH_4TiOF_3 to TiO_2 and kinetically controlled by the concentration of F-scavenger H_3BO_3.

Energy-dispersive X-ray Spectroscopy (EDS) mapping and line scans (Figure 3.8a-f) for the sample collected at 2 months show that the mesocrystal center where debris accumulate contains more Ti and less F, as compared to the edges. SAED pattern in Figure 3.8i corresponds to the diffraction rings of TiO_2 (anatase), and that in Figure 3.8g corresponds to the single-crystal-like pattern of an NH_4TiOF_3

mesocrystal. This demonstrates that the debris accumulated at the mesocrystal center consists of anatase TiO_2 and the edges remain intact in composition (*i.e.* NH_4TiOF_3) and crystallographic orientation. Furthermore, it is confirmed that dissolution of NH_4TiOF_3 leads to the formation of TiO_2 (anatase) which is a thermodynamically driven process. Elemental analyses of the precipitates collected at various reaction times (namely 11 days and 2 months) are shown in Table 3.1. Contents of N and F generally decrease with reaction time while that of Ti increases. This confirms that NH_4TiOF_3 is being converted to TiO_2.

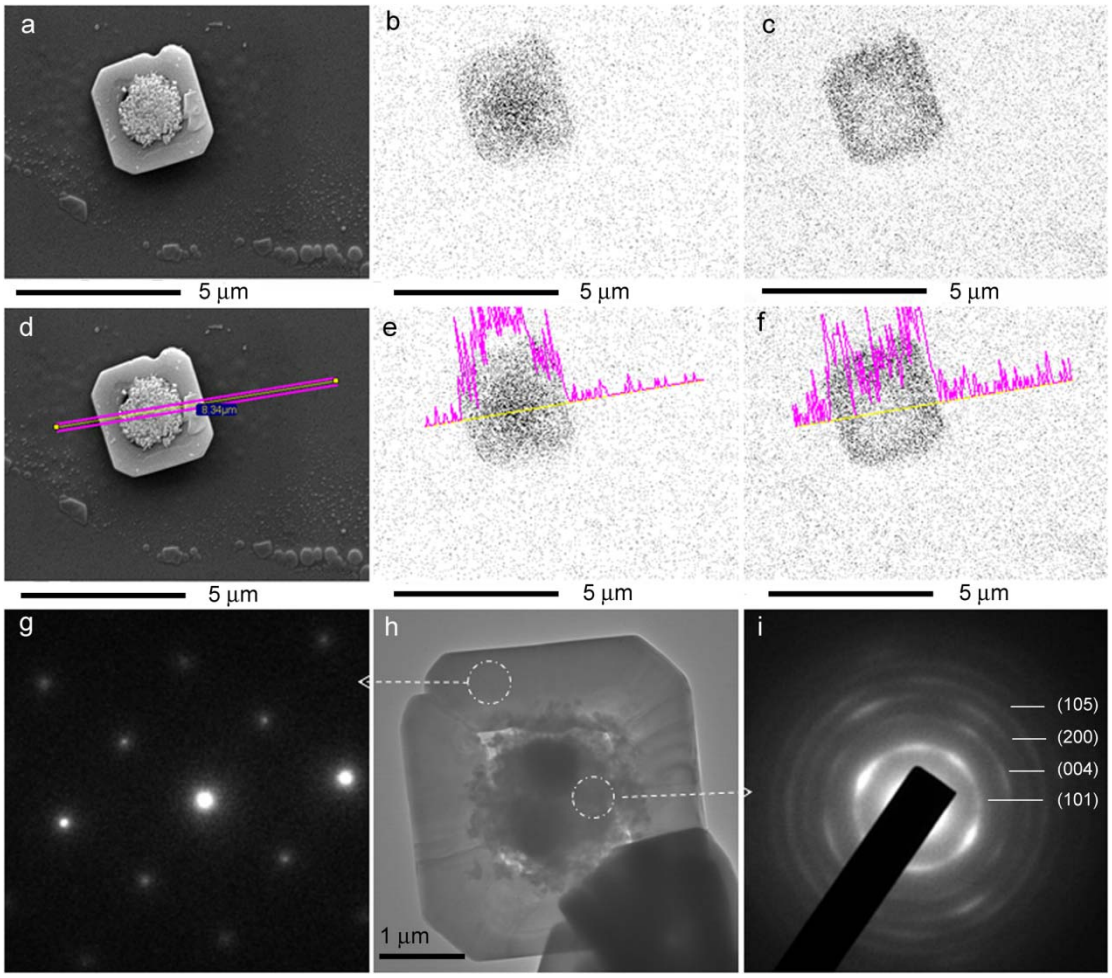

Figure 3.8 Elemental distribution and TEM of NH4TiOF3 mesocrystals collected at 2 months. (a) SEM image; (b) and (c) the corresponding EDS mappings for Ti and F, respectively. (d) the line for line scan; (e) and (f) line scans for Ti and F, respectively. (h) TEM image; (g) SAED for the un-dissolved edge as indicated in (h); (i) SAED for the debris accumulated at the mesocrystal center.

Table 3.1 Elemental analyses of the samples collected at various periods.

Sample	**N (wt%)**	**F (wt%)**	**Ti (wt%)**
9 h	9.4	39.8	30.3
11 days	9.4	39.5	30.7
2 months	7.9	31.3	34.5

With the observed conversion from NH_4TiOF_3 to TiO_2, it may be speculated that *ex-situ* dissolution of NH_4TiOF_3 mesocrystals in deionized water (*i.e.* dispersing them in deionized water) would give rise to a reduction in the contents of N and F elements. Elemental analyses of the as-synthesized mesocrystals collected at 3 h and those further treated in water, as shown in Table 3.2, reveal that the contents of N and F elements are indeed reduced. In addition, as will be discussed later for Figure 3. 10, the hole at mesocrystal center is developed in the same anisotropic manner as that shown in Figures 3.1j and 3.5d. This confirms that NH_4TiOF_3 loses elements N and F to water and suggests that the *in-situ* growth of hole at mesocrystal center is driven by the conversion from NH_4TiOF_3 to TiO_2. Hence, the varying propagation rates of the hole in different crystallographic directions may be closely related to the varying densities of elements N and F.

Table 3.2 Elemental analyses of the sample *3h* collected at 3 h and its water treated derivatives [a]

Sample	N (wt%)	F (wt%)
3h	8.4%	30.5%
3h – D1	7.9%	28.9%
3h – D2	5.7%	21.5%

[a]3h-D1 was prepared by dispersing 27.3 mg of the sample 3h in 1 ml of deionized water for 30 min; 3h-D2 was prepared by dispersing 14.3 mg of sample 3h in 2 ml of deionized water for 5.3 h.

A close examination of the unit cell structure from ref. [59] and [65] and Chapter 6 gives atomic densities of N and F in {010}, {100} and {110} planes and their parallels. The planar densities of both elements follow this order:

{010}={100}>{110} (including their parallels). This corresponds to the observed anisotropic growth rate of the hole at mesocrystal center, *i.e.* faster in <010> and <100> than <110> (see Figure 3.5d) . Therefore, the variation in planar densities of N and F in different crystallographic planes appears to be responsible for the anisotropic growth of the hole at mesocrystal center.

Anisotropic dissolution behavior of single crystals have been reported in published literature. [85-87] The simulation results show that dissolution of a perfect single crystal starts from external faces, vertices and edges.[85] Dissolution of a specific crystallographic face exhibits a specific global dissolution rate[86] while dissolution at vertices and edges results in new faces[85]. For a synthetic single crystal, dissolution initiates via the creation of pits at defected sites and inclusions, and proceeds via retreat of steps which is the rate determining step of the dissolution process.[87] The rate of retreat of steps is related to activation energy following the Arrhenius equation, where the activation energy is determined by the types and number of bonds to be broken during the dissolution process.[25, 26] Therefore, activation energy of the corresponding crystallographic planes in the NH_4TiOF_3 mesocrystals varies with planar densities of N and F elements that are to be lost to water. Consequently, an anisotropic shape of holes arises from the anisotropic rate of dissolution, which is observed in the NH_4TiOF_3 mesocrystals in the present work.

Figure 3.9 shows the dissolution pits formed in an NH_4TiOF_3 mesocrystal collected at 96 h, where the arrows indicate individual pits while the circle indicates coalesced pits. The rather diffuse SAED pattern by TEM gives no clear clue on the composition of the debris concentrated at center, due to the limited degree of crystallization.

According to the XRD phase analysis for the sample collected at 2 months, the debris may well be TiO_2 that precipitates due to the increased local supersaturation. This increase in local supersaturation is attributed to the local dissolution of NH_4TiOF_3 mesocrystal as revealed by the formation of pits. A recent report by Feng et al. [65] shows that an organic free route also leads to the formation of NH_4TiOF_3 mesocrystals with dominant (001) surfaces. In their study, the dissolution pits caused by defects are randomly located on the surfaces. In contrast, the dissolution pits in the present work initiate and concentrate at center.

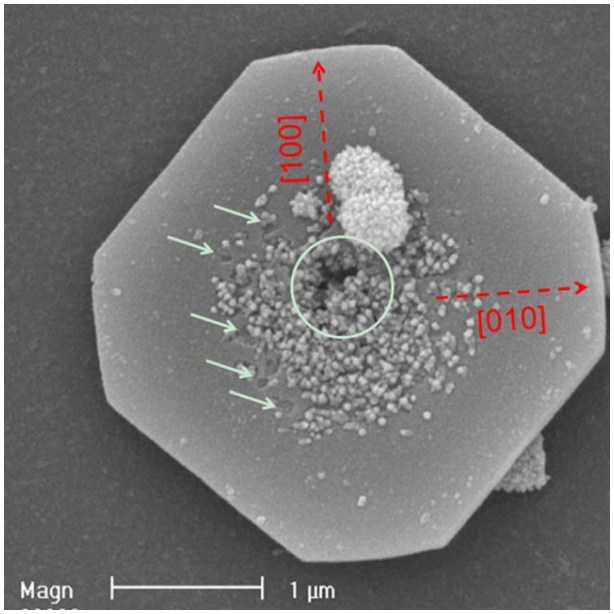

Figure 3.9 SEM image shows the dissolution pits of a mesocrystal collected at 96 h.

Elemental analysis using CHNS method shows that the carbon content is 0.17(±0.05) wt% and 0.07(±0.05) wt% for the samples collected at 3 h and 9 h, respectively. Obviously, carbon is associated with the occluded surfactant molecules in the mesocrystal. There could be two scenarios for this phenomenon: (i) carbon is

distributed uniformly; and (ii) there is a gradual decrease in carbon content from center towards the edges of the mesocrystals. According to Zhou et al., the growth of NH_4TiOF_3 mesocrystals evolves from hybrid mesophases, where the separation of organic and inorganic materials is required.[59] However, as shown in Figure 3.3, the mesocrystals, assembled from nano-particles with the aid of Brij 58 molecules,[59] grow the fastest at the initial stage. This suggests that, at the initial growth stage, occluded surfactant molecules may not readily separate from the growing mesocrystal. Thus, the second scenario, i.e., there is a higher concentration of surfactant molecules in the central region of the mesocrystal, is more likely. The occluded surfactants impose unstable interfaces between inorganic NH_4TiOF_3 and organic surfactant molecules and consequently facilitate the dissolution of this structure. The appearance of dissolution pits at the mesocrystal center supports this idea. In the work on copper oxalate mesocrystals reported by Soare et al., a random ordered core caused by rapid growth in the initial stage is proposed to be responsible for the dissolution at center.[81] In contrast, the mesocrystal core in the present work is well aligned (see Figure 3.10c).

For the *in-situ* dissolution, we have considered two important aspects. One is the anisotropic growth of dissolution hole at the mesocrystal center caused by anisotropic distribution of N and F in the respective dissolution planes, where the densities of N and F affect the activation energy of dissolution of the respective planes. The other consideration is the amount of inclusions accumulated at the mesocrystal center. To further understand the process, we conducted *ex-situ* dissolution studies with the washed NH_4TiOF_3 mesocrystals.

The as-synthesized mesocrystals obtained at 9 h were dispersed in water and examined with SEM and TEM. Figures 3.10d and 3.10i show two mesocrystals: the as-synthesized and the further treated (in water for 1 h), respectively. The single-crystal-like SAED pattern in Figure 3.10c is indexed and shows that the diagonals across the truncated corners are in [100] and [010] directions. The SAED patterns in Figures 3.10a and 3.10b are the same as that in Figure 3.10c. This consistency reveals that the crystallites in the examined areas (*i.e.* corners and center) are all oriented in the same crystallographic register, which is characteristic of a mesocrystal. The as-synthesized mesocrystal is intact. In contrast, the water-treated mesocrystal, as shown in Figure 3.10i, has been dissolved anisotropically in the center and near the edges, leaving an exterior "skin". The same change applies to the SEM observations in Figures 3.10k and 3.10l. In addition, Figure 3.10j shows that the exterior "skin", highlighted by the ellipse in Figure 3.10i, has also partially dissolved. The anisotropic dissolution in center (Figure 3.10i) is consistent with what is observed in the as-synthesized mesocrystals obtained at 164 h (Figure 3.5d), *i.e.* a faster dissolution in the directions of truncated corners, namely [010] and [100]. The SAED patterns for the skin (Figure 3.10e), center (Figure 3.10f), and truncated corner (Figure 3.10g) are the same and correspond to [001] zone of NH_4TiOF_3. Figures 3.10m and 3.10n show the bright field and dark field TEM images, respectively, for a water-treated 9 h mesocrystal, where the dark field image reveals the portions that are being dissolved: center, skin, and diagonals (*i.e.* in [100] and [010] directions). As discussed above, the mesocrystal center contains the highest concentration of occluded surfactant molecules and initiates dissolution in water due

to its poorest stability. The anisotropic shape of the dissolution hole is caused by the variation of activation energy for dissolution of different planes, where the activation energy is affected by the planar densities of N and F elements.

Extended *ex-situ* dissolution resulted in a gap that separates the exterior "skin" from the interior during the dissolution process. The exterior "skin" is connected to the interior at the truncated corners and its crystallographic orientation is the same as the interior, as shown by the SAED patterns (Figures 3.10e, 3.10f and 3.10g). This suggests that the "skin" is left from the partial dissolution of the original external edges. This phenomenon contradicts the case whereby the external edges are structurally the same as the interior. In the latter, the external surface sacrifices itself to protect the interior and a gap between the interior and the external edges should not appear. Therefore, in the current case, the external edges must be structurally different from the interior. Moreover, the external edges are more stable in comparison to the interior edges and may well be improved in crystallinity. In fact, it is widely known that the external parts of mesocrystals have improved crystallinity due to the "dissolution and re-crystallization" process.[14, 19, 20] This "gap" phenomenon of dissolution is only observed in our *ex-situ* dissolution study, where the growth rate of external edges is zero.

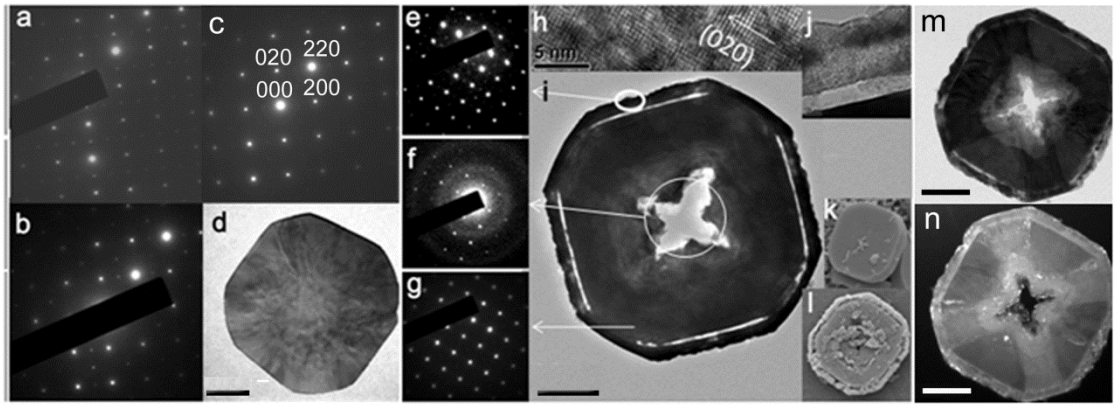

Figure 3.10 TEM, SAED patterns and SEM images. (a)-(d): a mesocrystal collected at 9 h; (c) SAED for the mesocrystal center, and (a) and (b) for two truncated corners. (i): TEM of a mesocrystal collected at 9 h, washed and then dispersed in water for 1 h (14.0 mg in 1 ml water); (e), (h) and (j) are from the "skin" highlighted by the ellipse in (i); (k) and (l) are SEMs before and after immersion in water for 1 h, respectively. (m) and (n) are bright and dark field TEM images (using source from diffraction spot (220)), respectively, of a mesocrystal collected at 9 h, washed and then dispersed in water for 30 min (14.7 mg in 1 ml water). Scale bars are 0.5 μm.

The inset in Figure 3.3 shows that growth rate of mesocrystal length approaches zero but never falls below zero throughout the observation period (*i.e.* 164 h). It reveals that *in-situ* growth rate at edges overcompensates or at least equals to the dissolution rate. This is a statistically macroscopic observation which counts for the typical morphologies of only inner net dissolution as shown in Figure 3.1. However, we have also observed several mesocrystals that exhibit both inner and outer net dissolution *in-situ*, as shown in Figure 3.11. These two types of dissolution both propagate faster in the directions of corners corresponding to <100> and <010> crystallographic directions.

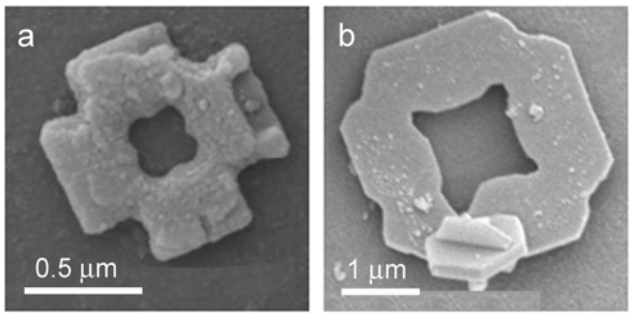

Figure 3.11 SEM images of particles showing *in-situ* inner and outer net dissolution.

3.6 Remarks

Anisotropic dissolution of NH_4TiOF_3 mesocrystals is observed in both *in-situ* and *ex-situ* studies. In both cases, dissolution initiates from the mesocrystal center, where the concentration of occluded surfactant molecules is the highest. At the earlier stage of mesocrystal growth, the growth rate competes favorably against the dissolution rate. However, with the extension of mesocrystal growth, as shown by the *in-situ* study, the net growth rate approaches zero and apparent dissolution is observed at mesocrystal center. As further shown by the *in-situ* studies, dissolution is observed only when the dissolution rate exceeds the growth rate. As a result of the two competing processes, dissolution is not observed in the initial stage of rapid growth rate, but appears at the later stage of slow growth rate. This is followed by the propagation of dissolved hole in the mesocrystal center. The dissolution propagates preferentially in the <100> and <010> directions, where it is thermodynamically driven by conversion of NH_4TiOF_3 to more stable TiO_2 via losing N and F elements. The observed anisotropic behavior is caused by the difference in activation energy of the corresponding planes that are being dissolved. The activation energy appears to

be associated with the planar densities of N and F elements in NH_4TiOF_3 mesocrystals.

CHAPTER 4. MANIPULATING THE FORMATION OF NH_4TIOF_3 MESOCRYSTALS: EFFECTS OF TEMPERATURE, SURFACTANT, AND PH

4.1 Background

As mentioned above, mesocrystals are a new class of crystals assembled from small units that are crystallographically oriented.[3, 4] Unless the small units are stabilized, such mesocrystals usually fuse to form 'single crystals' due to the high lattice energy of inorganic constituents involved.[35] The additives in between the small units are excluded from the surfaces that fuse during the fusion process.[3] However, due to the size or shape variation of the small units, the resultant 'single crystals' may inevitably contain pores – a feature that is not commonly observed for the single crystals that are grown via an ion-by-ion route (i.e., the classical crystallization process). Nevertheless, Colfen et al. consider these micro-porous structures as single crystals[88] unless the pores are prominent (e.g. DL-alanine and V_2O_5 mesocrystals)[35, 89]. Inumaru[6] has proposed the concept 'sponge crystals' to describe such 'single crystals' and categorized them under the class 'mesocrystal'. In this chapter, we consider such 'single crystals' as mesocrystals highlighting their porous feature which is drastically distinct from those of single crystals grown via the classical route. Recently, Colfen and coworkers discussed three approaches for the densification of V_2O_5 mesocrystals,[89] namely, (i) addition of salt NaCl to decrease the

Debye length of the electrical double layer (EDL) in the V_2O_5 sol; (ii) application of a strong sedimentation force by centrifugation to reduce the inter-particle distance; and (iii) introduction of an acrylic acid/sulfonic acid copolymer for particle alignment and densification. As discussed below, we however demonstrate that size and volume of the mesopores can also be manipulated by variation in pH value of the reaction solution.

In the previous chapter, we demonstrated that the NH_4TiOF_3 mesocrystals undergo a thermodynamically driven process, i.e., dissolution and precipitation, to form TiO_2. This phenomenon has inspired us to manipulate the stability of NH_4TiOF_3 nanocrystals by adjusting processing parameters involved and to study their effects on the formation and growth of NH_4TiOF_3 mesocrystals. We find that increasing the pH or temperature of the reaction solution can chemically destabilize the NH_4TiOF_3 nanocrystals and convert them into TiO_2 nanoparticles. The resultant TiO_2 nanoparticles are crystallographically different from the NH_4TiOF_3 nanocrystals. Consequently, they would not participate in the mesoscale assembly process that leads to the formation of NH_4TiOF_3 mesocrystals via oriented attachment and crystallographic fusion,[59] but interact with each other to eventually form TiO_2 aggregates. There are two apparently competitive processes that take place in the reaction solution and lead to the formation of NH_4TiOF_3 mesocrystals and TiO_2 aggregates with their relative amounts depending on the pH and temperature of the reaction solution as well as the presence of surfactant Brij 58 molecules. The two processes (in the presence of Brij 58) are schematically shown in Scheme 4.1.

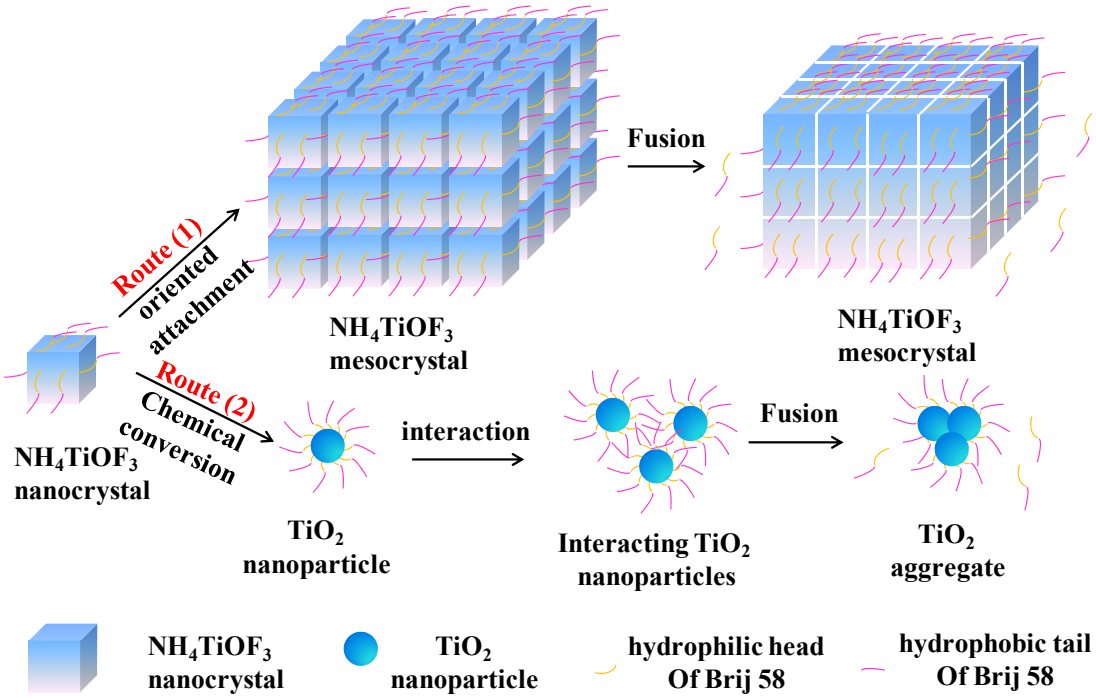

Scheme 4.1 The two competitive routes that take place in the reaction solution (in the presence of surfactant Brij 58). Route (1): formation of NH_4TiOF_3 mesocrystals; Route (2): formation of TiO_2 aggregates. The size of surfactant Brij 58 molecules has been exaggerated in the drawing and the shape does not represent the truth in aqueous solution. Similar scheme applies to the case whereby Brij 58 is not present.

4.2 Experimental Details

The solid particles were grown in an aqueous solution, according to what has been reported.[59] Typically, an aqueous solution of surfactant Brij 58 (3 g in 10 g of deionized water, Aldrich) was first prepared at 23˚C. An appropriate amount of fluoride scavenger H_3BO_3 (123.7 mg, 99.8%, Merck) was then dissolved in the surfactant solution. $(NH_4)_2TiF_6$ (198.0 mg, 99.99%, Aldrich) was then subsequently added, and upon its complete dissolution, ammonia solution (28%, Ajax) was added dropwise. The amount of ammonia solution was varied: 0, 80, 160 and 240 μL. After the solution was well mixed, particles were allowed to grow under static condition

for 3 days at 4˚C or 23˚C. For the study without surfactant Brij 58, only the step of adding Brij 58 was omitted and the other steps were kept unchanged in the same procedure. The resultant solid particles were then recovered by centrifugation and washing successively for three times. Solvents used for washing were water, acetone and ethanol. Drying was carried out at 60˚C for 12 h. Calcination of the solid particles was operated at 500˚C or 700˚C for 5 h with a ramp rate 2˚C/min.

4.3 Characterization of NH_4TiOF_3 Mesocrystals and TiO_2 Particles

At 4˚C in the presence of Brij 58, the size of the solid particles derived from the solution decreases upon the addition of ammonia solution (Figure 4.1a-d). At 0 μL of ammonia solution, particles of rather uniform size and morphology are observed. The morphology is of rod with circular top surfaces. It has been reported by Zhou et al. that these particles are NH_4TiOF_3 mesocrystals.[60] At 80 μL of ammonia solution, the particle size is decreased and the top surfaces appear of squares. Pores which reveal the porous interior are readily observed on the surfaces. At 160 μL, the porous structure is retained, but the particle size has been decreased further and nanoparticles appear. At 240 μL, there are only aggregates of nanoparticles. XRD shows that the crystalline phase is dependent on the amount of ammonia solution added, i.e., crystalline NH_4TiOF_3 for 0, 80 and 160 μL and poorly-crystallized TiO_2 (anatase) for 240 μL (Figure 4.3a).

In the absence of Brij 58 at 4˚C, the addition of ammonia solution also decreases the particle size (Figure 4.1e-h). At 0 μL of ammonia solution, the rods with circular top surfaces heavily aggregate. Upon the addition of ammonia solution, the particles

are turned into aggregates of nanoparticles regardless of the amount of ammonia solution added. Comparing the samples synthesized with and without Brij 58 for 80 μL and 160 μL of ammonia solution (Figure 4.1b & f, Figure 4.1c & g, respectively), it is inferred that Brij 58 molecules help the assembly of individual nanoparticles into hierarchical superstructures. However, when the amount of ammonia solution added is too high (240 μL), this function of Brij 58 is lost (Figure 4.1d). XRD shows that the crystalline phase is dependent on the amount of ammonia solution added, i.e., is crystallized NH_4TiOF_3 for 0 and 80 μL and poorly-crystallized TiO_2 (anatase) for 160 and 240 μL (Figure 4.3b).

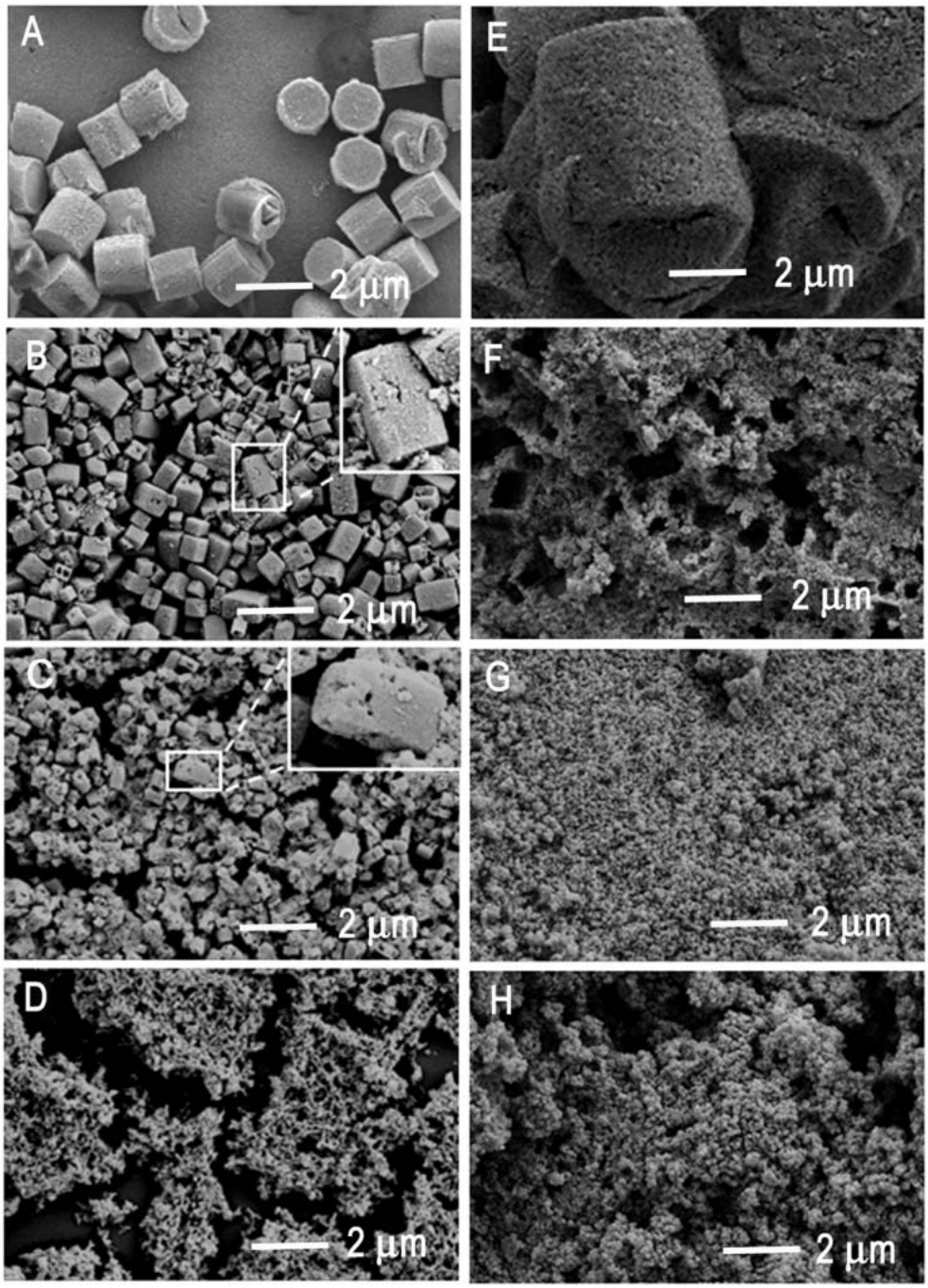

Figure 4.1 SEM images of the as-synthesized particles grown at **4**°**C**. (a) - (d) in the presence of surfactant Brij 58. (e) - (h) in the absence of surfactant Brij 58. The amount of ammonia solution added into the reaction solutions: (a) & (e) 0 μL, (b) & (f) 80 μL, (c) & (g) 160 μL, (d) & (h) 240 μL.

At 23˚C in the presence of Brij 58, the addition of ammonia solution also decreases size of the particles (Figure 4.2a-d). At 0 μL of ammonia solution, particles of rather uniform size and morphology are observed. The morphology is rod-like with circular top surfaces. At 80 μL, the size has been decreased and the morphology changes to plates with square top surfaces. Pores are also readily observed. From 160 μL onwards, the only observable morphology is aggregates of nanoparticles. XRD shows that the crystalline phase is crystalline NH_4TiOF_3 for 0 and 80 μL and poorly-crystallized TiO_2 (anatase) for 160 and 240 μL of ammonia solution (Figure 4.3c).

In the absence of Brij 58 at 23˚C, the addition of ammonia solution again decreases size of the particles (Figure 4.2e-h). At 0 μL of ammonia solution, plates with square top surfaces heavily aggregate. Upon the addition of ammonia solution, the particles are turned into aggregates of nanoparticles regardless of the amount of ammonia solution added. Comparing the samples obtained at 23˚C with and without Brij 58 for 80 μL of ammonia solution (Figure 4.2b & f), it appears that Brij 58 molecules help the assembly of individual nanoparticles into hierarchical superstructures. However, when the amount of ammonia solution is too high (160 μL and 240 μL), this function of Brij 58 disappears (Figure 4.2c & d). XRD shows that the crystalline phase is crystalline NH_4TiOF_3 for 0 μL and poorly-crystallized TiO_2 (anatase) for 80, 160 and 240 μL (Figure 4.3d).

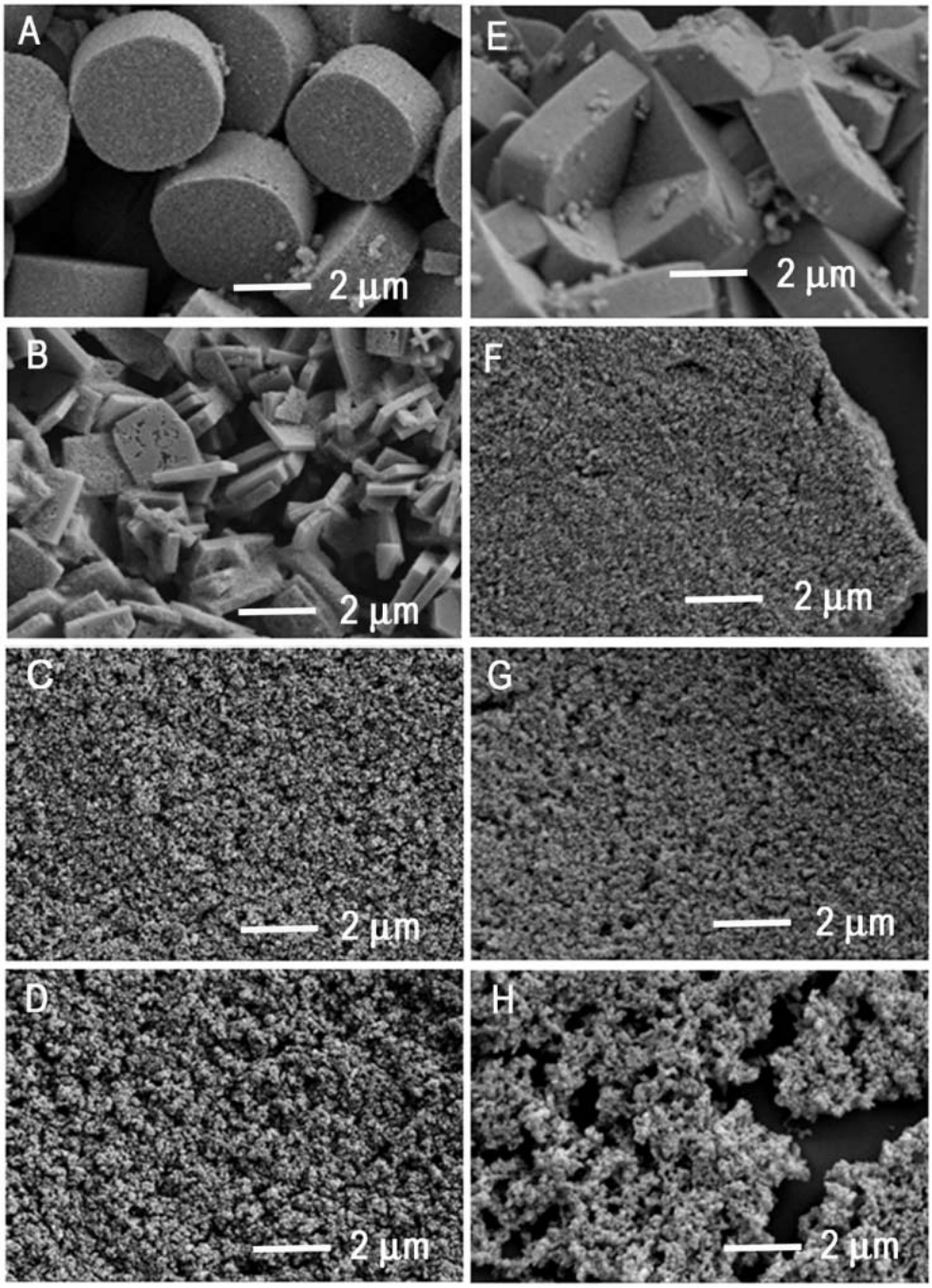

Figure 4.2 SEM images of the as-synthesized particles grown at **23˚C**. (a)-(d) in the presence of surfactant Brij 58; (e)-(h) in the absence of surfactant Brij 58. The amount of ammonia solution added into the reaction solutions: (a) & (e) 0 μL, (b) & (f) 80 μL, (c) & (g) 160 μL, (d) & (h) 240 μL.

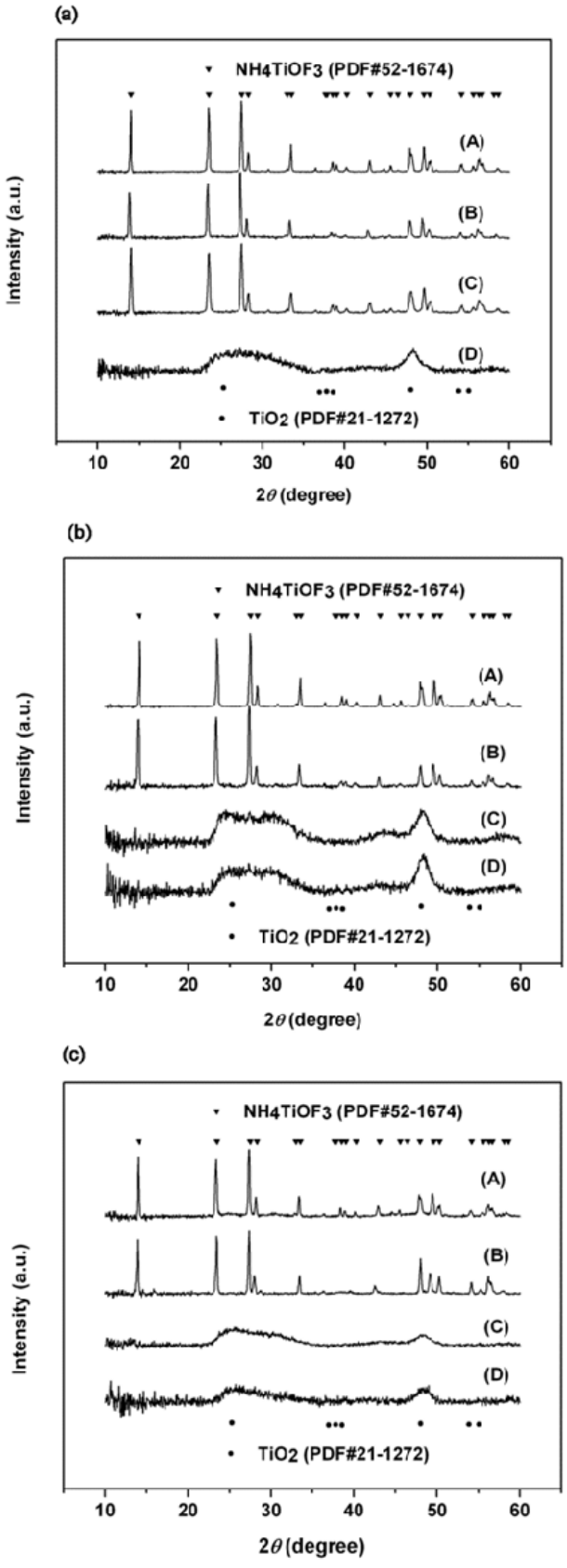
(a)
NH4TiOF3 (PDF#52-1674)
(A)
(B)
(C)
(D)
TiO2 (PDF#21-1272)
Intensity (a.u.)
10
20
30
40
50
60
2θ (degree)
(b)
NH4TiOF3 (PDF#52-1674)
(A)
(B)
(C)
(D)
TiO2 (PDF#21-1272)
Intensity (a.u.)
10
20
30
40
50
60
2θ (degree)
(c)
NH4TiOF3 (PDF#52-1674)
(A)
(B)
(C)
(D)
TiO2 (PDF#21-1272)
Intensity (a.u.)
10
20
30
40
50
60
2θ (degree)

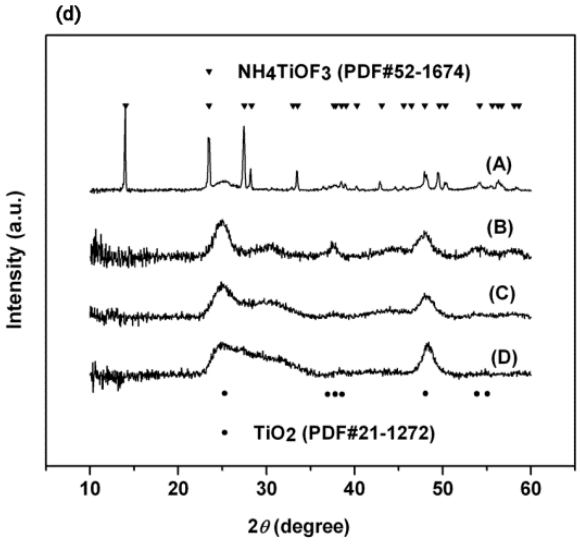

Figure 4.3 XRD of the as-synthesized particles grown at various conditions. (a) 4˚C with Brij 58, (b) 4˚C without Brij 58, (c) 23˚C with Brij 58, (d) 23˚C without Brij 58. The amount of ammonia solution added into the reaction solutions: (A) 0 μL, (B) 80 μL, (C) 160 μL, (D) 240 μL.

Table 4.1 Summary of the particles grown at various conditions

Reaction Condition	**Crystalline Phase(s)**	**Morphology**
Brij 58, $NH_3 \cdot H_2O$ (0 μL), 4˚C	NH_4TiOF_3	mesocrystal
Brij 58, $NH_3 \cdot H_2O$ (80 μL) , 4˚C	NH_4TiOF_3	mesocrystal
Brij 58, $NH_3 \cdot H_2O$ (160 μL) , 4˚C	NH_4TiOF_3	mesocrystal
Brij 58, $NH_3 \cdot H_2O$ (240 μL) , 4˚C	TiO_2	aggregates
$NH_3 \cdot H_2O$ (0 μL) , 4˚C	NH_4TiOF_3	aggregated mesocrystal
$NH_3 \cdot H_2O$ (80 μL) , 4˚C	NH_4TiOF_3	aggregates
$NH_3 \cdot H_2O$ (160 μL) , 4˚C	TiO_2	aggregates
$NH_3 \cdot H_2O$ (240 μL) , 4˚C	TiO_2	aggregates
Brij 58, $NH_3 \cdot H_2O$ (0 μL), 23˚C	NH_4TiOF_3	mesocrystal
Brij 58, $NH_3 \cdot H_2O$ (80 μL) , 23˚C	NH_4TiOF_3	mesocrystal
Brij 58, $NH_3 \cdot H_2O$ (160 μL) , 23˚C	TiO_2	aggregates
Brij 58, $NH_3 \cdot H_2O$ (240 μL) , 23˚C	TiO_2	aggregates
$NH_3 \cdot H_2O$ (0 μL) , 23˚C	NH_4TiOF_3 & TiO_2	aggregated mesocrystal
$NH_3 \cdot H_2O$ (80 μL) , 23˚C	TiO_2	aggregates
$NH_3 \cdot H_2O$ (160 μL) , 23˚C	TiO_2	aggregates
$NH_3 \cdot H_2O$ (240 μL) , 23˚C	TiO_2	aggregates

The hierarchical superstructures represented in Figure 4.1b &c (synthesis condition: with Brij 58; 4˚C; $NH_3 \cdot H_2O$ 80 μL and 160 μL, respectively) and 2b (synthesis condition: with Brij 58; 23˚C; $NH_3 \cdot H_2O$ 80 μL) are identified to be NH_4TiOF_3 mesocrystals, as shown by the single-crystal-like diffraction patterns in Figure 4.4a-c. The nanoparticles which appear in Figure 4.1c (synthesis condition: with Brij 58; 4˚C; $NH_3 \cdot H_2O$ 160 μL) are also identified to be NH_4TiOF_3 mesocrystals although the morphology is not well defined (Figure 4.4d). The

crystallographic orientations are indicated in the respective panels, suggesting a large portion of the {001} facets. Their porous interiors are also revealed by the low contrast regions. In accordance with the XRD diffraction (Figure 4.3a-D), the aggregates of nanoparticles represented in Figure 4.1d (synthesis condition: with Brij 58; 4˚C; $NH_3 \cdot H_2O$ 240 μL) are extremely poor in crystallinity (Figure 4.4e). However, their crystallinity can be effectively enhanced by thermal treatment at 200˚C for 2 h, as suggested by the diffraction rings of TiO_2 (anatase) (Figure 4.4f). Table 4.1 summarizes the characteristics of all structures synthesized at various conditions.

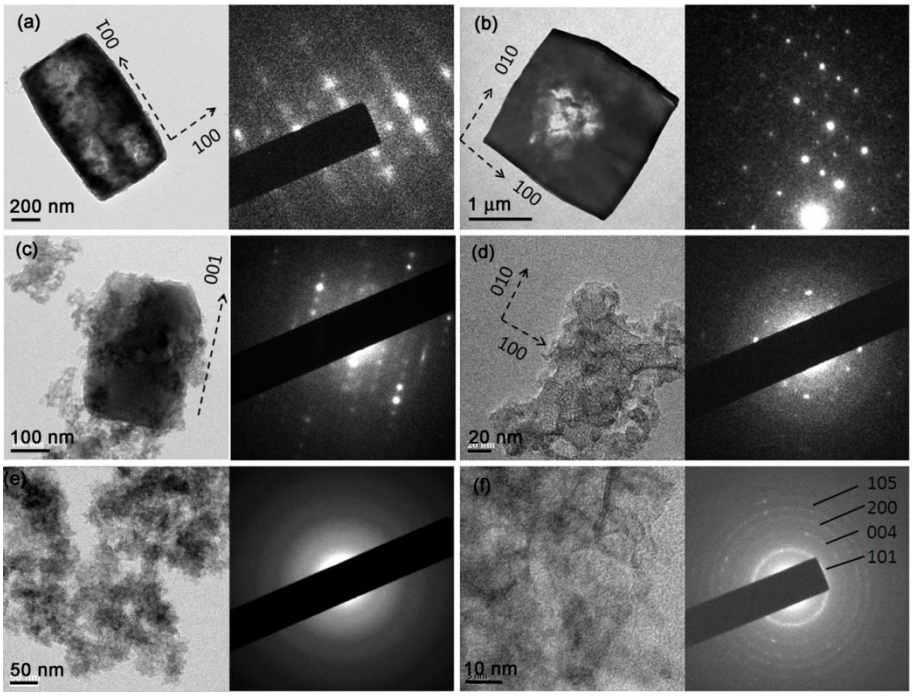

Figure 4.4 TEM and diffraction patterns of the particles grown at various conditions. (a) 4˚C with Brij 58, amount of ammonia solution is 80 μL; (b) 23˚C with Brij 58, amount of ammonia solution is 80 μL; (c) & (d) 4˚C with Brij 58, amount of ammonia solution is 160 μL; (e) 4˚C with Brij 58, amount of ammonia solution is 240 μL; (f) thermally treated sample of (e) at 200˚C for 2 h. The extra diffraction spots arise from double diffraction caused by thickness.

4.4 Factors Affecting Phases: Temperature, Surfactant, and pH

There are three major parameters which largely determine the formation of NH_4TiOF_3 hierarchical superstructures (i.e., NH_4TiOF_3 mesocrystals). One is the presence of Brij 58. As suggested by Zhou et al., Brij 58 surfactant molecules can adsorb preferentially onto the different crystallographic planes of NH_4TiOF_3 nanocrystals and assemble them into NH_4TiOF_3 mesocrystals via the interaction of hydrophobic tails.[59] Before the NH_4TiOF_3 nanocrystals are converted to TiO_2 nanoparticles, they can be assembled, with the aid of Brij 58 molecules, into NH_4TiOF_3 mesocrystals which fuse to exclude the inter-unit Brij 58 molecules (Scheme 4.1, Route 1). Otherwise, they would be converted to TiO_2 nanoparticles and form aggregates (Scheme 4.1, Route 2). The second parameter is temperature. In the presence of Brij 58, NH_4TiOF_3 mesocrystals form preferentially at the lower temperature 4˚C. The chemical conversion from NH_4TiOF_3 to TiO_2 is a thermally activated process whereby the rate increases with temperature according to the Arrhenius relationship. Raising temperature kinetically enhances the conversion process and thereby decreases the chemical stability of NH_4TiOF_3 nanocrystals. The third parameter is the pH value of the reaction solution which is controlled by the amount of ammonia solution added. Generally, increasing the pH level deteriorates the formation of NH_4TiOF_3 mesocrystals and the gradual change is the most significant when synthesized in the presence of Brij 58 at 4˚C. The pH of the aqueous solution, whereby 36.5 mg of NH_4TiOF_3 mesocrystals is dispersed in 10 g of deionized water for 6 h, is measured to be 4.0. Little increment (< 0.2) in pH value is observed till 4 days. XRD (Figure 4.5) shows that the dominant crystalline phase at 6

h is NH_4TiOF_3 with a little hump at 2θ of around 25.3˚ corresponding to (101) peak of TiO_2 (anatase). However, after 4 days, only TiO_2 (anatase) is observed. This proves that NH_4TiOF_3 is metastable and readily converted to TiO_2 (anatase). Furthermore, when the same amount of NH_4TiOF_3 mesocrystals is dispersed in a diluted ammonia solution (pH=11.9), a short reaction time (6 h) gives rise to poorly-crystallized TiO_2 (anatase) (Figure 4.5). This observation suggests that a basic environment facilitates the conversion from NH_4TiOF_3 to TiO_2. This phenomenon can be explained as follows. Similar to the hydrolysis of the precursor $(NH_4)_2TiF_6$ (or so-called 'ligand exchange' with water) whereby F^- is replaced by OH^- from water producing H^+,[59] conversion from NH_4TiOF_3 to TiO_2 also gives rise to H^+ as indicated by the acidic solution of NH_4TiOF_3 mesocrystals dispersed in water. The addition of basic ammonia solution will facilitate the conversion process. Therefore, it is highly possible that the fair crystallinity observed by TEM (Figure 4.4) arises from hydrolysis and partial removal of fluorine and nitrogen from the NH_4TiOF_3 mesocrystals. In the discussions below, we will look at the effect of pH at a fixed temperature 4˚C in the presence of Brij 58. The pH is adjusted by the amount of ammonia solution (28%) added. Similar phenomenon can be observed when KOH (6.1 M) is employed (Figure 4.6).

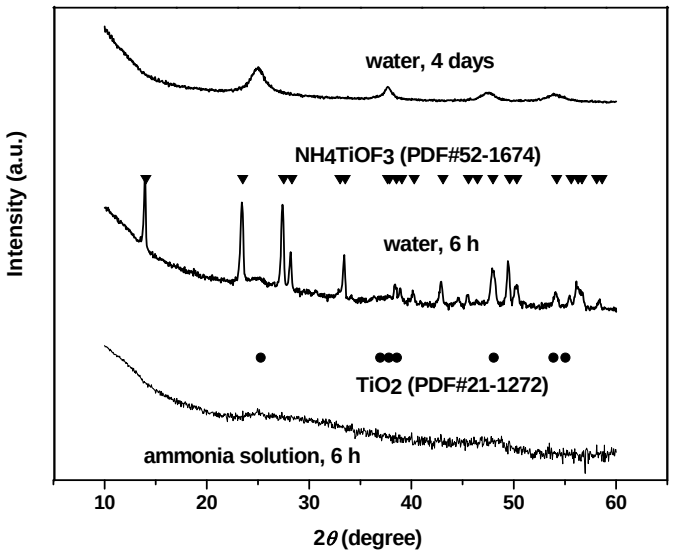

Figure 4.5 XRD traces of NH_4TiOF_3 mesocrystals dispersed in deionized water and diluted ammonia solution (pH=11.9). Amount of NH_4TiOF_3 mesocrystals: 36.5 mg; amount of dispersant: 10 g.

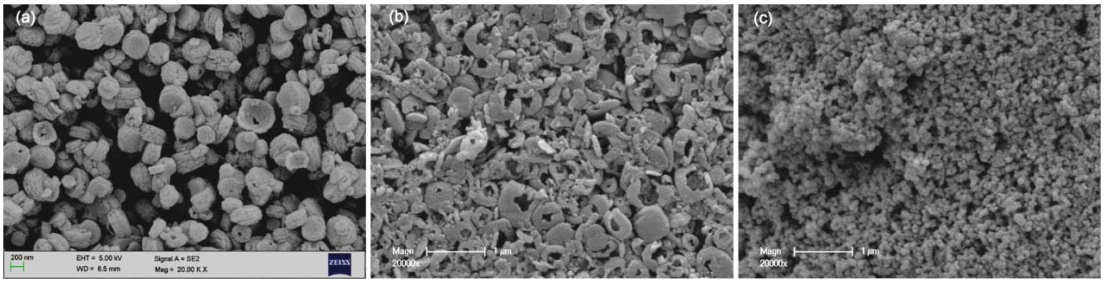

Figure 4.6 As-synthesized particles prepared at 4 ˚C in the presence of Brij 58. The solution pH was controlled by the amount of KOH solution (6.1 M). The amounts of KOH solution: (a) 80 μL; (b) 240 μL; (c) 720 μL. (a) and (b) are NH_4TiOF_3 mesocrystals; (c) aggregates of TiO_2 (anatase) nanoparticles.

Elemental analyses confirm the above XRD and TEM results. The results for the as-synthesized particles prepared at 4˚C in the presence of Brij 58 with ammonia solution 80 μL and 240 μL are shown in Table 4.2. The distinct differences are the

amount of fluorine and nitrogen. The as-synthesized precursor prepared at 80 μL contains large amounts of fluorine and nitrogen (30.7% and 9.0%, respectively), which is characteristic of NH_4TiOF_3. In contrast, the as-synthesized precursor prepared at 240 μL contains rather small amounts of fluorine and nitrogen (0.3% and 3.0%, respectively), which suggests a dominant constituent of TiO_2. In addition, thermal treatment of the precursors at 500˚C for 5 h removes fluorine and nitrogen rather effectively. However, residue fluorine is still detectable and its amount decreases with the amount of ammonia solution added into the reaction solutions (2.4% for 80 μL and 0.2% for 240 μL). At a higher temperature, e.g., 700˚C, further reduction in fluorine content is observed for 80 μL (0.4%) and no change for 240 μL. The amount of fluorine affects the photocatalytic performance of these TiO_2 products, as will be discussed in Figure 4.10. The larger amount of hydrogen in the precursor prepared at 240 μL of ammonia solution suggests that this precursor comprises more hygroscopic TiO_2, which is also supported by the FTIR and TGA results.

Table 4.2 Elemental analyses of the as-synthesized particles (precursors) prepared with Brij 58 at 4 ˚C and their thermally treated derivatives (500 ˚C or 700 ˚C for 5 h)

Sample	**H (wt%)**	**N (wt%)**	**F (wt%)**
Precursor (80 μL)	2.7	9.0	30.7
TiO_2 (80 μL, 500˚C)	<0.5	<0.5	2.4
TiO_2 (80 μL, 700˚C)	<0.5	<0.5	0.4
Precursor (240 μL)	3.6	3.0	0.3
TiO_2 (240 μL, 500˚C)	<0.5	<0.5	0.2
TiO_2 (240 μL, 700˚C)	<0.5	<0.5	0.2

FTIR spectra (Figure 4.7) also reveal that the phases of the as-synthesized products, prepared in the presence of Brij 58 at 4˚C, vary with the amount of ammonia solution added in the synthesis process. The IR-absorption bands at wavenumbers of 3290, 3199 and 3087 cm^{-1} for the samples prepared at 0 and 80 μL are ascribed to the stretching modes of NH_4^+.[66, 70, 90, 91] The band at 3153 cm^{-1} for the samples prepared at 160 and 240 μL is also ascribed to the stretching mode of NH_4^+.[90] The former three bands (3290, 3199 and 3087 cm^{-1}) have shrinked into one (3153 cm^{-1}) probably because the NH_4^+ groups in the as-synthesized particles (160, 240 μL) have been destroyed as shown by the dramatically reduced amount of nitrogen (Table 4.2). The bands at 1417 and 2858 cm^{-1} are ascribed to the bending mode of NH_4^+ and its overtone band, respectively.[66, 70, 90, 91] The band at 895 cm^{-1} in the samples prepared at 0, 80 and 160 μL is attributed to the stretching mode of Ti=O (terminal oxygen) [66, 70] or Ti-O-Ti antisymmetric stretching[92]. For the same samples, the band at 758 cm^{-1} corresponds to a combination of lattice modes of Ti-O and Ti-F.[70] The band at 600 cm^{-1}, which is attributed to Ti-F, [66, 70] disappears in the sample prepared at 240 μL. This is consistent with the results of elemental analysis that the amount of fluorine in that sample is close to 0 (Table 4.2). The bands at 509, 504 and 454 cm^{-1} are due to Ti-O.[93, 94] The relative intensity at 500 cm^{-1} with respect to that at 3150 cm^{-1} is greatly enhanced in the sample prepared at 240 μL. This observation strongly supports our previous speculations that this sample contains less nitrogen. Furthermore, the band at 3432 cm^{-1} is ascribed to O-H stretching of adsorbed water and the hydroxyl groups,[90, 95] and the band at 1646 cm^{-1} is attributed to H-O-H bending[90] or deformation of the adsorbed water and the hydroxyl groups[66, 95]. These two bands are

much stronger for the sample prepared at 240 μL in comparison to the rest. This observation is consistent with the hygroscopic nature of TiO_2.[96] In addition, no detectable amount of Brij 58 can be observed in these spectra suggesting that the surfactant molecules are effectively excluded from the inorganic products.

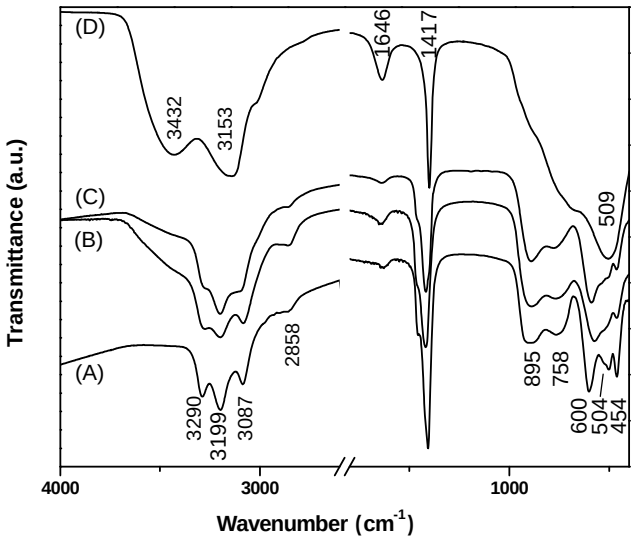

Figure 4.7 FTIR of the particles synthesized with Brij 58 at 4˚C. Amount of ammonia solution added: (A) 0 μL, (B) 80 μL, (C) 160 μL, (D) 240 μL.

Thermogravimetric analyses (TGA) of the as-synthesized solid particles prepared at 4˚C in the presence of Brij 58 are presented in Figure 4.8. In the lower temperature range (< 250˚C), the weight loss increases with the amount of ammonia in the solution. As discussed previously, the major contribution for this weight loss can be attributed to water, the reason being the progressive removal of nitrogen and fluorine with increasing pH in the synthesis process results in more Ti-O bonds which

contribute to the hygroscopic nature of TiO_2. In the higher temperature range (250-500˚C) whereby the thermal treatment removes nitrogen and fluorine, weight loss decreases with the amount of ammonia solution. This supports our previous speculation that OH^- facilitates the conversion from NH_4TiOF_3 to TiO_2 whereby the amount of nitrogen and fluorine lost to the reaction solution increases with an increase in the amount of ammonia solution.

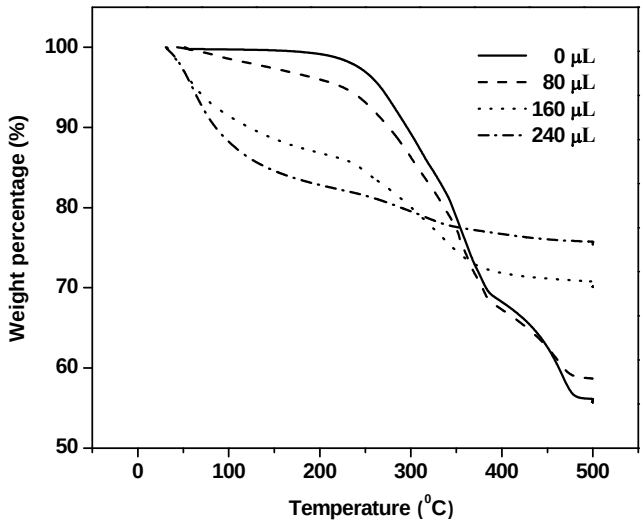

Figure 4.8 TGA of the solid particles synthesized in the presence of Brij 58 at 4˚C.The mass loss of these solid particles against rising temperature is dependent on the amount of ammonia added in the solution.

pH values of the reaction solutions and zeta potential were measured after the added ammonia solution was well mixed (Table 4.3). Apparently, the ammonia solution contributes to the increase in pH value. Zeta potential refers to the potential difference between the shear plane and the bulk solution surrounding the particle

surface. A shear plane separates the mobile fluid from the adsorbed ions, organic molecules and solvent that move with the particle. In the absence of Brij 58, the negative zeta potential values show that the surface charge of the nanoparticles is negative, and the values shift toward 0 with increasing pH. In the presence of Brij 58, the zeta potentials are close to 0.

H^+ and OH^- are the potential determining ions for metal oxides and hydroxides because of the metal hydroxyl group –MOH at the surfaces. When the solution pH varies from the isoelectric point (IEP) of the metal oxide or metal hydroxide, one of the following ionization processes of surface –MOH groups can take place[97]:

$–MOH + H^+ <–> –MOH_2^+$ (pH < IEP, resulting in a positive surface charge)

$–MOH <–> –MO^- + H^+$ (pH > IEP, resulting in a negative surface charge)

NH_4TiOF_3 and TiO_2 both contain surface hydroxyl groups –TiOH and, thus, exhibit variations of zeta potential with solution pH. As the solution pH increases, zeta potential of either pure phase should decrease or reach a plateau. However, the zeta potential measured in the absence of Brij 58 generally increases with solution pH (Table 4.3). The negative zeta potential (-15.4) at pH 3.6 whereby NH_4TiOF_3 is produced, suggests that the IEP of NH_4TiOF_3 is below 3.6. IEP of TiO_2 (anatase) has been reported in literature with a rather broad range of 5-7.[98] Since the measurement was done at 25˚C, the particle status should be most relevant to the products shown in Figure 4.2e-h, i.e. nanoparticles with an end product of TiO_2 (anatase) at 23˚C after 3 days. Although the end products obtained in the absence of Brij 58 at 23˚C, regardless of the amount of ammonia solution, are all TiO_2 (anatase) after 3 days, the conversion rate from NH_4TiOF_3 to TiO_2 is dependent on the solution pH. Therefore,

the fact that zeta potential value increases slightly with pH suggests that the nanoparticles measured for zeta potential in the absence of Brij 58 was a mixture of NH_4TiOF_3 and TiO_2 (anatase) and the portion of TiO_2 increased with the solution pH, i.e., the amount of ammonia solution added.

In contrast to the zeta potential values obtained in the absence of Brij 58, the values obtained in the presence of Brij 58 are all close to 0 regardless of the amount of ammonia solution added (Table 4.3). In addition to the possible explanation in consideration of the high viscosity and turbidity of the solutions containing surfactant Brij 58,[99] we consider the following plausible reasons. Delgado notes that "adsorbed organic matter marks, to some extent, the physiochemical properties of underlying surfaces and dominates surface interactions of mineral particles with the aquatic medium".[100] Indeed, it has been experimentally proved that adsorbed polymer molecules can cause an outward shift of the shear plane and thereby reduce the magnitude of zeta potential.[101, 102] The dramatically reduced magnitude of zeta potential, as compared to the cases without Brij 58, shows that Brij 58 surfactant molecules have successfully adsorbed onto the surfaces of nanoparticles. It has been reported that polymers adsorbed onto silica or alumina via the PEO groups tend to desorb as the solution pH exceeds the IEP.[103, 104] The data here suggests that, even though the increase in solution pH caused by the addition of ammonia solution might have induced desorption of Brij 58 molecules, the effect is not too great that leads to complete desorption. Furthermore, the residue Brij 58 molecules on the surfaces can still facilitate mesoscale assembly of NH_4TiOF_3 nanocrystals (Scheme 4.1).

Table 4.3 Zeta potential of the particles measured at 25˚C. Upon homogeneous mixing of ammonia solution, the solutions were immediately centrifuged at 9000 rpm for 5 min before measurement and only the supernatants were measured (because of the high supersaturation, particles continue to form in the supernatants).

$NH_3 \cdot H_2O$	**Without Brij 58**		**With Brij 58**	
Volume	**pH**	**Zeta potential (mV)**	**pH**	**Zeta potential (mV)**
0 μL	3.6	-15.4 (±1.2)	3.8	+0.7 (±0.4)
80 μL	5.8	-14.8 (±2.2)	5.9	+1.1 (±0.1)
160 μL	7.9	-9.2 (±2.3)	7.5	+1.9 (±0.9)
240 μL	8.8	-8.5 (±2.2)	8.5	+1.1 (±0.4)

For the samples prepared at 4˚C in the presence of Brij 58, the adsorption-desorption isotherms of nitrogen at 77 K are presented in Figure 4.9a and their corresponding pore size distributions are shown in Figure 4.9b. The calculated results of BET specific surface area are tabulated in Table 4.4. The isotherms are of type II which suggests an adsorption mode of monolayer followed by multi-layers. The specific surface area thus calculated increases with the amount of ammonia solution added in the synthesis process. The addition of ammonia solution of 80 μL dramatically increases specific surface area from 3 to 28 m^2/g. The increase in the amount of ammonia solution to 160 μL and 240 μL further increases specific surface area to 36 and 53 m^2/g, respectively. The pore size distribution also varies with the amount of ammonia solution added. Without ammonia solution, the pores are mainly below 4 nm. Upon the addition of ammonia solution, the pore size range expands through mesopore (< 50 nm) to macropore (> 50 nm). With 80 μL and 160 μL of ammonia solution added, the pore size ranges to 100 nm, with dominant

ones below 10 nm. With 240 μL of ammonia solution being added, the dominant pore size is still below 10 nm, but the portion of larger pores has increased. The shift in pore size distribution indicates a shift from intraparticle pores to interparticle pores, corresponding to the size deduction of the particles with the amount of ammonia solution (Figure 4.1a-d). Lastly, the pore volume also increases with the amount of ammonia solution added, i.e., the packing density of individual nanoparticles decreases with the amount of ammonia solution. A plausible reason for this phenomenon could well be the conversion of NH_4TiOF_3 nanocrystals to TiO_2 nanoparticles, a process that limits the supply of NH_4TiOF_3 nanocrystals for the mesoscale assembly of NH_4TiOF_3 mesocrystals.

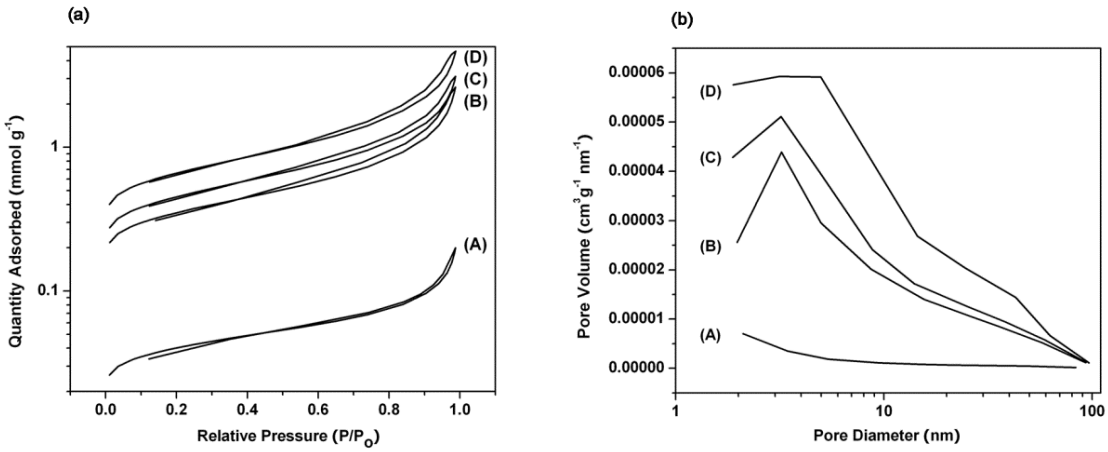

Figure 4.9 BET analyses (nitrogen, 77 K) of the particles grown with Brij 58 at 4˚C.(a) adsorption-desorption isotherms; (b) pore size distribution (calculated from the desorption branch by the Barrett-Joyner-Halenda (BJH) model). Amount of ammonia solution added: (A) 0 μL, (B) 80 μL, (C) 160 μL, (D) 240 μL.

Table 4.4 BET specific surface area of particles synthesized with Brij 58 at 4˚C with varying amount of ammonia solution.

Sample	0 μL	80 μL	160 μL	240 μL
Specific Surface Area (m^2/g)	3	28	36	53

4.5 Morphology Dependence of Photocatalytic Performance

The photocatalytic performance of the calcined products of the particles grown with Brij 58 at 4˚C is evaluated for degradation of aqueous Orange II under UV irradiation (Figure 4.10a). Orange II is an anionic dye[105, 106] that adsorbs onto TiO_2 surface through its oxygen atoms[107]. Heterogeneous photocatalysis is affected by a number of parameters such as the catalyst loading, radiant flux, initial pollutant concentration, aeration, presence of other substances, photoreactor geometry, pH, specific surface area, pore volume, crystallinity and dopant concentration.[108] The first seven factors were kept unchanged in our study, and only specific surface area, pore volume, crystallinity, and dopant type and concentration are considered in the current work. The specific surface area is known to strongly affect the uptaking of dye molecules; pore volume determines the continuous supply of dye molecules for adsorption onto the surface of photocatalyst in the pores; crystallinity influences the amount of recombination centers for the photogenerated electron-hole pairs; dopant type and concentration can alter band structure of the photocatalyst and also contribute to recombination centers.

The performance in photocatalysis is dependent on the amount of ammonia solution added in the synthesis process and calcination temperature (Figure 4.10a). In

the absence of TiO_2, very little degradation of Orange II is observed (5.1%). At the calcination temperature of 500˚C, the resultant anatase particles show an increasing photocatalytic activity with the amount of ammonia solution (i.e., 80 μL < 160 μL < 240 μL), apparently due to the increasing specific surface area (Figure 4.10b) and pore volume (Figure 4.10c) although their crystallinity decreases with the amount of ammonia solution (Figure 4.10d). At the calcination temperature of 700˚C, photocatalytic activity is generally enhanced, as compared to their respective counterparts calcined at 500˚C, but the order has been changed to: 240 μL < 80 μL < 160 μL (Figure 4.10a).

Two factors could contribute to the general enhancement of photocatalytic activity at the higher calcination temperature of 700˚C. One is the improved crystallinity (Figure 4.10d). The other one is the effect of dopant fluorine. The effect of anatase surface fluorination on photocatalytic degradation could be positive or negative depending on its concentration. Under UV irradiation, more free OH radicals are generated on fluorinated anatase because photogenerated electrons can be trapped by ≡Ti-F in association with the strong electronegativity of fluorine.[109] On the one hand, therefore, fluorinated anatase can give rise to a higher degradation rate of OH radical mediated organic molecules (e.g. phenol, Orange II).[109, 110] On the other hand, however, fluoride ions can also act as recombination centers.[110] Thus, the dopant concentration of fluorine should be optimized to better enhance the photocatalytic activity of fluorinated anatase. Defluorination of fluorine stabilized anatase has been realized by two major methods. One is by ligand exchange of fluorinated anatase in

alkaline solutions ($\equiv$Ti-F + OH^- $\rightarrow$ $\equiv$Ti-OH + F^-).[105, 109, 111-114] The other is by calcination in air at high temperatures.[110, 112, 114, 115] Noticeably, Lee et al. studied the continuous decrease in content of fluorine as the annealing temperature for NH_4TiOF_3 is increased from 0˚C to 1000˚C.[116] Our XPS results also show that the amount of fluorine is smaller at the higher calcination temperature of 700˚C (Figure 4.11). Therefore, the reduction in concentration of fluorine can contribute to the enhanced photocatalytic activity at the higher calcination temperature of 700˚C. This consideration is confirmed by the greater enhancement for the samples 80 μL and 160 μL (Figure 4.10a), as compared to their counterparts calcined at 500˚C due to their greater reduction of fluorine amount (Table 4.2).

At the calcination temperature of 700˚C, the photocatalytic activity follows the order: 240 μL < 80 μL < 160 μL. The effects of specific surface area (Figure 4.10b), pore volume (Figure 4.10c) and crystallinity (Figure 4.10d) contribute to their photocatalytic activity according to the following orders: 80 μL < 160 μL < 240 μL, 80 μL < 160 μL < 240 μL, and 80 μL > 160 μL > 240 μL, respectively. Another factor which could also contribute to the photocatalytic activity is the portion of {001} facets. In the work of Lu and coworkers,[115] fluorine is employed to stabilize the energetic {001} facets of anatase , which has aroused considerable research interests in increasing the portion of {001} facets for various morphologies of anatase[112]. The energetic {001} facets are highly active and promising for favorable applications in photocatalytic degradation[111, 117-119], photocatalytic water splitting[117, 120], dye-sensitized solar cells[121-123], and lithium ion batteries[124-126]. Zhou et al.[59] and Feng

et al.[65] have reported that NH_4TiOF_3 mesocrystals can be converted to TiO_2 (anatase) mesocrystals after calcination and their unit cell directions and morphology remain the same. In the present study, since the NH_4TiOF_3 mesocrystals synthesized at 4˚C in the presence of Brij 58 with 80 μL and160 μL of ammonia solution expose a large portion of {001} facets (Figure 4.4a & c), the resultant TiO_2 (anatase) mesocrystals obtained after calcination would expose a large portion of {001} facets. This large portion of {001} facets for the samples 80 μL and160 μL could also contribute to the photocatalytic activity order 240 μL < 80 μL < 160 μL at the calcination temperature of 700˚C.

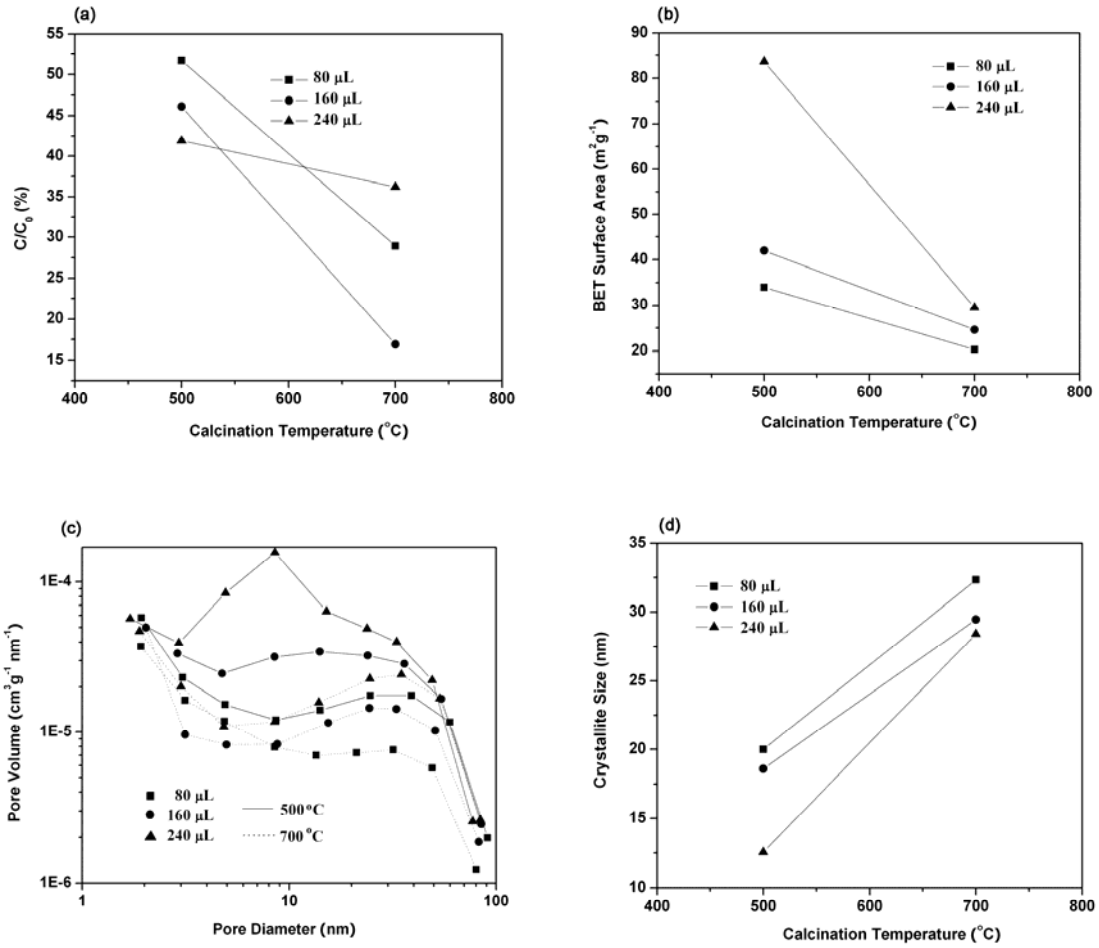

Figure 4.10 Photocatalytic performances, BET results, and crystallite sizes of thermally treated products. (a) Portions of the Orange II left from decomposition under UV irradiation (in the absence of TiO_2, portion left is 94.9%). Photocatalysts were prepared by calcining the solid particles at 500˚C and 700˚C respectively, which were synthesized in the presence of Brij 58 at 4˚C. (b) BET specific surface areas of the resultant TiO_2 (anatase). (c) Pore size distribution of the resultant TiO_2 (anatase). (d) Coherence length calculated by the Scherrer Equation using the peak at 2θ of 25.3 ^{o} corresponding to (101) plane.

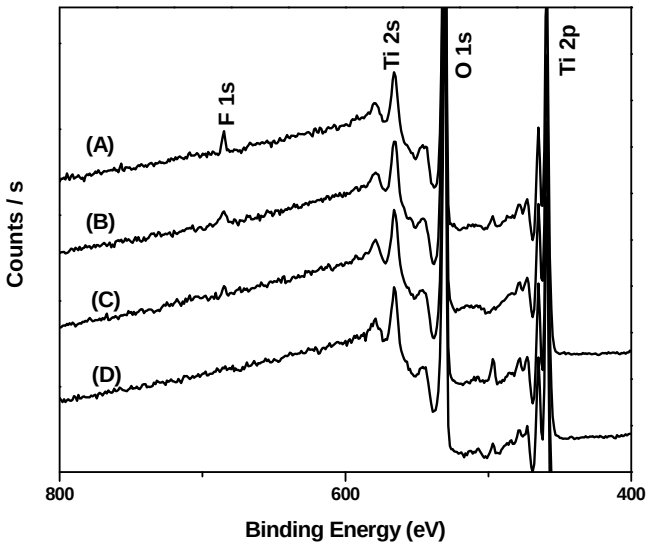

Figure 4.11 XPS survey scans of thermally treated TiO_2 powder. (A) 80 μL, 500˚C; (B) 240 μL, 500˚C; (C) 80 μL, 700˚C; (D) 240 μL, 700˚C.

4.6 Remarks

We have in this chapter investigated three factors that affect the formation of NH_4TiOF_3 mesocrystals (Scheme 4.1, Route 1): temperature, the presence of surfactant Brij 58 and pH of the reaction solution. The route (Scheme 4.1, Route 2) that leads to the formation of TiO_2 (anatase) aggregates competes against the mesoscale assembly of NH_4TiOF_3 nanocrystals into NH_4TiOF_3 mesocrystals. Higher temperature and higher solution pH both favor the conversion from NH_4TiOF_3 nanocrystals to TiO_2 nanoparticles. The presence of Brij 58 however facilitates the mesoscale assembly process. In the presence of Brij 58 and at 4˚C, a higher solution pH, i.e., a larger amount of ammonia solution, increases the conversion rate of NH_4TiOF_3 nanocrystals to TiO_2 nanoparticles and thereby reduces the amount of NH_4TiOF_3 nanocrystals available for the formation of NH_4TiOF_3 mesocrystals. The

resultant NH_4TiOF_3 mesocrystals show an increasing pore volume with solution pH. Photocatalytic performance of the calcined TiO_2 particles is enhanced at the high calcination temperature of 700˚C. The portion of {001} facets and fluorine content of the TiO_2 particles thus derived have contributed to the best photocatalytic performance observed for 160 μL observed in the present work.

CHAPTER 5. FROM NH_4TIOF_3 NANOPARTICLES TO NH_4TIOF_3 MESOCRYSTALS: STERIC HINDRANCE VERSUS HYDROPHOBIC ATTRACTION OF F127 MOLECULES

5.1 Background

Mesocrystals are assembled from small units of building blocks that are crystallographically oriented.[3, 4] These small units of building blocks are usually nanocrystals grown in solutions.[127] Such a colloid system does not require long-term stability so that the small units can undergo the mesoscale assembly process to form mesocrystals. As such, the stability of these small units is crucial in controlling the formation of mesocrystals. There are three general approaches to impose colloidal stability.[128, 129] (i) Polymeric stabilization, which utilizes certain non-ionic organic polymers, presents two routes depending on whether the functioning polymer molecules are attached to the nanoparticle surfaces. For steric stabilization, part of the polymer molecules is attached ("anchored") to the nanoparticle surfaces while the rest is dangling in the solution. Aggregation is retarded due to the steric effect of the dangling polymer chains. For depletion stabilization, the polymer molecules do not interact with the nanoparticle surfaces. A high energy is thus required to create a zone depleted of the free polymers and this energy barrier impedes aggregation. (ii) Electrostatic stabilization is caused by ionization of the nanoparticle surfaces, ion

exchange between the nanoparticle surfaces and the surrounding solution, and ion binding with the ions from the surrounding solution to the nanoparticle surfaces. Such net charges on the nanoparticle surfaces lead to colloidal stability. (iii) Electrosteric stabilization is realized by the attachment of charged organic polymers onto nanoparticle surfaces. Both steric effect and electrostatic effect of these organic polymers are employed in this approach. In this chapter, polymeric stabilization, which is a specifically steric effect of surfactant F127, is utilized to enhance the colloidal stability of NH_4TiOF_3 nanoparticles and thereby impede formation of NH_4TiOF_3 mesocrystals.

In addition to the colloidal stability of NH_4TiOF_3 nanoparticles, their chemical stability is also considered in this chapter. In our previous study, we proposed two routes that took place in the solution: (a) mesoscale assembly of NH_4TiOF_3 nanoparticles into NH_4TiOF_3 mesocrystals; and (b) conversion of NH_4TiOF_3 nanoparticles into TiO_2 nanoparticles and the subsequent formation of TiO_2 aggregates. We have observed that the presence of surfactant Brij 58 (23 wt%), which consists of a hydrophobic alkyl chain (C_{16}) and a hydrophilic PEO group (EO_{20}), facilitates the mesoscale assembly, while increasing the solution pH and elevating the reaction temperature facilitate the chemical conversion process. In the work described in this chapter, we present a new method to obstruct the mesoscale assembly process and hence facilitate the formation of TiO_2 by replacing the hydrophobic alkyl chain (C_{16}) of Brij 58 with a more hydrophilic chain PO_{70} of surfactant F127, which creates certain steric stabilization effect at an appropriate concentration (10 wt%). In addition to the two routes proposed previously (Scheme

5.1, Route 1 and 3), we propose one more route (Scheme 5.1, Route 2) in this chapter whereby at an appropriate intermediate concentration (10 wt%) of surfactant F127, NH_4TiOF_3 nanoparticles are stabilized in the colloid and then chemically converted to sterically stabilized TiO_2 nanoparticles at 23 ˚C and 35 ˚C. To further support what is demonstrated, a careful investigation is made into the temperature effect, which will be discussed in this chapter together with some of the phenomena reported in the previous chapter.

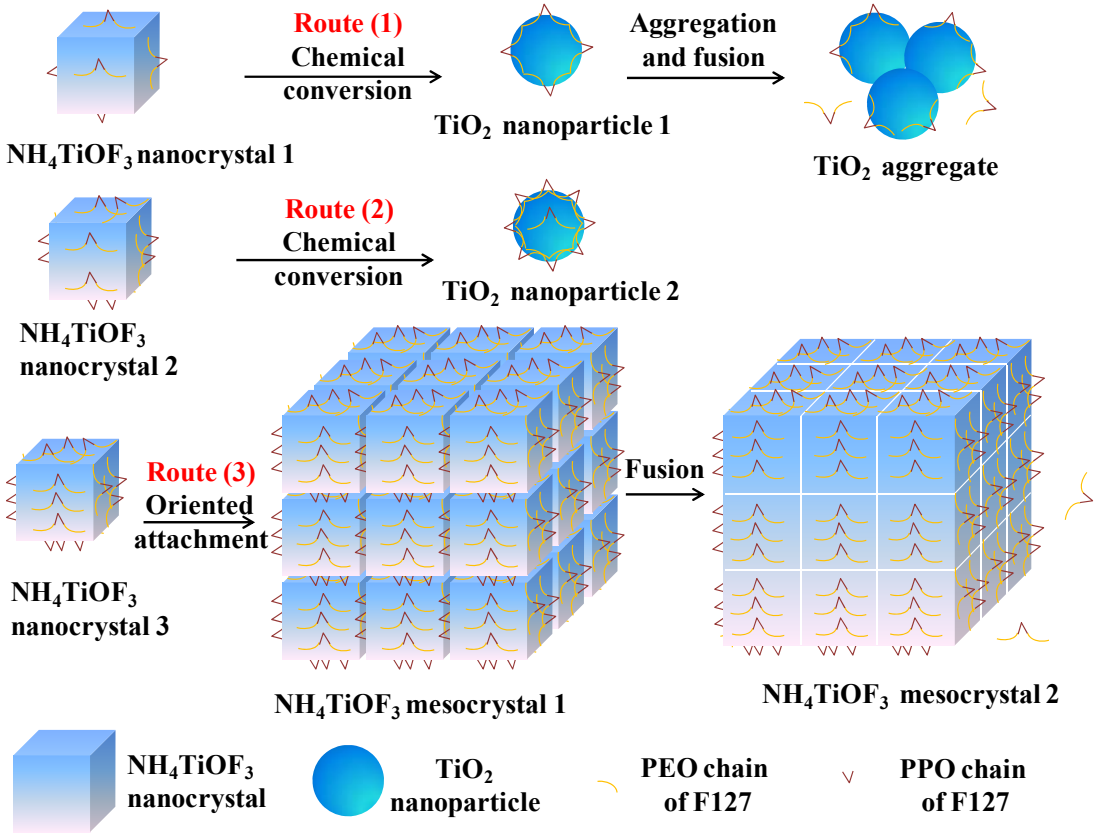

Scheme 5.1 The Three Routes for NH_4TiOF_3 Nanocrystalline Building Blocks Depending on the Surfactant (F127) Concentration in the Solution. Route (1) formation of TiO_2 aggregates; Route (2) formation of TiO_2 nanoparticles; Route (3) formation of NH_4TiOF_3 mesocrystals. The concentration of F127 is increased from Route 1 to Route 3. The size of surfactant F127 molecules has been exaggerated in the drawing and the shape varies in the aqueous solution.

5.2 Experimental Details

Solid particles were grown in an aqueous solution, according to what has been reported,[59] except that the surfactant Brij 58 is replaced by F127 ($EO_{106}PO_{70}EO_{106}$, Sigma) in the present work. Typically, aqueous solutions of surfactant F127 (0 wt%, 2 wt%, 5 wt%, 10 wt%, 15 wt%, and 20 wt%) were first prepared at 23 ˚C. An appropriate amount of fluoride scavenger H_3BO_3 (99.8%, Merck) (weight ratio

H_3BO_3 : H_2O = 123.7 mg : 10 g) was then dissolved in each of the surfactant solutions. Finally, $(NH_4)_2TiF_6$ (99.99%, Aldrich) was added, with a weight ratio $(NH_4)_2TiF_6$: H_2O = 198.0 mg : 10 g. When $(NH_4)_2TiF_6$ was well dissolved, particles were allowed to grow under static condition at 4 ˚C, 23 ˚C, and 35 ˚C for a desired period of time. The resultant solid particles were then recovered by centrifugation and washing successively for three times. The solvents used for washing were water, acetone and ethanol. Drying was carried out at 60 ˚C for 12 h. Calcination of the solid particles was operated at 700 ˚C for 5 h with a ramp rate 2 ˚C/min.

5.3 Characterization of NH_4TiOF_3 Mesocrystals and TiO_2 Particles

The morphology (Figure 5.1) and crystalline phases (Figure 5.3) of the as-synthesized particles are dependent on both temperature and the concentration of F127. Examples of XRD patterns of the single phased NH_4TiOF_3, TiO_2, and a combination of them, including those particles prepared at 0%, 10%, 15%, and 20% of F127 at all three temperatures, are shown in Figure 5.2. A summary of morphology and crystalline phases characterized for all particles prepared under various conditions are tabulated in Table 5.1.

At 4 ˚C, NH_4TiOF_3 is the only crystalline phase identified, while the morphology includes those of heavily aggregated micro-drums, nanoparticles, and discrete micro-drums (Figures 5.1, 2). The micro-drums are heavily aggregated when no surfactant F127 is added (Figure 5.1a). At 2% of F127, nanoparticles dominate (Figure 5.1d). At 5% of F127, both nanoparticles and discrete micro-drums are developed (Figure 5.1g). At 10% and 15% of F127, only discrete micro-drums are

observed (Figure 5.1j, m). At 20% of F127, both nanoparticles and discrete micro-drums are obtained again (Figure 5.1p).

At 23 ˚C, the products include heavily aggregated NH_4TiOF_3 micro-plates, NH_4TiOF_3 aggregates, TiO_2 nanoparticles, discrete NH_4TiOF_3 micro-flakes, and discrete NH_4TiOF_3 micro-plates (Figures 5.1, 2). The micro-plates are heavily aggregated when no surfactant F127 is added (Figure 5.1b). At 2%, 5%, and 10% of F127, nanoparticles and aggregates of both NH_4TiOF_3 and TiO_2 are observed (Figure 5.1e, h, k). At 15% of F127, both nanoparticles and discrete NH_4TiOF_3 micro-flakes are obtained (Figure 5.1n). At 20% of F127, both nanoparticles and discrete NH_4TiOF_3 micro-plates appear (Figure 5.1q).

NH_4TiOF_3 mesocrystals were observed, unexpectedly, at both 4 ˚C and 23 ˚C in the absence of F127. In Chapter 6, it will be confirmed that NH_4TiOF_3 is a ferroelectric material, where the spontaneous dipolar interactions can well lead to the mesoscale assembly of NH_4TiOF_3 nanocrystals. Detailed report for the ferroelectric behavior of NH_4TiOF_3 will be discussed in Chapter 6.

At 35 ˚C, the products include heavily aggregated TiO_2 micro-plates, TiO_2 nanoparticles, TiO_2 aggregates, and discrete NH_4TiOF_3 micro-plates (Figures 5.1, 2). The TiO_2 micro-plates are heavily aggregated when no F127 is added (Figure 5.1c). At 2% and 5% of F127, both TiO_2 nanoparticles and aggregates are observed (Figure 5.1f, i). At 10% of F127, only TiO_2 nanoparticles are observed (Figure 5.1l). The particle size generally decreases as the concentration of F127 is increased from 2% to 10%, while the aggregation of TiO_2 nanoparticles becomes progressively less obvious. At 15% and 20% of F127, both TiO_2 nanoparticles and discrete NH_4TiOF_3

micro-plates are observed (Figure 5.1o, r).

The effect of surfactant Brij 58 ($C_{16}EO_{20}$) concentration at 35 ˚C has been studied by Zhou et al.[59] Large TiO_2 particles (micron sizes) were observed at a very low concentration of Brij 58 (1%). The morphology approached square shape and the amount of aggregated NH_4TiOF_3 mesocrystals increased as the concentration of Brij 58 was increased. Moreover, discrete NH_4TiOF_3 mesocrystals were developed when the concentration was increased to 23%. In comparison to Brij 58 ($C_{16}EO_{20}$) which contains a rather hydrophobic alkyl group (C_{16}), each F127 ($EO_{106}PO_{70}EO_{106}$) molecule contains a less hydrophobic PO_{70} chain which "develops a hydration shell with an enhanced structure of water" [130]. Consequently, in the present work, an adequate amount of F127 is able to sterically impede the mesoscale assembly of NH_4TiOF_3 nanoparticles as well as the aggregation of their chemically converted products TiO_2 nanoparticles at 35˚C. Specifically, at the same temperature (35˚C), the presence of 10% of F127 gives rise to a colloid of NH_4TiOF_3 nanoparticles that is relatively stable and resistant to aggregation or mesoscale assembly due to the steric stabilization effect of the PPO chain (Scheme 5.1, Route 2). At 2% and 5% of F127, due to the insufficient F127 molecules, the steric effect of the PPO chains is less prominent and some aggregates are also observed (Scheme 5.1, Route 1). Furthermore, at higher concentrations of F127 (15% and 20%), NH_4TiOF_3 nanoparticles tend to undergo a mesoscale assembly process to form NH_4TiOF_3 mesocrystals (Scheme 5.1, Route 3). The effect of higher concentration of F127 can be explained by the following plausible reason. At higher concentrations, the hydrophobicity of PPO chains is prominent and the hydrophobic force draws the

NH_4TiOF_3 nanoparticles towards each other and thereby the requirement of spatial contact for mesoscale assembly is met. The postulation that PPO chains tend to interact with each other instead of water molecules at higher concentrations is analogous to the micellization process of surfactant F127 in water.[131-133] Furthermore, when the concentration of F127 is too high, an observable gelation of the reaction solution takes place and consequently the transportation of the NH_4TiOF_3 particles is slowed down such that both submicron particles and mesocrystals are formed. This phenomenon is most obvious for the samples obtained in the presence of 20% F127. Gelation of F127 in water has been reported in literature.[133, 134]

Temperature has apparent effects on both crystalline phases and morphology of the products. Figure 5.3 shows that NH_4TiOF_3 tends to form at low temperature and the tendency of forming TiO_2 strengthens as temperature increases. We have previously proposed that raising temperature kinetically enhances the chemical conversion process from NH_4TiOF_3 nanoparticles to TiO_2 nanoparticles. In the present work, the higher reaction rate and yield at 35 ˚C, in comparison to 23 ˚C, also result in formation of TiO_2, though the steric hindrance by the PPO chain of F127 at 2% is not prominent because the limited amount of surfactant F127 cannot provide adequate coverage on the particle surfaces (Figure 5.1).

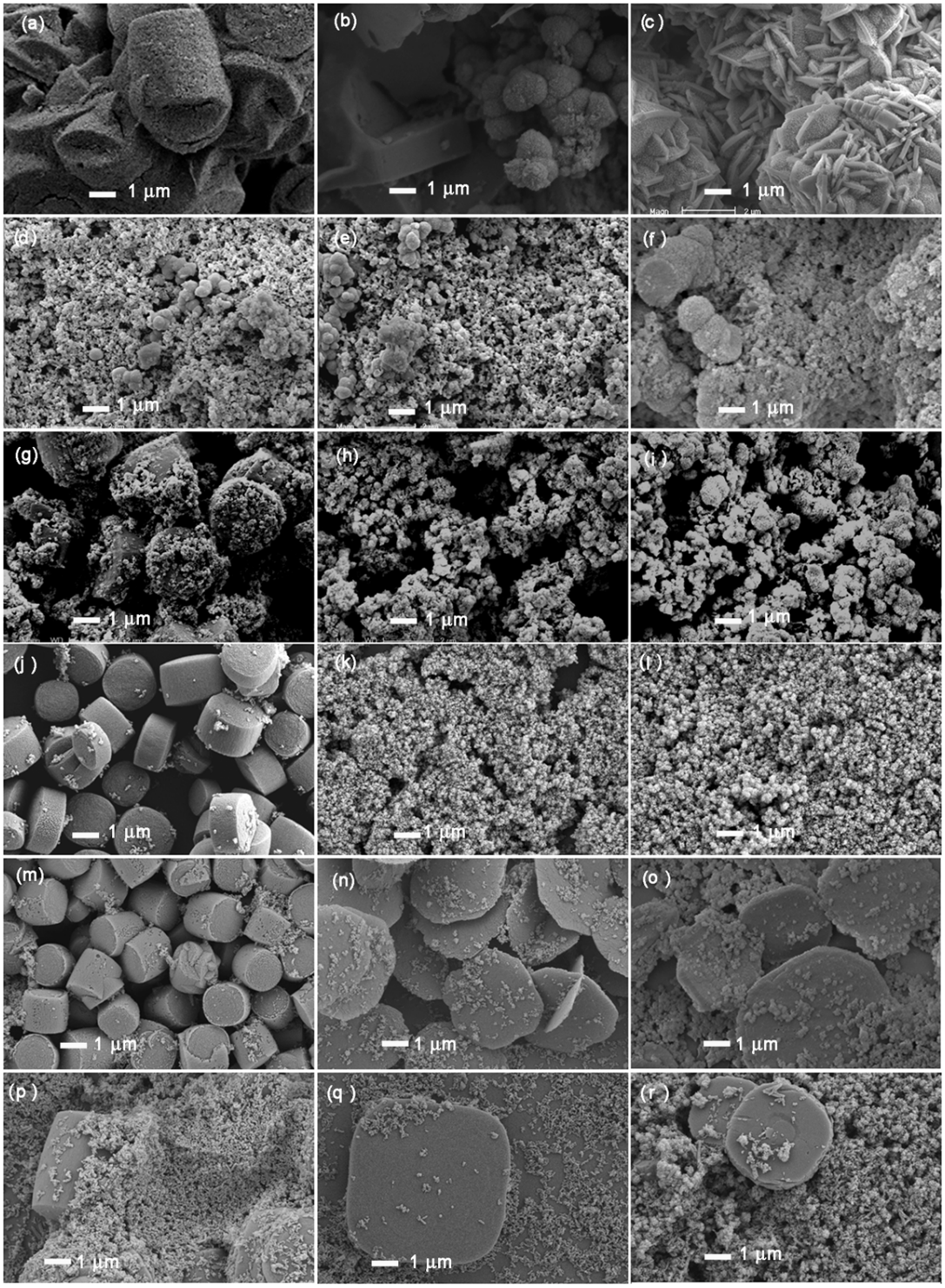

Figure 5.1 SEM images of the as-synthesized particles prepared at various temperatures and concentrations of surfactant F127 after a growth time of 3 days. Column from left to right: 4 ˚C, 23 ˚C, and 35 ˚C. Row from top to bottom: 0%, 2%, 5%, 10%, 15%, and 20%.

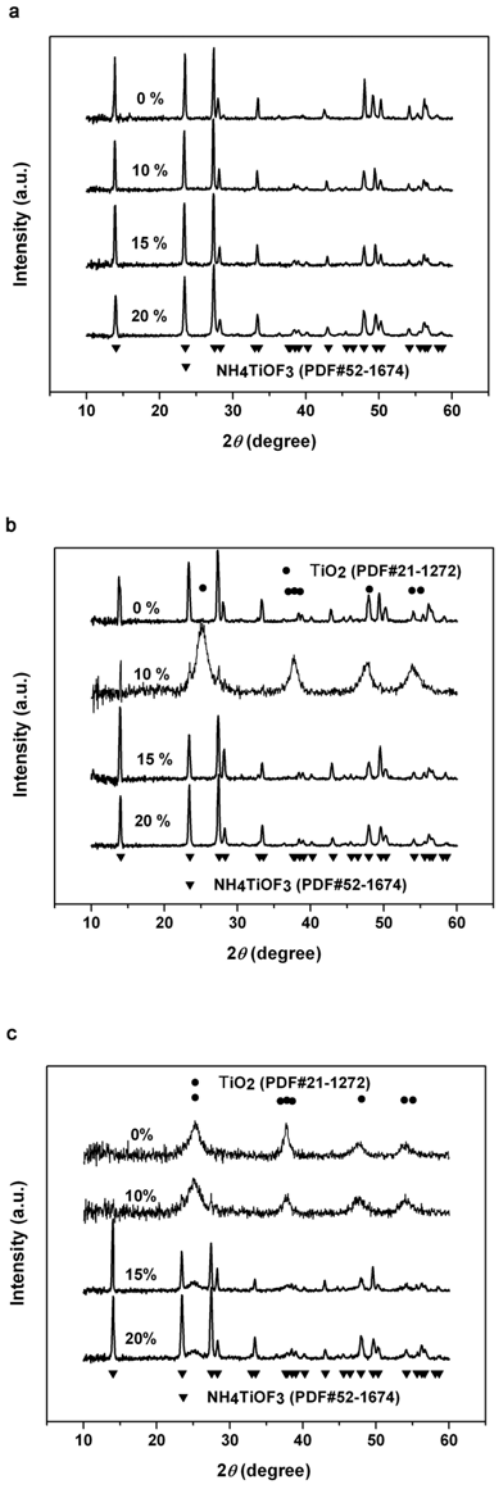

Figure 5.2 XRD of as-synthesized particles prepared at various temperature and concentrations of surfactant F127. (a) 4 ˚C; (b) 23 ˚C; (c) 35 ˚C.

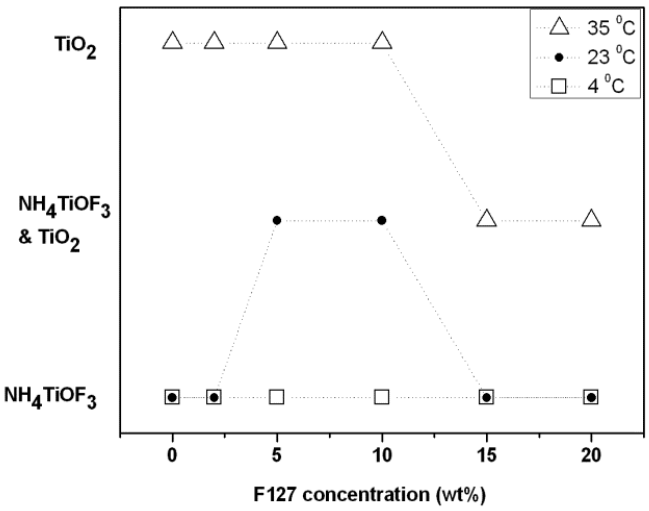

Figure 5.3 Phase identification results by XRD for the particles prepared at 4 ˚C, 23 ˚C, and 35 ˚C respectively with various concentrations of F127. Crystalline phases vary with the concentration of F127 and reaction temperature.

Table 5.1 Summary of the particles synthesized at various conditions based on SEM and XRD results

Reaction Condition	**Crystalline Phase(s)**	**Morphology**
F127 0%, 4 ˚C	NH_4TiOF_3	aggregated mesocrystal
F127 2% , 4 ˚C	NH_4TiOF_3	nanoparticle
F127 5% , 4 ˚C	NH_4TiOF_3	mesocrystal & nanoparticle
F127 10% , 4 ˚C	NH_4TiOF_3	mesocrystal
F127 15% , 4 ˚C	NH_4TiOF_3	mesocrystal
F127 20% , 4 ˚C	NH_4TiOF_3	mesocrystal & nanoparticle
F127 0%, 23 ˚C	NH_4TiOF_3	aggregated mesocrystal
F127 2% , 23 ˚C	NH_4TiOF_3 & TiO_2	nanoparticle & aggregate
F127 5% , 23 ˚C	NH_4TiOF_3 & TiO_2	nanoparticle & aggregate
F127 10% , 23 ˚C	NH_4TiOF_3 & TiO_2	nanoparticle
F127 15% , 23 ˚C	NH_4TiOF_3	mesocrystal & nanoparticle
F127 20% , 23 ˚C	NH_4TiOF_3	mesocrystal & nanoparticle
F127 0%, 35 ˚C	TiO_2	aggregate
F127 2% , 35 ˚C	TiO_2	nanoparticle & aggregate
F127 5% , 35 ˚C	TiO_2	nanoparticle & aggregate
F127 10% , 35 ˚C	TiO_2	nanoparticle
F127 15% , 35 ˚C	NH_4TiOF_3 & TiO_2	mesocrystal & nanoparticle
F127 20% , 35 ˚C	NH_4TiOF_3 & TiO_2	mesocrystal & nanoparticle

Macroscopically, the crystalline phases detected by XRD in the samples prepared at 23 ˚C are NH_4TiOF_3 for 0%, 15%, and 20% of F127, and mainly TiO_2 for 10% of F127 (Figure 5.2). FTIR spectra of the samples prepared at 23 ˚C with 0%, 10%, 15%, and 20% of F127 reveal the same observations (Figure 5.4). The IR-absorption bands

at 3290, 3199 and 3087 cm^{-1} for the samples prepared at 15% and 20% are ascribed to the stretching modes of NH_4^+.[66, 70, 90, 91] The band at 3153 cm^{-1} for the sample prepared at 10% of F127 is of much lower intensity, which is also ascribed to the stretching mode of NH_4^+.[90] The latter band is no longer well resolved into the former three bands because of the dramatically reduced amount of nitrogen (Table 5.2). The bands at 1417 and 2858 cm^{-1} are ascribed to the bending mode of NH_4^+ and its overtone band, respectively.[66, 70, 90, 91] Again, these two bands for the sample prepared at 10% of F127 is very low in intensity indicating a very small amount of NH_4^+ in this sample. The band at 884 cm^{-1} is attributed to the stretching mode of Ti=O (terminal oxygen) [66, 70] or Ti-O-Ti antisymmetric stretching[92]. Another band at 758 cm^{-1} corresponds to a combination of lattice modes of Ti-O and Ti-F.[70] The band at 628 cm^{-1}, which is attributed to Ti-F [66, 70], disappears in the sample prepared at 10% of F127. This is consistent with the experimental results of elemental analysis that the amount of fluorine in that sample is rather low (Table 5.2). The bands at 551, 504, and 461 cm^{-1} are due to Ti-O.[93, 94] The relative intensity at around 551 cm^{-1} with respect to that at 3153 cm^{-1} is greatly enhanced in the sample prepared at 10% of F127 as compared to those prepared at 15% and 20%. This observation strongly supports our previous speculation that this sample contains less nitrogen and more oxygen. Furthermore, the band at 3432 cm^{-1} is ascribed to O-H stretching of adsorbed water and the hydroxyl groups [90, 95], and that at 1646 cm^{-1} is attributed to H-O-H bending[90] or deformation of the adsorbed water and the hydroxyl groups [66, 95]. These two bands are much stronger for the sample prepared at 10% of F127 in comparison to the other two. This observation is consistent with the hygroscopic nature of TiO_2.[96]

The band at 1050 cm^{-1} in all the samples is due to the C-O-C ether stretching mode of occluded F127.[135, 136]

TGA results (Figure 5.5) of the samples prepared at 23 ˚C with 0%, 10%, 15%, and 20% of F127 also support those observations from XRD and FTIR. From 0 ˚C to 200 ˚C, the sample prepared without F127 (0%) shows no obvious weight loss, while the samples prepared with 15% and 20% of F127 show about 5% of weight loss, and the other sample prepared with 10% of F127 shows about 15% of weight loss. The weight loss during this stage is attributed to the adsorbed water, and the observed difference arises from the fact that these samples contain different amount of the hygroscopic TiO_2. From 200 ˚C to 500 ˚C, the weight loss, which is attributable to NH_4 and F, follows the order of 0% > 15% & 20% > 10%. This implies that the portion of NH_4TiOF_3 follows the same order, that is, 0% > 15% & 20% > 10%. Furthermore, it can also be inferred that, the steric stabilization effect of F127 hinders the mesoscale assembly of NH_4TiOF_3 nanoparticles and consequently allows sufficient time for these NH_4TiOF_3 nanoparticles to chemically convert to TiO_2 nanoparticles, and this effect is the most significant at 10%. Elemental analyses of these samples indeed show that nitrogen, hydrogen, and fluorine have been largely reduced in the sample prepared with 10% of F127 (Table 5.2).

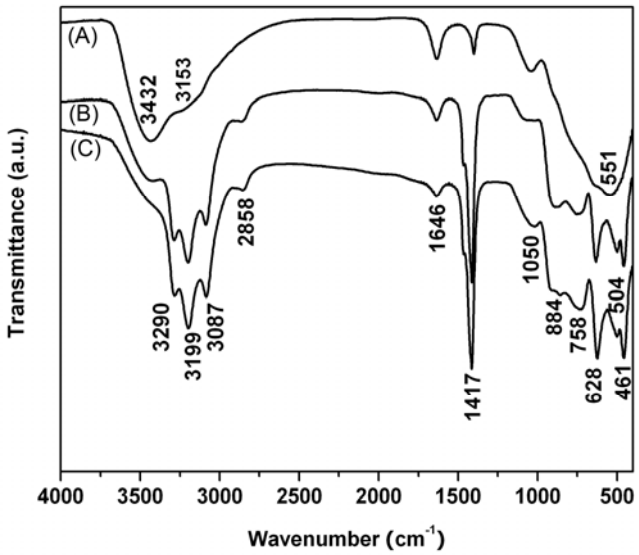

Figure 5.4 FTIR of the as-synthesized particles prepared at 23 ˚C and various concentrations of surfactant F127. (A) 10%; (B) 15%; (C) 20%. The result for 0% is the same as those of 15% and 20%.

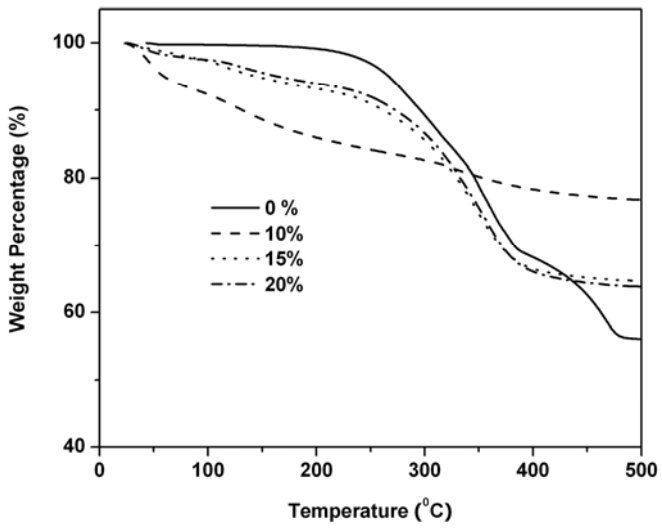

Figure 5.5 TGA of the as-synthesized particles prepared at 23 ˚C and various concentrations of surfactant F127.

Table 5.2 Elemental analyses of the as-synthesized particles prepared at 23 ˚C with various F127 concentrations.

Preparation Condition	H wt%	N wt%	F wt%	Ti wt%
F127 10%	1.55	0.38	6.52	44.61
F127 15%	2.46	7.56	28.38	32.93
F127 20%	2.70	7.86	28.16	29.50

Based on the macroscopic observations (XRD, FTIR, TGA, and elemental analyses) discussed above, it is concluded that the dominant phases in the samples prepared at 23 ˚C are NH_4TiOF_3 for 15% and 20% of F127, and TiO_2 for 10% of F127. In addition, TEM was employed to examine the particle morphologies and phases (Figure 5.6). The micro-particles prepared at 15% and 20% (Figure 5.1n, q, respectively) are NH_4TiOF_3 mesocrystals consisting of crystallographically aligned NH_4TiOF_3 nanoparticles as revealed by the typical example shown in Figure 5.6e-g. Specifically, the single diffraction patterns ([001] zone) of different spots on the same micro-particle show the same crystallographic directions. The nanoparticles derived from 10% and 15% of F127 (Figure 5.6a, c, respectively) are crystallized TiO_2 as suggested by their respective diffraction patterns in Figure 5.6b and d. The nanoparticles observed for 20% are largely amorphous TiO_2 (Figure 5.6h, FFT was taken on atomic scale). In addition, the nanoparticles prepared at 4 ˚C with 2% of F127 are NH_4TiOF_3 (Figures 5. 1, 2). Furthermore, the sample prepared at 35 ˚C with 10% of F127 consists of only TiO_2 nanoparticles (Figures 5. 1, 2). Therefore, it can be concluded that NH_4TiOF_3 nanoparticles in the mother liquor are chemically stable at 4 ˚C and chemically unstable at 23 ˚C and 35 ˚C, over the observation period of 3

days. This phenomenon is reasoned as the chemical reaction rate being higher at elevated temperature according to the Arrhenius relationship. There is a stronger tendency to form TiO_2 with the increase in temperature regardless of surfactant concentration (Figure 5.3). One more point to note is that, once these NH_4TiOF_3 nanoparticles undergo the mesoscale assembly process to form microscale NH_4TiOF_3 mesocrystals, the aforementioned chemical conversion process in the mother liquor is largely slowed down (Figure 5.6c, f).

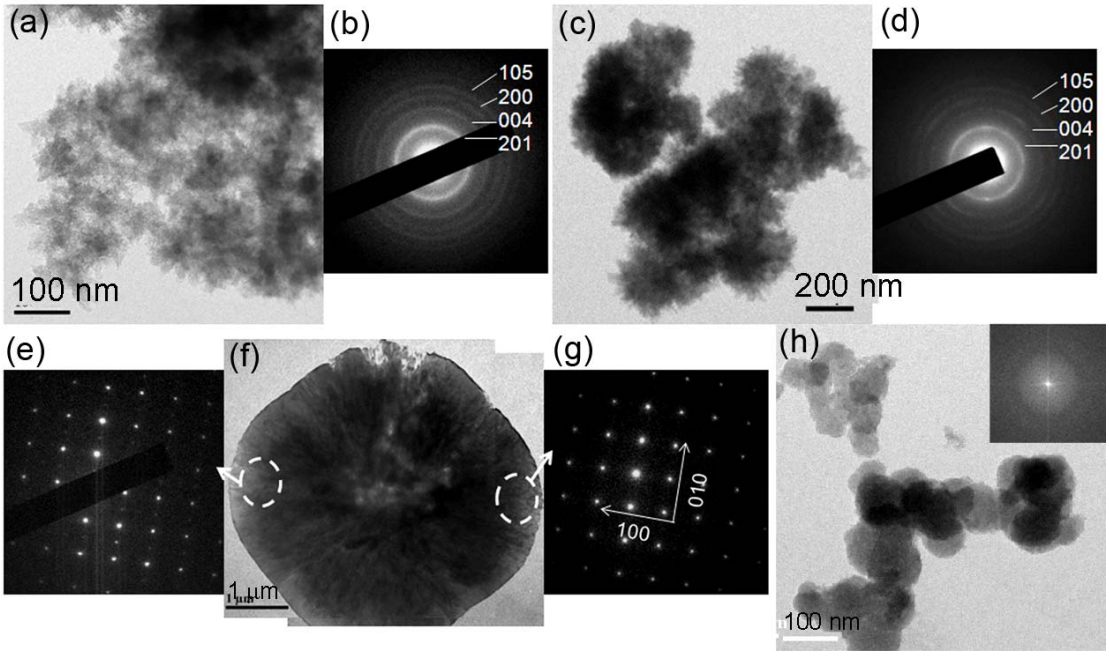

Figure 5.6 TEM images, selected area diffraction (SAED) patterns, and fast fourier transform (FFT) analysis of the as-synthesized particles prepared at 23 ˚C and various surfactant F127 concentrations. (a-b) 10 %; (c-g) 15 %; (h) 20 %, FFT was taken on atomic scale.

5.4 Evolution from NH_4TiOF_3 to TiO_2

In Chapter 4, we have demonstrated that the microscale mesocrystals can be

partially converted to TiO_2 in the mother liquor and completely converted to TiO_2 in deionized water when an enough reaction time is given. In the current study, only TiO_2 nanoparticles are observed for the samples prepared at both 23 ˚C and 35 ˚C with 10% of F127 at the reaction time of 3 days. From the point view of colloidal stability, at 10% of F127, the NH_4TiOF_3 nanoparticles are more stable as compared to the situation at 15% and 20% of F127. Since these isolated NH_4TiOF_3 nanoparticles are not assembled into the microscale mesocrystals that would consist of them, they are very vulnerable to the chemical conversion by water and result in the formation of TiO_2 nanoparticles (Figure 5.3). To confirm the chemical conversion process from NH_4TiOF_3 nanoparticles to TiO_2 nanoparticles, we studied the samples prepared at 35 ˚C (a higher temperature to reduce the experimental period required) with 10% and 15% of F127 by XRD (Figure 5.7) and TEM (Figure 5.8).

Figure 5.7 and Figure 5.8 show XRD spectra, TEM images and SAED patterns for the samples prepared at 35 ˚C with 10% and 15% of F127 for different reaction periods: 4 h, 11 h, and 15 days, respectively. At 4 h, both concentrations of F127 give rise to NH_4TiOF_3 nanoparticles (Figure 5.8a, 7b) and their crystallite sizes are both about 45 nm according to the calculation using the Scherrer's equation (Figure 5.7b). At 11 h, a substantial amount of the NH_4TiOF_3 nanoparticles has been converted to TiO_2 nanoparticles for 10% of F127, while those for 15% remain intact, and the crystallite sizes of NH_4TiOF_3 in both samples do not show obvious change (Figure 5.7a, b). However, after 15 days, the main product derived from 10% of F127 has become TiO_2 nanoparticles (Figure 5.8c), while the product for 15% F127, which also contains some TiO_2 particles (Figure 5.8d), mainly consists of NH_4TiOF_3

mesocrystals (Figure 5.1o) with a crystallite size of about 81 nm (Figure 5.7b). The increase in crystallite size from 45 nm to 81 nm is consistent with the proposed fusion process between neighboring nanoparticles in mesocrystals.[59] Therefore, it is clear that the isolated NH_4TiOF_3 nanoparticles are much more vulnerable to the chemical conversion process from NH_4TiOF_3 to TiO_2 than the microscale NH_4TiOF_3 mesocrystals.

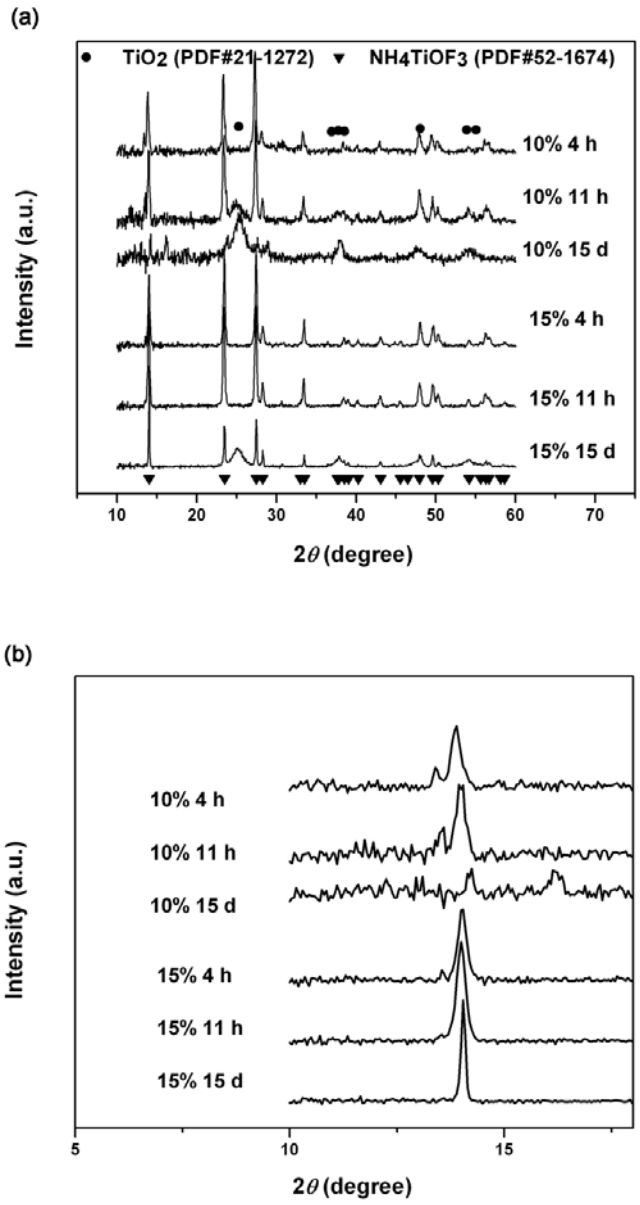

Figure 5.7 XRD traces of the particles prepared at 35 ˚C for 4 h, 11 h, and 15 days with 10% and 15% of F127.

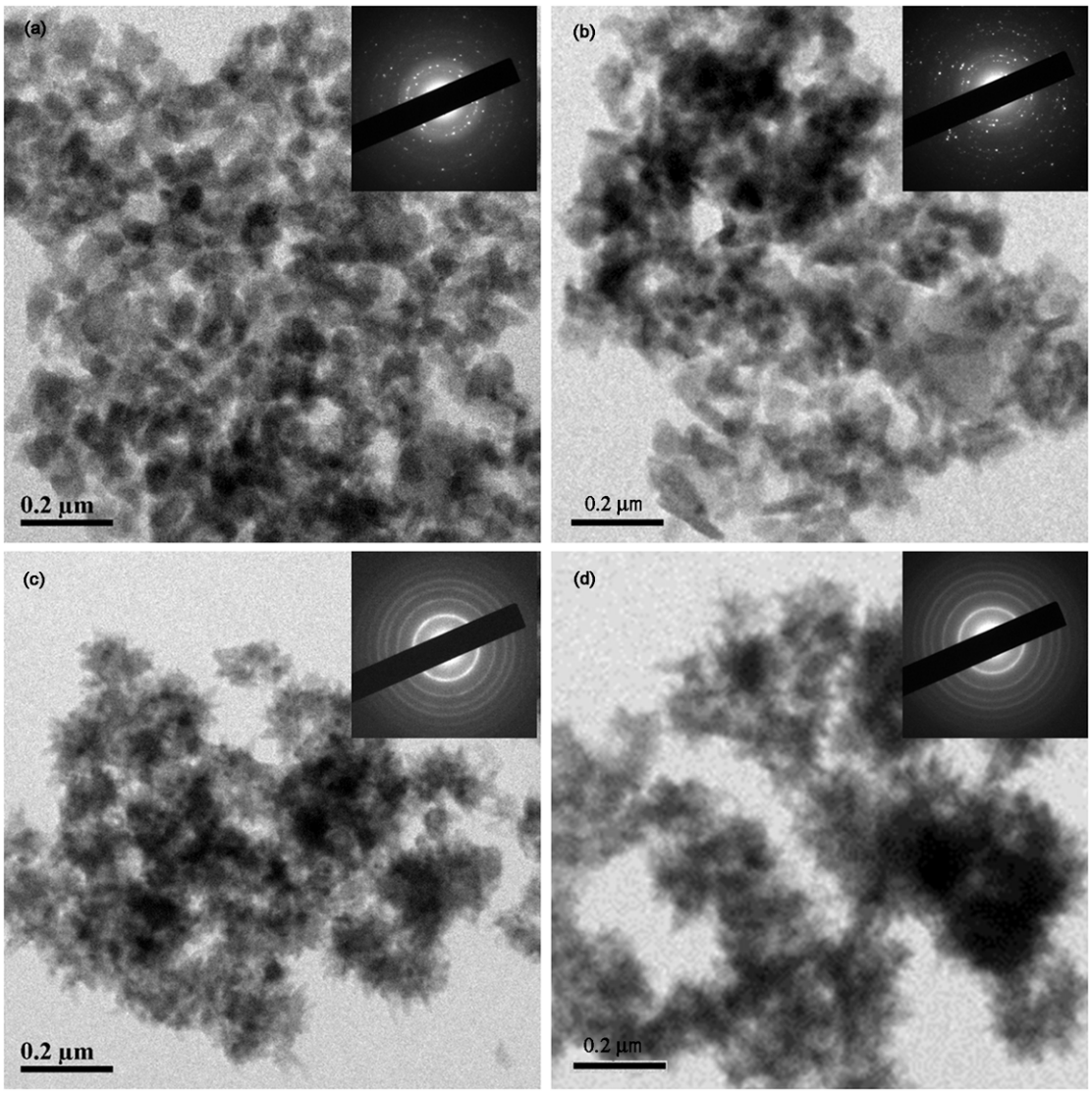

Figure 5.8 TEM and selected area diffraction patterns for the nanoparticles prepared at 35 ˚C for different reaction periods and with different concentrations of F127. (a) 10%, 4 h; (b) 15%, 4 h; (c) 10%, 15 days; (d) 15%, 15 days.

5.5 Surface Adsorption Mode and Effect of F127

As mentioned above, the steric effect of F127 molecules would hinder the mesoscale assembly of NH_4TiOF_3 nanoparticles. Concerning the adsorption of PEO-PPO-PEO triblock copolymers in an aqueous solution, the conformation of

these molecules is dependent on characteristics of the sorbent surfaces. For hydrophobic surfaces, it is generally accepted that the more hydrophobic PPO chains adsorb onto the surfaces while the hydrophilic PEO chains dangle in solution, resulting in a brush-like conformation.[137] For their adsorption on hydrophilic surfaces, an increase in solution pH value induces their desorption from the attached surfaces due to the loss of hydrogen bond[138] between sorbent surface and oxygen groups of the polymers.[139, 140] However, their conformation on hydrophilic surfaces is rather controversial. For example, Killmann et al. [29] have observed that the adsorption of PEO-PPO-PEO triblock copolymers resembles that of PEO homopolymers and thereby suggest that the adsorption operates through both PPO and PEO chains.[139] Malmsten et al. studied the adsorption of PPO homopolymers, PEO homopolymers, and PEO-PPO-PEO triblock copolymers on hydrophilic silica.[30] They have reported that the adsorption (by mass) of PPO homopolymers is "not detectable", while the adsorption of PEO homopolymers is "detectable", and that of PEO-PPO-PEO triblock copolymers is even higher. They concluded that PEO has a stronger tendency to adsorb on silica surfaces, and thereby propose that, for the adsorption of PEO-PPO-PEO triblock copolymers on hydrophilic silica, PEO chains are "preferentially adsorbed" and "located in the proximity of surfaces" and also preferentially reside on the "outer part of the adsorbed layer" while PPO chains lie "in the middle part of the adsorbed layer". Schroen et al. noted the steric effect of pre-adsorbed PEO-PPO-PEO triblock copolymers in reducing the adsorption of proteins.[31] They proposed that the two terminal PEO blocks attaching to hydrophilic surfaces resulted in a pancake conformation. Nejadnik et al. have furthered the study

on the adsorption of F127 on surfaces with different hydrophobicities and concluded that the conformation is pancake on very hydrophilic surfaces and brush on very hydrophobic surfaces.[141]

In the present work, we also prepared samples with 10% of PEG 2000 homopolymers and PEG 20000 homopolymers at 23 ˚C for 3 days (Figure 5.10). The two samples both consist of only aggregated NH_4TiOF_3 mesocrystals. On account of the TiO_2 nanoparticles obtained with 10% of F127 at the same temperature and growth period (Figure 5.1k), it can be perceived that the PO_{70} block is playing a crucial role in controlling the morphology of the final product. A PO group is less hydrophobic than a CH_2 group (about one fourth) [133] and less hydrophilic than a EO group due to the CH_3 group [140]. Therefore, at a relatively low concentration (<=10%), the tendency for the PPO chains to impart hydrophobic force on the NH_4TiOF_3 nanoparticles is small, instead, steric effect predominates. At higher concentrations (>10%), the hydrophobicity of PPO chains becomes important and induces the mesoscale assembly leading to formation of NH_4TiOF_3 mesocrystals as what has been reported for Brij 58.[59] Consequently, in our scheme (Scheme 5.1), we adopt a "pancake" conformation, where the PEO chains are attached to the hydrophilic surfaces and the PPO chains can extend a little bit into the adjacent solution. We also dispersed equal amounts of NH_4TiOF_3 mesocrystals (synthesized at 4 ˚C with 23 % of Brij 58 for 3 days) into 3 solutions (10% of F127, PEG 2000, and PEG 20000) to study the crystalline phase change after 5 days (Figure 5.9). Very little phase change was observed for F127, and a combination of NH_4TiOF_3 and TiO_2 phases was observed for both PEG 2000 (data is not shown) and PEG 20000. This suggests that

the more hydrophobic PPO chains on the outer layer are more effective in reducing the amount of water attacking the NH_4TiOF_3 mesocrystals, in comparison to PEO chains.

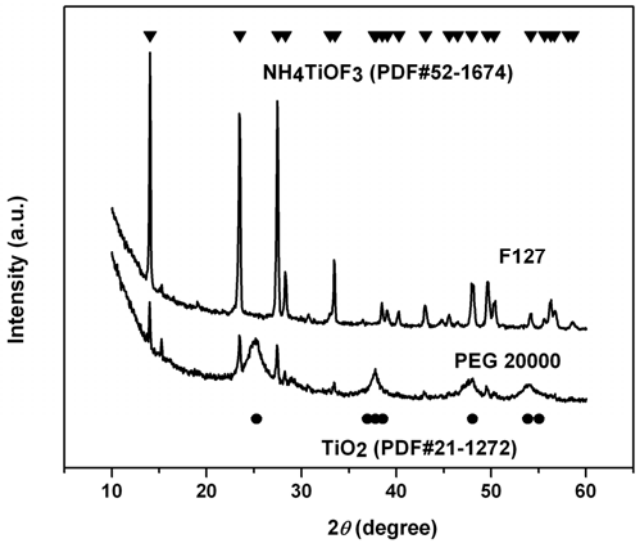

Figure 5.9 XRD traces of the NH_4TiOF_3 mesocrystals dispersed in solutions of F127 (10%) and PEG 20000 (10%). Amount of NH_4TiOF_3 mesocrystals (synthesized at 4 ˚C with 23 % of Brij 58 for 3 days): 36.5 mg; amount of dispersant: 10 g. Ultrasonication till complete dispersion was applied before 5 days of static reaction.

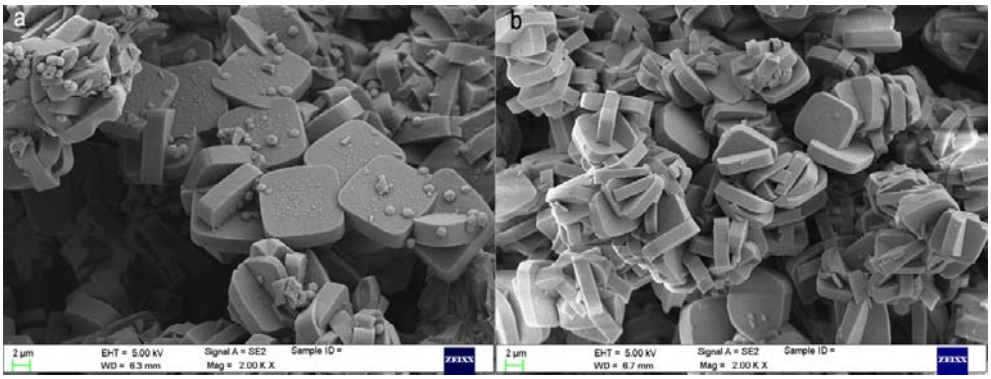

Figure 5.10 SEM images of the as-synthesized aggregated NH_4TiOF_3 mesocrystals grown at 23 ˚C for 3 days with (a) 10% of PEG 2000 and (b) 10% of PEG 20000.

5.6 Photocatalytic Application Related Characterizations

To illustrate the effects of particle morphology (nanoparticle and mesocrystal) on the specific surface area, the results of BET analysis are shown in Figure 5.11, where they are consistent with what have been observed using SEM and TEM. The specific surface areas measured for the samples prepared at 23 ˚C with 10% and 15% of F127 are 112 and 22 m^2/g, respectively. A high surface area to volume ratio of the nanoparticles prepared with 10% of F127 gives rise to a high specific surface area (112 m^2/g). Expectantly, when the nanoparticles are assembled into NH_4TiOF_3 mesocrystals, the specific surface area is dramatically reduced to 22 m^2/g for 15% of F127. Both samples show a rather broad pore size distribution: micro, meso, and macro pore sizes in relation to intra-particle and inter-particle pores. However, the sample prepared with 10% of F127 exhibits, as compared to that prepared with 15% of F127, a dramatically much larger pore volume at each pore size, in consistence with their dominant morphologies of nanoparticles and mesocrystals, respectively.

Upon calcination at 700 ˚C for 5 h, the particles prepared at 23 ˚C with 10% and15% of F127 have been converted to TiO_2 (anatase) as shown in Figure 5.12. The poorly crystallized TiO_2 in the precursor prepared at 10% of F127 have been thermally converted to well crystallized TiO_2 via an Ostwald ripening process (Figure 5.12a-c). In addition to such well crystallized TiO_2 nanocrystals, TiO_2 mesocrystals are also observed for the sample derived from the sample prepared with 15% of F127 (Figure 5.12e and Figure 5.13). The SAED patterns at different spots of the same particle show the same crystallographic directions and interplanar spacings demonstrating the mesocrystal character of these microscale particles (Figure 5.12f,

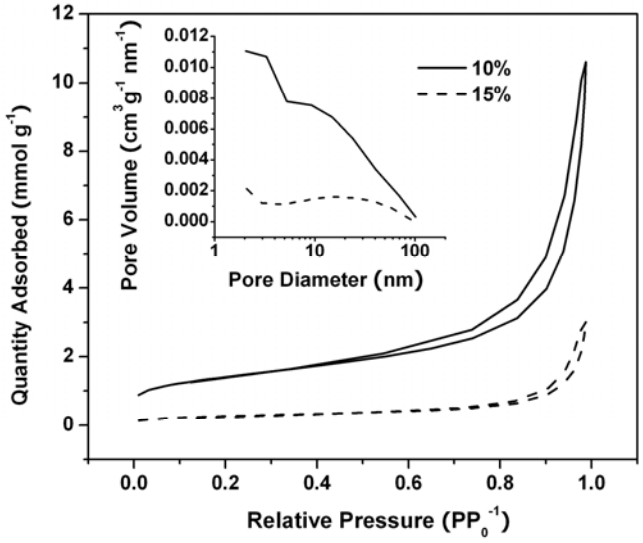

Figure 5.11 BET isotherms and pore size distribution (calculated from the desorption branch by Barrett−Joyner−Halenda (BJH) model) for the nanoparticles and mesocrystals prepared at 23 ˚C with 10% and 15% of F127, respectively. Specific surface areas for the samples prepared with 10% and15% of F127 are 112 and 22 m^2/g, respectively.

g). It has been reported that NH_4TiOF_3 mesocrystals can undergo a topotactic reaction to form TiO_2 mesocrystals as the atomic arrangements of titanium remain the same while the unit cell dimensions are largely reduced. Consequently, the resultant TiO_2 mesocrystals are obviously porous as shown by the TEM images (Figure 5.12d-e), SEM images (Figure 5.13), and BET pore size distribution of their calcined products (Figure 5.14c).

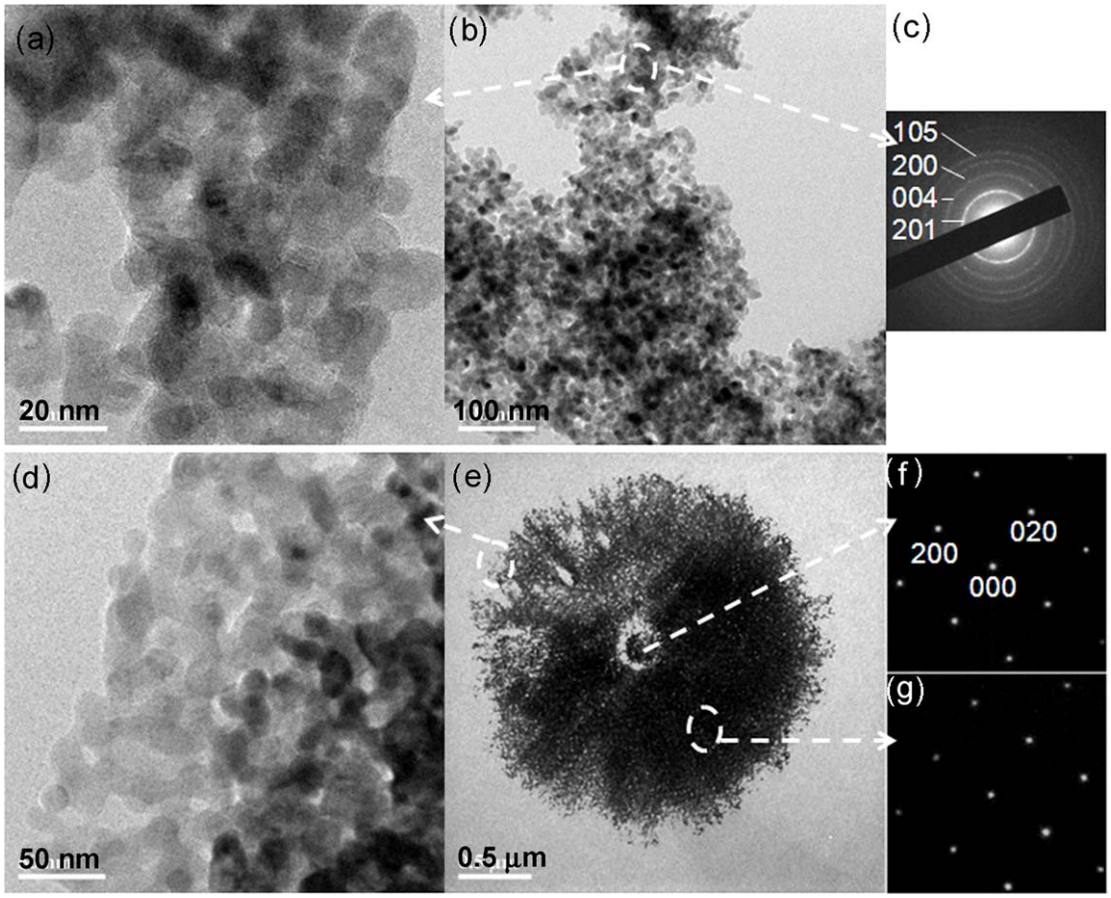

Figure 5.12 TEM images and SAED patterns for the samples synthesized at 23 ˚C with (a-c) 10%, and (d-g) 15% of F127 and subsequently calcined at 700 ˚C for 5 h at a heating rate of 2 ˚C/min. Only TiO_2 nanocrystals are observed for 10% of F127, and TiO_2 mesocrystals are also observed for 15% of F127 in addition to TiO_2 nanocrystals.

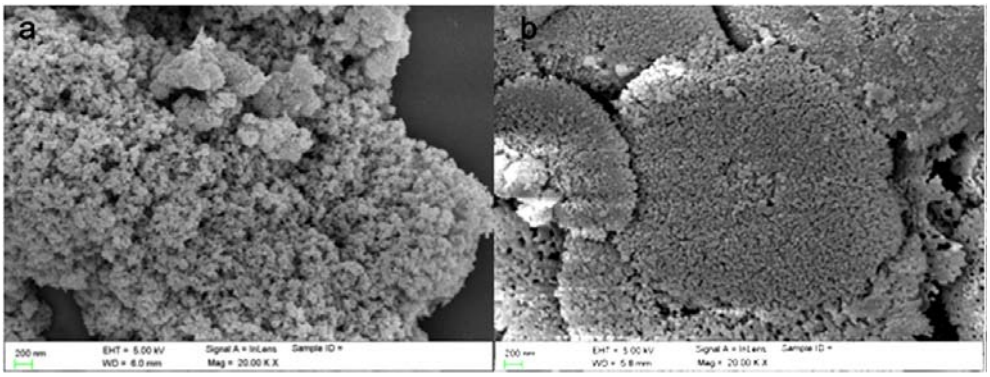

Figure 5.13 SEM images of the calcined products of particles prepared at 23 ˚C with (a) 10% and (b) 15% of F127.

Photocatalytic performance of the calcined products was tested with Orange II solution. The visible light absorbance curves of the original solution (prior to photocatalytic decomposition) and the residual solutions (after photocatalytic decomposition with the calcined products) were recorded. Readings at 484 cm^{-1} were used to calculate the molar ratios of residual Orange II molecules with respect to the original solution, and the results are shown in Figure 5.14a. The amount of residual Orange II molecules increases with the concentration of F127 suggesting a worsening effect on the photocatalytic performance. This effect is closely related to the morphology of the photocatalysts, that is, the calcined products of the precursors prepared with different concentrations of F127. The sample prepared with 10% of F127 consists of only nanoparticles, while that prepared with 15% of F127 contains both mesocrystals and nanoparticles. XRD of the calcined products shows that FWHM of the XRD spectrum for the sample prepared with 10% of F127 is markedly larger in comparison to that with 15% of F127 (Figure 5.14d). In other words, crystallite sizes of the calcined products, calculated according to the Scherrer's equation, increase as the concentration of F127 increases (Figure 5.14b). This variation is consistent with the morphologies of their precursors prior to calcination, because the nanoparticles comprising the mesocrystals are closer to each other and more vulnerable to the Ostwald ripening leading to larger crystallites. Furthermore, such variation in the morphology of the precursors also gives rise to the variations in the BET specific surface areas of the calcined products as shown in Figure 5.14b, c. The precursor of nanoparticles prepared with 10% of F127 gives rise to pure TiO_2 nanoparticles after calcination. The other sample prepared with 15% of F127

consisting of both NH_4TiOF_3 mesocrystals and TiO_2 nanoparticles gives rise to both TiO_2 mesoctystals and TiO_2 nanoparticles. Their difference in photocatalytic performance can therefore be correlated to their morphologies, which give rise to the observed variation in the specific surface areas.

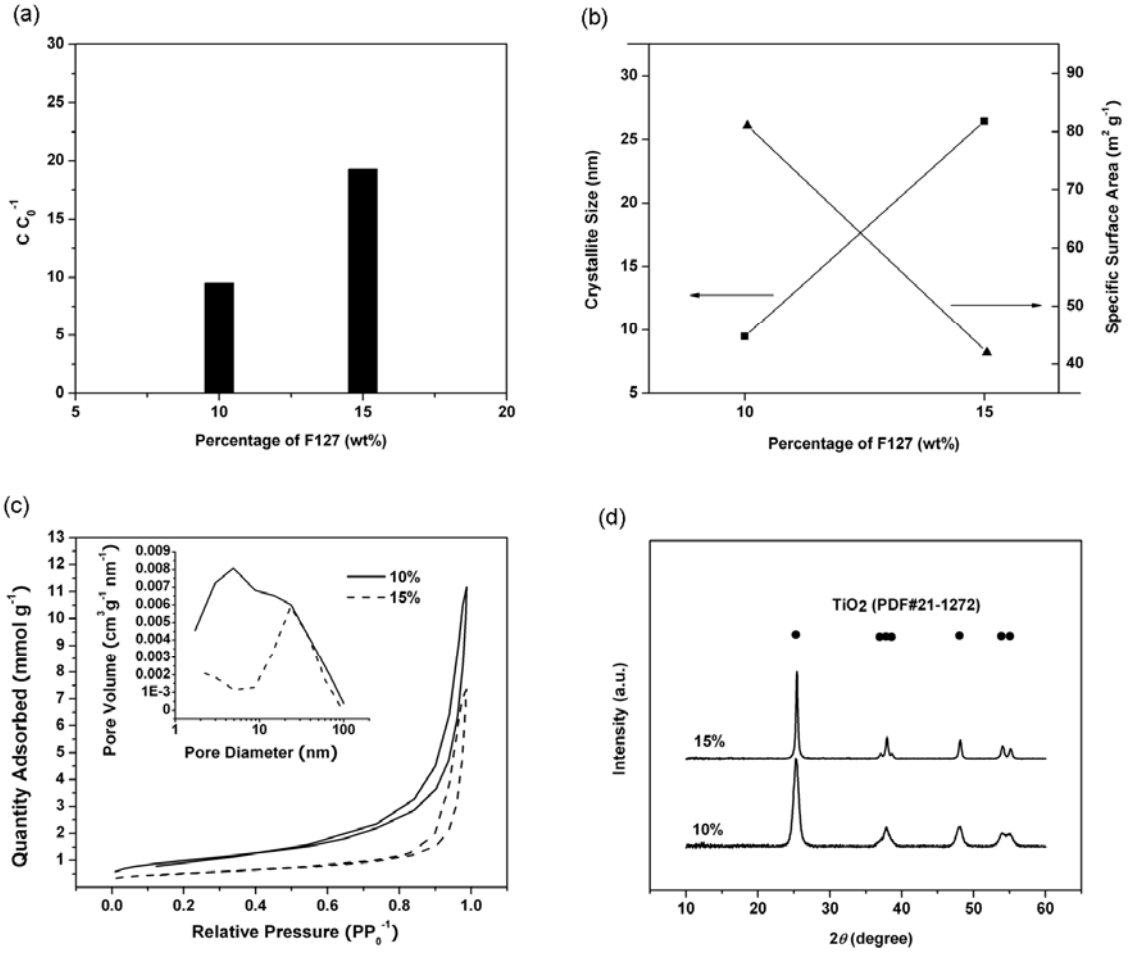

Figure 5.14 Photocatalytic performance, crystallite sizes, and BET results for the thermally treated products. (a) Photocatalytic performance, (b) Crystallite sizes and BET specific surface areas, (c) BET isotherms and pore size distribution (calculated from the desorption branch by Barrett−Joyner−Halenda (BJH) model), (d) XRD of the calcined products of the particles prepared at 23 ˚C with F127 concentrations of 10% and 15%.

5.7 Remarks

The PPO chains of F127 triblock copolymers are demonstrated to impart the steric effect that effectively obstructs mesoscale assembly of NH_4TiOF_3 nanoparticles and consequently the formation of NH_4TiOF_3 mesocrystals. This function is optimized at a surfactant concentration of 10%. Below this concentration, the low surface coverage of F127 gives rise to aggregation of nanoparticles. Above this concentration, however, the hydrophobicity of the PPO chains dominates and induces mesoscale assembly of NH_4TiOF_3 nanoparticles and thereby the formation of NH_4TiOF_3 mesocrystals. It is again confirmed that NH_4TiOF_3 nanoparticles are vulnerable to chemical conversion in water. Unless assembled into the microscale NH_4TiOF_3 mesocrystals, within a few hours, they are readily converted to TiO_2 nanoparticles at 35 ˚C in the mother liquor. Therefore, there is a competition between the mesoscale assembly of NH_4TiOF_3 nanoparticles into NH_4TiOF_3 mesocrystals and the chemical conversion from NH_4TiOF_3 nanoparticles to TiO_2 nanoparticles. Raising temperature to 23 ˚C and then to 35 ˚C facilitates the latter process and therefore TiO_2 nanoparticles are produced, while only NH_4TiOF_3 mesocrystals are obtained at 4 ˚C at the same concentration of F127 (10%). Sterically stabilized nanoparticles prepared at 23 ˚C with 10% of F127 give rise to TiO_2 nanocrystals, whereas NH_4TiOF_3 mesocrystals prepared at 23 ˚C with 15% of F127 give rise to TiO_2 mesocrystals after calcination at 700 ˚C. The TiO_2 nanocrystals show superior photocatalytic performance over TiO_2 mesocrystals, which can be accounted for by their difference in morphology and specific surface areas.

CHAPTER 6. FERROELECTRICITY IN NH_4TIOF_3 MESOCRYSTALS

6.1 Background

Mesocrystal formation induced by hydrophobic interparticle force has been well reported, while the involvement of other interparticle forces is largely overlooked.[4] For the growth of NH_4TiOF_3 mesocrystals, successful use of surfactants Brij 58, Brij 56, Brij 700 and F127 implementing the hydrophobic force has been well documented.[59] However, when pure water or mixture solutions of water and miscible organic liquids (ethanol, ethylene glycol, diethylene glycol, and polyethylene glycol 200) replace the surfactant solution, NH_4TiOF_3 mesocrystals are still developed (Figure 6.1). Traces of the building units are readily observable on the surfaces of NH_4TiOF_3 mesocrystals (Figure6.1c, f). Since the hydrophobic force in these situations is negligible or absent, the assembly mechanism of the building units into mesocrystals becomes very interesting. Furthermore, Lee and Shih also prepared NH_4TiOF_3 "discoid crystals" on glass substrates at 40 ˚C and 2 h with the mixture of aqueous solutions of H_3BO_3 and $(NH_4)_2TiF_6$ in the absence of additives.[63] The NH_4TiOF_3 "discoid crystals" show single crystal diffraction patterns under TEM. Yu et al. prepared NH_4TiOF_3 mesocrystals from H_3BO_3 and $(NH_4)_2TiF_6$ in the mixture of 2-propanol and water at 80 ˚C for 20 h by hydrothermal method.[64] Feng et al. prepared NH_4TiOF_3 mesocrystals from $TiCl_4$ and NH_4F in the mixture of water and ethanol or propanol at 180 ˚C and 12 h by hydrothermal method.[65] Therefore, it is

apparent that NH_4TiOF_3 tends to grow via the route of mesocrystals without necessary relation to the additives introduced or precursors used. Therefore, the correlation between this macroscopic phenomenon and the intrinsic behavior of NH_4TiOF_3 is important for understanding the mesocrystal formation mechanism. Herein, we have studied the ferroelectric behavior of NH_4TiOF_3 mesocrystals The spontaneous dipole-dipole interaction of NH_4TiOF_3 nanocrystals can contribute to their oriented attachment in the mesocrystal formation process

Dipole-dipole interaction is a well-known phenomenon for self-assembly of quantum dots,[21, 28, 29, 142, 143] inorganic nanoparticles,[27, 30, 33, 144] and organic nanoparticles.[35, 36, 145] The phenomenon that the building blocks with dipoles tend to grow via the mesocrystal route is also applicable to polar organic material and inorganic compounds.[14, 35, 36, 145] Impressively, the example of polar organic mesocrystals of DL-Alanine is analogous to the phenomenon observed with NH_4TiOF_3 mesocrystals. Specifically, polar DL-Alanine forms mesocrystals in the presence of block copolymer,[145] alcohol,[36] or even in the absence of any additives.[35] In addition, it has been reported that transition metal oxyfluorides exhibit ferroelectricity.[146-148] In this chapter, the ferroelectric nature of NH_4TiOF_3 is verified by experimental observations using piezoresponse force microscopy (PFM) technique measured by the collaborators (Prof Zeng and Dr Kumar), which is predicted by the density functional calculation performed by the collaborators (Mr Fan and Dr Ong). Spontaneous dipoles in ferroelectric building blocks are demonstrated to lead to the formation of 3D mesocrystals, in consistence with the recent real time observations on oriented attachment.[30, 144]

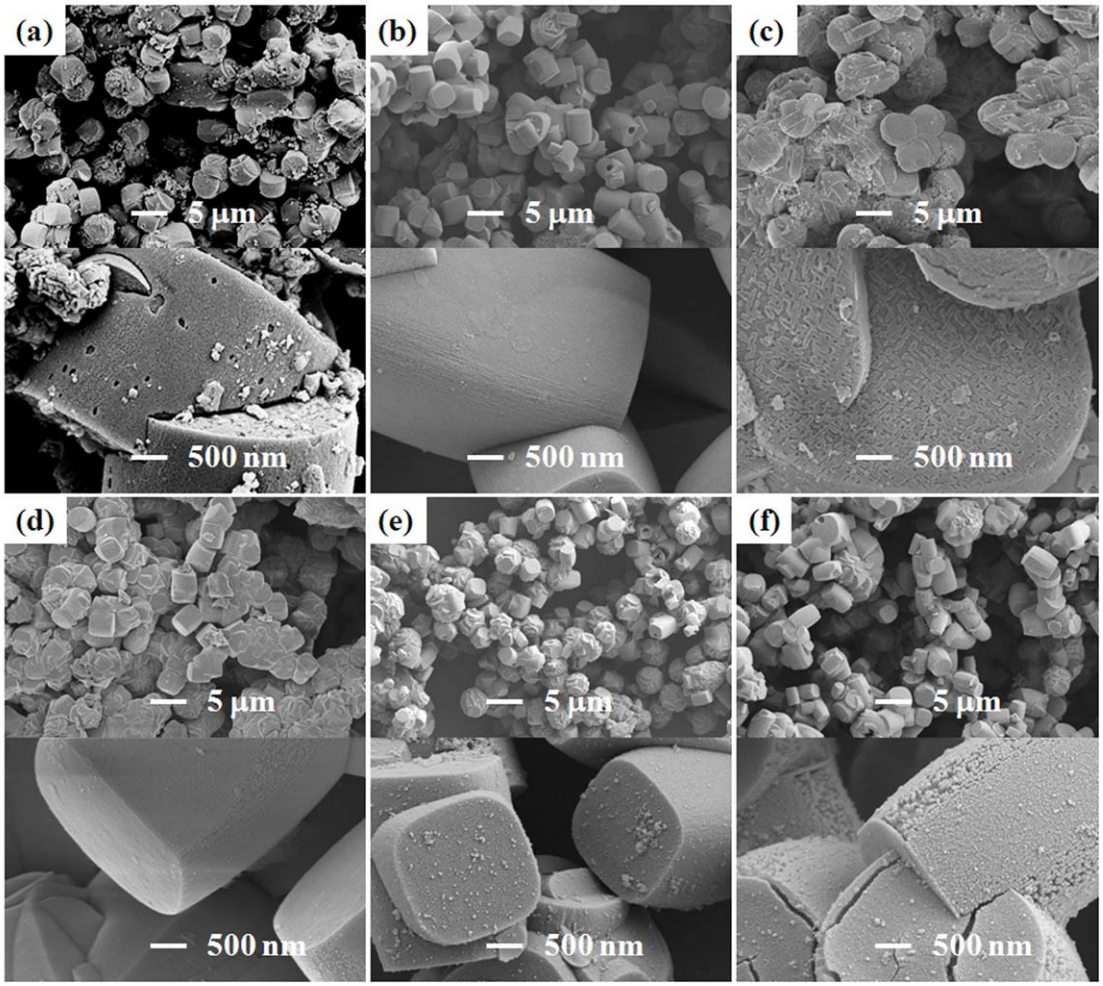

Figure 6.1 SEM of the powder sythesized at 4 ˚C and 3 days in aqueous solution with various additives. (a) no additive; (b) ethanol ($HO\text{-}CH_2\text{-}CH_3$) (10%); (c) polyethylene glycol (PEG, $H\text{-}(O\text{-}CH_2\text{-}CH_2)_4\text{-}OH$) 200 (10%); (d) ethylene glycol (EG, $HO\text{-}CH_2\text{-}CH_2\text{-}OH$) (10%); (e) ethylene glycol (EG) (30%); (f) diethylene glycol (DEG, $HO\text{-}CH_2\text{-}CH_2\text{-}O\text{-}CH_2\text{-}CH_2\text{-}OH$) (30%). When pure water or mixture solutions of water and additives of miscible organic liquids (ethanol, ethylene glycol, diethylene glycol, and polyethylene glycol 200) are used instead of surfactant solutions, NH_4TiOF_3 mesocrystals are steadily formed.

6.2 Experimental Details

Sample preparation: Surfactant Brij 58 (Aldrich, 3 g) was dissolved in DI water (10g) first. Fluoride scavenger H_3BO_3 (99.8%, Merck, 123.7 mg) was then dissolved.

Lastly, $(NH_4)_2TiF_6$ (99.99%, Aldrich, 198.0 mg) was added. When $(NH_4)_2TiF_6$ was well dissolved, a piece of fluorine-doped tin oxide (SnO_2:F) (FTO) coated glass (TEC15, Dyesol) was inserted into the solution. NH_4TiOF_3 mesocrystals were allowed to grow under static condition in a PPE tube. After 3 h, the glass was removed from solution and dipped in water to remove inorganic impurities and subsequently ultrasonicated for 5 s in ethanol to remove Brij 58 molecules and the mesocrystals which were loosely attached to the substrate. Drying was done by purging with N_2. The solid particles in the solution were then recovered by centrifugation and washing successively for three times. The solvents used for washing were water, acetone and ethanol. Drying of powder was carried out at 60 ˚C for 12 h.

To experimentally observe ferroelectricity of NH_4TiOF_3 mesocrystals, I first tried the conventional P-E loop measurement[149]which turned out to be problematic. Firstly, the disk samples could not be densified by calcination due to decomposition of NH_4TiOF_3 above 200 ˚C. Secondly, as a consequence, the gold-dots-sputtered disk samples turned out to be fatally leaky and no macroscopic P-E polarization hysteresis loops were measurable. Therefore, I prepared samples for piezoresponse force microscopy (PFM) measurement, a technique suitable for local P-E loop and imaging. Since PFM operates in contact mode, the NH_4TiOF_3 mesocrystals must be adhered strongly to the substrate so that they do not move during measurement. I placed different substrates in the reaction solution and found NH_4TiOF_3 mesocrystals could grow and adhere strongly to fluorine-doped tin oxide (FTO) film coated glass substrates during PFM measurement. To prevent the aggregation of mesocrystal

NH_4TiOF_3surfactant Brij 58 (23 wt%) has been introduced. Growth time was limited to 3 h for a smaller particle size so that the canteliver tip can keep contact with particle surface better at the edges of particles during PFM measurement. **Computation method:** As collaborators for this project, Fan Zhen and Dr Ong performed computational studies with NH_4TiOF_3 mesocrystals. For the first principle calculations they employed the PBE-GGA approximation[150, 151] as implemented in the Vienna Ab initio Simulation Package (VASP),[152] which employ the Projected Augmented Wave (PAW) method.[153, 154] A 4×4×2 Monkhorst-Pack *k*- mesh and an energy cut-off of 400eV for plane waves were used. Within their calculations, all atoms in NH_4TiOF_3 mesocrystal (since now we call it NH_4TiOF_3 for abbreviation) are fully relaxed until the Hellmann-Feynman forces are less than 20 meV/Å. The electronic polarization is calculated using the Born effective charge method.[155, 156]

6.3 Theoretical Prediction

The NH_4TiOF_3 mesocrystal exhibit a sandwich crystal structure with layers of $[TiOF_3]^-$ pseudo-octahedra, which are inter-connected via the corners in *ab*-plane, stacked and sandwiched by $[NH_4]^+$ tetrahedral along the *c*-direction, see Figure 6.2. Its lattice parameters have been reported to be a=7.51 Å, b=7.58 Å, c=12.61 Å, and angles $\alpha=\beta=\gamma=90^o$.[70] In one unit cell, there are 8 $[TiOF_3]^-$ octahedron (1 from 8 corners, 3 from 12 edge centers, 3 from 6 surface centers and 1 at body center) and 32 sites where the 24 F atoms and the 8 O atoms reside. On average, each octahedron has 1 Ti atom, 1 O atom and 3 F atoms, namely, $[TiOF_3]^-$. Therefore each $[TiOF_3]^-$ octahedron has an electronic polarization in which polarization orientation is

dependent on the position of O atom. The positions of O and F atoms in NH_4TiOF_3 have not been reported to date. To optimize the position of O and F atoms in NH_4TiOF_3, based on the valence-sum rule[157] which requires that the sum of the bond valences at Ti atoms equals to the atomic valence, there are only two different types of crystal structure depending on the position of oxygen atoms, (i) tops of $[TiOF_3]^-$ octahedra, i.e. along the *c*-axis, and (ii) in *ab*-plane.

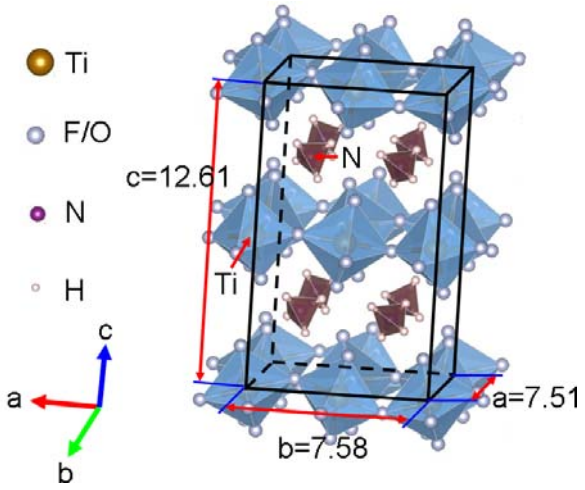

Figure 6.2 Crystal structure of NH_4TiOF_3 (Courtesy by Dr Khuong Phuong Ong and Mr Fan Zhen)

For case (i), O atoms reside at the tops of the $[TiOF_3]^-$ octahedra, i.e. along the *c*-axis, and there are 8 possible structures including three types of antiferroelectric order and one type of ferroelectric order. The antiferroelectric order include A-type (A_1, A_2, A_3 corresponding to Figure 6.3a, Figure 6.3b, and Figure 6.3c, respectively), C-type (C_1, C_2, C_3 corresponding to Figure 6.3d, Figure 6.3e, and Figure 6.3f, respectively), and G-type (Figure 6.3g). The ferroelectric order is along the *c*-axis (F_c corresponding to Figure 6.3h). In the case (ii) where O atoms lie in the *ab*-plane, two

possible crystal structures A_a and A_b are shown in Figure 6.3, where O atoms are at the corners of $[TiOF_3]^-$ octahedron arranged along the *a*-axis (Figure 6.3i) and along the *b*-axis (Figure 6.3j), respectively. The results show that both structures A_a and A_b which are antiferroelectric, are more stable in comparison to structures of case (i) (Table 1). This suggests that O atoms do not prefer to reside at the tops of $[TiOF_3]^-$ octahedron along the *c*-axis. To double check this conclusion a structure combining case (i) and (ii), $M_{i\text{-}ii}$ (Figure 6.3k), with some O atoms located at the corners along the *a*-axis and the rest at the tops along the *c*-axis has been studied. The result (Table 1) shows that it is not a stable structure in comparison to structures A_a and A_b.

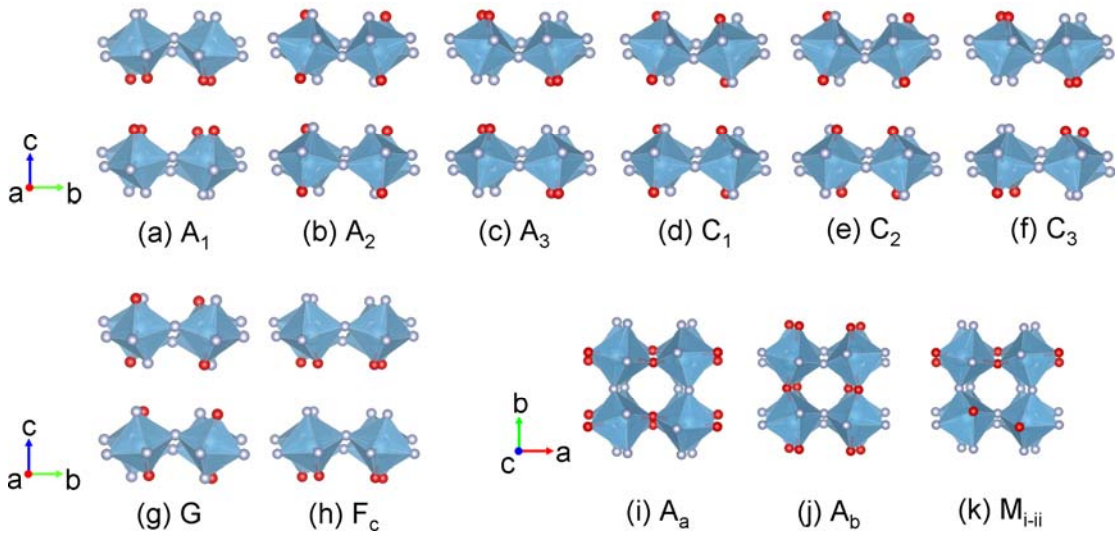

Figure 6.3 Possible structures of NH_4TiOF_3 (a) A_1, (b) A_2, (c) A_3, (d) C_1, (e) C_2, (f) C_3, (g) G (h) F_c, (i) A_a, (j) A_b, and (k) $M_{i\text{-}ii}$. The red circles are O atoms and the white circles are F atoms. Ti atoms are in the octahedra. $[NH_4]^+$ tetrahedra are omitted for simplicity of figures. (Courtesy by Dr Khuong Phuong Ong and Mr Fan Zhen).

Table 6.1 Possible crystal structure of NH_4TiOF_3 (Courtesy by Dr Khuong Phuong Ong and Mr Fan Zhen)

Type	Space group	Energy (eV/formular unit)	Polarization (μC/cm^2)		
			P_a	P_b	P_c
A_1	P_1	-58.59858	0	0	0
A_2	P_1	-58.59687	0	0	0
A_3	P_1	-58.58842	0	0	0
C_1	P_1	-58.59772	0	0	0
C_2	$P2_1$	-58.60211	0	0	0
C_3	$P2_1$	-58.60009	0	0	0
G	$P2_1$	-58.59953	0	0	0
F_c	$P2_1$	-58.60133	0	0	6.938
A_a	$P2_12_12_1$	-59.03144	0	0	0
A_b	$P2_12_12_1$	-59.01927	0	0	0
$M_{i\text{-}ii}$	P_1	-58.83635	8.937	0.187	2.643
F	P_1	-59.11410	8.586	5.363	0.072
F_{zig}	P_1	-59.11816	8.175	0.306	1.658

It is therefore inferred that O atoms prefer to stay in the *ab*-plane. In this configuration, the larger electronegativity of O atoms, in comparison to F atoms, is better satisfied by interacting with two neighboring Ti atoms. It is further noticed that the distances between an O atom and two nearest Ti atoms are not the same, i.e. ~ 1.7 Å and ~ 2.2 Å, in both A_a and A_b structures. This means that the O atoms at corners in *ab*-plane will not be shared equally between two $[TiOF_3]^-$ octahedra but strongly bonded to one $[TiOF_3]^-$ octahedron and weakly bonded to the other. We further propose two other crystal structures (Figure 6.4) based on structure A_a.[1] In structure F (Figure 6.4a), both chains of $[TiOF_3]^-$ along *a*-axis and *b*-axis are ferroelectric. In structure F_{zig} (Figure 6.4b), the chain of $[TiOF_3]^-$ along *a*-axis is ferroelectric and the

other along *b*-axis is antiferroelectric. The results show that these two new structures are ferroelectric and more stable than structure A_a (Table 1) and the structure F_{zig} is the most stable structure for NH_4TiOF_3. By this, we conclude that NH_4TiOF_3 is a ferroelectric with structure F_{zig} and the electronic polarization of (8.175, 0.306, 1.658) $\mu C/cm^2$. To confirm the theoretical prediction of Fan Zhen and Dr Ong on the ferroelectricity of NH_4TiOF_3, we conduct experiments to verify it.

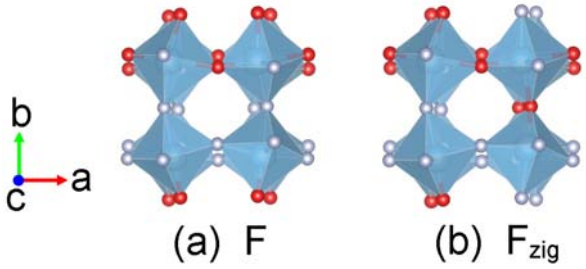

Figure 6.4 Possible ferroelectric structures of NH_4TiOF_3, (a) F structure and (b) F_{zig} structure. The red balls are O atoms and the white balls are F atoms. Ti atoms are in the octahedra. $[NH_4]^+$ tetrahedra are omitted for simplicity of figures. (Courtesy by Dr Khuong Phuong Ong and Mr Fan Zhen)

6.4 Mesocrystal Characterization

Scanning electron microscopy (SEM, Figure 6.5a) shows that the individual particles are successfully deposited on the FTO coated glass substrate. Some platelet particles lie more or less flat on the substrate while some attach to the substrate from the sides. X-ray diffraction (XRD, Figure 6.5b) spectra reveal that the powder obtained is NH_4TiOF_3 which corresponds to the peaks of PDF card number 52-1674 very well. In addition, the peaks for the NH_4TiOF_3 deposited FTO glass can be indexed to NH_4TiOF_3 and FTO. Furthermore, Transmission Electron Microscopy

(TEM, Figure 6.5c-f) shows that the particles from the collected powder are NH_4TiOF_3 mesocrystals as different spots of the same particle (center and edges) show the same single-crystal-like selected area electron diffraction (SAED) patterns which correspond to the [001] zone of NH_4TiOF_3. The top surface diagonals along the slightly truncated corners of the particle correspond to the [010] and [100] crystallographic directions of NH_4TiOF_3.

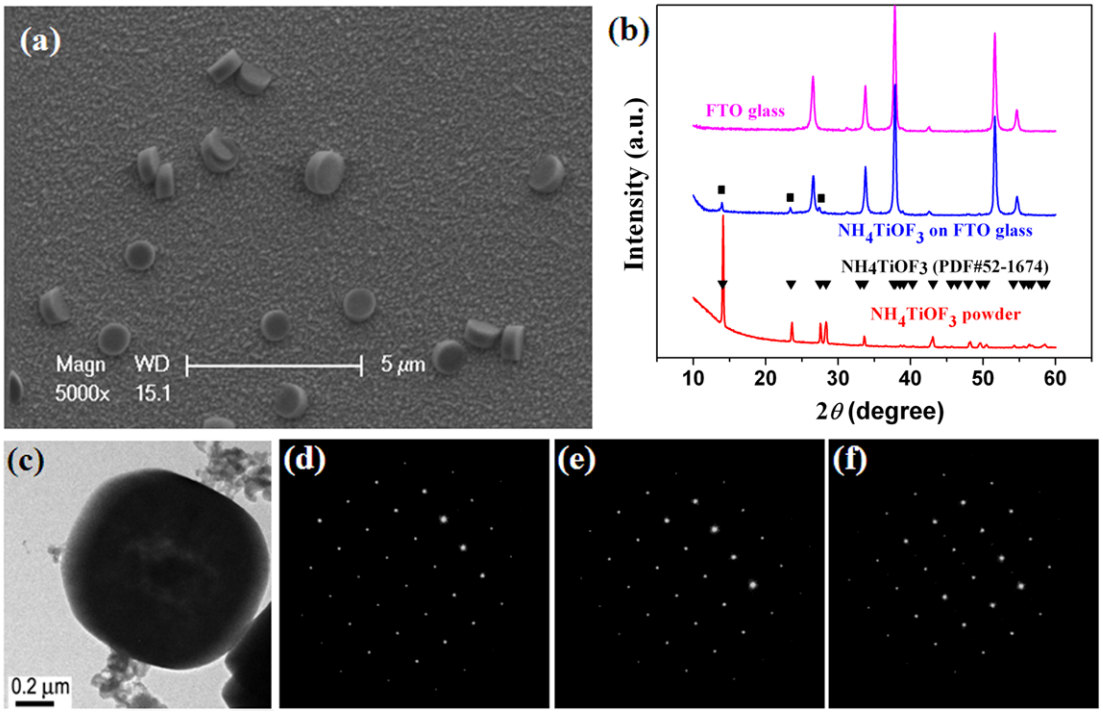

Figure 6.5 Characterization of NH_4TiOF_3 mesocrystals deposited on FTO glass. (a) SEM of NH_4TiOF_3 mesocrystals on FTO glass prepared at 23 ℃ for 3 h; (b) XRD spectra of FTO glass, NH_4TiOF_3 mesocrystals on FTO glass, and NH_4TiOF_3 powder; (c) TEM image of a microscale NH_4TiOF_3 mesocrystal from powder synthesized at 23 ℃ for 3 h; (d)-(f) selected area electron diffraction (SAED) patterns for different spots (center and edges) of the microscale mesocrystal shown in panel (c).

6.5 Ferroelectricity by PFM

PFM is an efficient tool to study the ferroelectric polarization and its switching

behavior for a material at nanoscale.[158] Figure 6.6 shows the PFM and switching spectroscopy results measured on one individual NH_4TiOF_3 mesocrystal. From the topography image in Figure 6.6a, it is observed that the mesocrystal is constructed from grains, which suggests that the mesocrystal is not grown by the classical crystallization growth process i.e. 'ion-by-ion' but by a non-classical crystallization process, i.e., mesoscale assembly of particles. Figure 6.6b, c show the corresponding PFM amplitude and phase response, respectively. Most of the grains in the mesocrystal show piezoresponse (Figure 6.6b) and upward polarization (180^o) (Figure 6.6c). To investigate the observed polarization for the ferroelectric like behavior, a switching spectroscopy method is used to switch the polarization. Phase and amplitude switching results in Figure 6.6d, e show that the polarization can be switched in a similar manner as ferroelectric polarization by an external electric field.

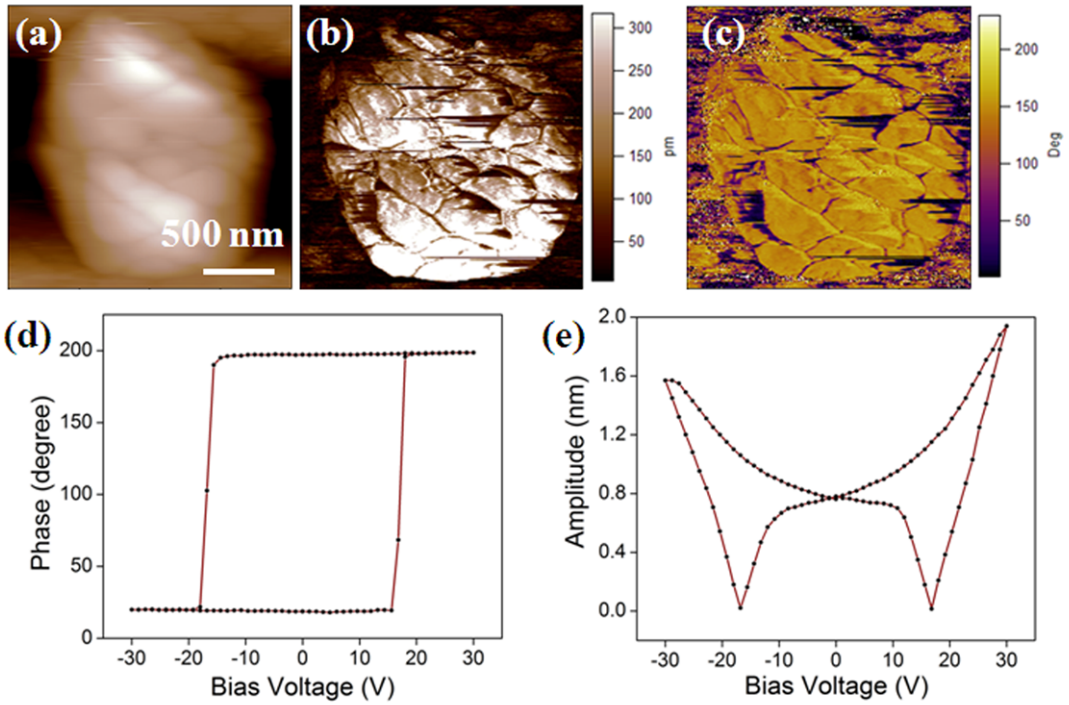

Figure 6.6 PFM and switching spectroscopy for NH_4TiOF_3 mesocrystal. (a) topography, (b) amplitude, (c) phase, (d) phase hysteresis loop and (e) corresponding amplitude hysteresis loop. (Courtesy by Prof Zeng Kaiyang and Dr Amit Kumar)

Another method to switch the polarization, so called dc writing or poling, is also applied on the same sample to switch the observed polarization (Figure 6.7). A +15 V dc bias is first applied on the mesocrystal using a line scan method.[15, 159] Figure 6.7a, d shows the phase and amplitude response of the same mesocrystal after the dc writing process. All the polarization dipoles get aligned in upward direction.. To switch the upward aligned polarization to the downward direction a negative (-15 V) dc bias is applied on the same area. Figure 6.7b, e show that most of the polarization dipoles have been switched to the downward direction after the negative dc bias writing, revealing that this polarization can also be erased and written similarly to conventional ferroelectric polarization. To testify against the possibility of charge

effect in polarization switching this sample was held for 1 hr after the negative dc bias writing and measured for PFM response again. Results in Figure 6.7c, f show that even after 1 hr the switched polarization is still stable. Therefore, this polarization is due to the ferroelectric domains present in the material, which can be switched by the application of external electric fields.

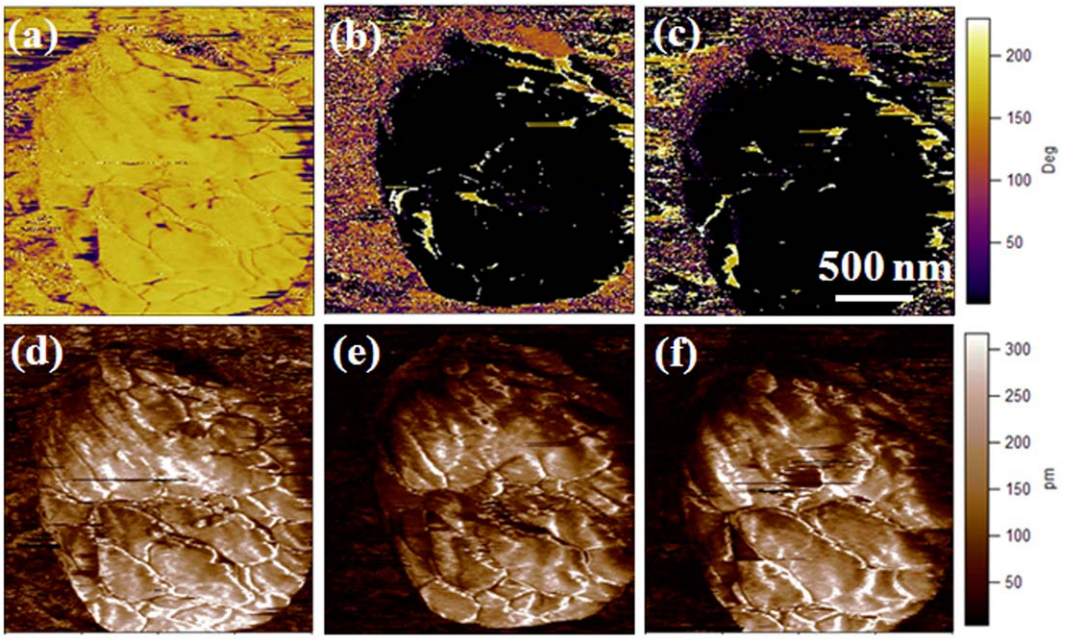

Figure 6.7 dc bias writing results for NH_4TiOF_3 mesocrystal (a) & (d) phase and amplitude response after +15 V bias application, (b) & (e) phase and amplitude response after the -15 V dc bias application, (d) & (f) phase and amplitude response 1 hour after -15 V bias application. (Courtesy by Prof Zeng Kaiyang and Dr Amit Kumar).

To further investigate the nature of ferroelectric domains in NH_4TiOF_3 mesocrystal, both lateral and vertical PFM responses are measured using vector PFM. The vertical and lateral PFM responses are recorded simultaneously for a single

mesocrystal (Figure 6.8). Vertical PFM measures the out-of-plane (OP) component of the polarization in z-direction (P_z) whereas Lateral PFM measures the in-plane (IP) component of the polarization either in x-direction or y-direction (P_x or P_y) (x, y, and z are laboratory coordinates). If all the three components of polarization are known at the same location of a sample, it is possible to construct a 3D map of domain orientation. However, due to technical constraint in measuring all three responses at the same location, 3D maps are difficult to construct. Instead, 2D maps for P_z and P_x or P_y are usually reported.[160] Figure 6.8a, d shows topography and the corresponding SEM image of NH_4TiOF_3 mesocrystal that is attached from its side on the FTO coated glass substrate. The vertical amplitude and phase response (OP) of this mesocrystal is shown in Figure 6.8b, c and its corresponding lateral amp and phase responses (IP) are shown in Figure 6.8e, f. We adopted the convention that the bright and dark in-plane contrast stands for right and left polarization components, respectively, relative to the cantilever's long axis.[160] From these vector PFM results for the NH_4TiOF_3 mesocrystal, it is concluded that the mesocrystal is not likely a single domain, rather, a multi-domain structure.

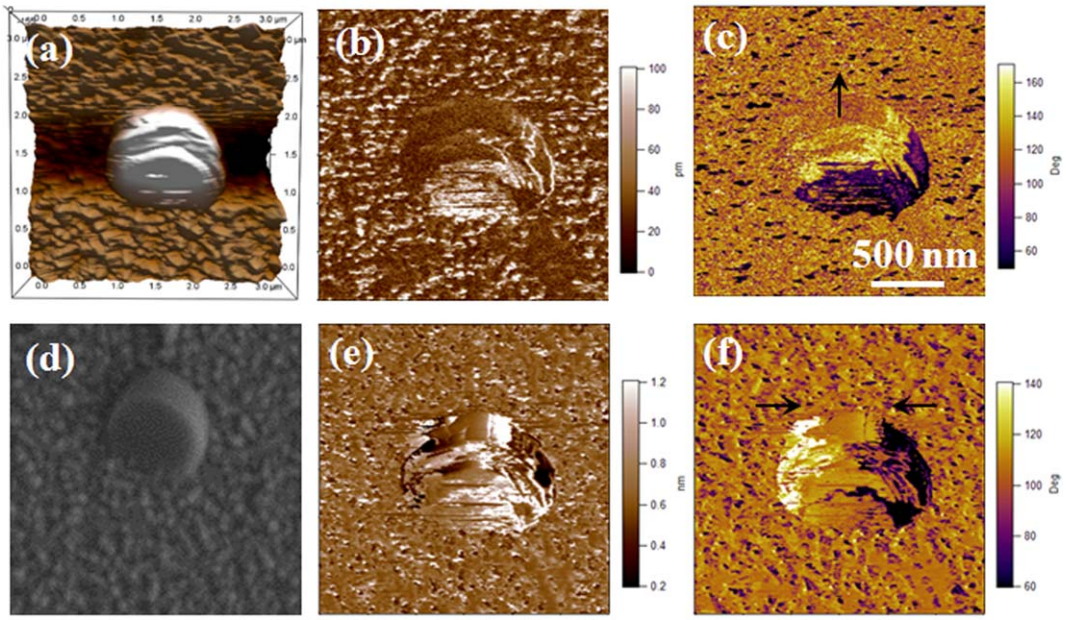

Figure 6.8 Vector PFM of an NH_4TiOF_3 mesocrystal grown on a FTO coated glass substrate (Courtesy by Prof Zeng Kaiyang and Dr Amit Kumar). (a) 3D topography, (b) vertical amplitude response, (c) vertical phase response, the arrow indicate upward polarization component in the yellow areas, (d) SEM of a particle which is oriented in similar way, (e) Lateral amplitude response, (f) lateral phase response, the arrows indicate left and right polarization components in the black and white contrast, respectively.

6.6 Remarks

In summary, the first-principle calculations by the collaborators suggest that ferroelectricity of NH_4TiOF_3 can arise from ordering of O and F. PFM measurement by the collaboators reveals that the NH_4TiOF_3 mesocrystals exhibit both ferroelectric and piezoelectric behavior. Further studies by vector PFM suggest that the NH_4TiOF_3 mesocrystals show multi polarization domains. Ferroelectricity may have well contributed to the non-classical crystallization process of NH_4TiOF_3 via dipole-dipole interaction of the building units leading to the wide observation that

NH_4TiOF_3 mesocrystals tend to form in various conditions. This speculation complements our previous observation that once F is removed from NH_4TiOF_3, TiO_2 aggregates instead of mesocrystals are formed. The resultant weak short-range dipole-dipole interaction is also supported by the work in Chapter 5 that steric hindrance exerted by PPO chains (PO_{70}) of F127 can retard the formation of NH_4TiOF_3 mesocrystals. Sharp and complete switching of dipoles in NH_4TiOF_3 mesocrystals suggests the promising application in ferroelectric non-volatile random access memory (FRAM).

CHAPTER 7. CONCLUSIONS

As detailed in Chapter 3, concerning the anisotropic dissolution of NH_4TiOF_3 mesocrystals, they appear to be able to convert to more stable TiO_2 (anatase) phase. Their anisotropic dissolution is observed in both *in-situ* and *ex-situ* studies. In both cases, dissolution initiates from the mesocrystal center, where the concentration of occluded surfactant molecules is the highest. This is followed by the propagation of dissolved hole in the mesocrystal center. The dissolution propagates preferentially in the <100> and <010> directions, where it is thermodynamically driven by the conversion of NH_4TiOF_3 to more stable TiO_2 via losing N and F elements. The observed anisotropic behavior is caused by the difference in activation energy of the corresponding planes that are being dissolved. The activation energy appears to be associated with the planar densities of N and F elements.

The formation of NH_4TiOF_3 mesocrystals can be manipulated, as discussed in Chapter 4. Three factors affecting the formation of NH_4TiOF_3 mesocrystals, i.e., temperature, the presence of surfactant Brij 58 (23%) and pH of the reaction solution, have been identified. The route that leads to the formation of TiO_2 aggregates competes against the mesoscale assembly of NH_4TiOF_3 nanocrystals into NH_4TiOF_3 mesocrystals. Raising temperature and increasing solution pH both favor the conversion from NH_4TiOF_3 nanocrystals to TiO_2 nanoparticles. The presence of Brij 58 (23%) facilitates the mesoscale assembly process. In the presence of Brij 58 and at 4˚C, a high solution pH promotes the conversion rate of NH_4TiOF_3 nanocrystals to TiO_2 nanoparticles and thereby reduces the amount of NH_4TiOF_3 nanocrystals

available for the formation of NH_4TiOF_3 mesocrystals. The resultant NH_4TiOF_3 mesocrystals show an increase in pore volume with the solution pH.

The formation of NH_4TiOF_3 mesocrystals can be further manipulated by the surfactant hydrophobicity, as the relative conversion rate from NH_4TiOF_3 to TiO_2 (anatase) was changed when surfactant F127 was introduced, instead of Brij 58 as discussed in Chapter 5. The PPO chains of F127 triblock copolymers are demonstrated to impart the steric effect that effectively obstructs mesoscale assembly of NH_4TiOF_3 nanoparticles and consequently the formation of NH_4TiOF_3 mesocrystals at appropriate concentrations. This function is optimized at the surfactant concentration of 10%. Below this concentration, the low surface coverage of F127 gives rise to the aggregation of nanoparticles. Above this concentration, however, hydrophobicity of the PPO chains dominates and induces mesoscale assembly of NH_4TiOF_3 nanoparticles and thereby the formation of NH_4TiOF_3 mesocrystals. It is again confirmed that NH_4TiOF_3 nanoparticles are vulnerable to chemical conversion in water. Unless assembled into the microscale NH_4TiOF_3 mesocrystals, within a few hours, they are readily converted to TiO_2 nanoparticles at 35 ˚C in the mother liquor. Therefore, there is a competition between the mesoscale assembly of NH_4TiOF_3 nanoparticles into NH_4TiOF_3 mesocrystals and the chemical conversion from NH_4TiOF_3 nanoparticles to TiO_2 nanoparticles. Raising temperature to 23 ˚C and then 35 ˚C facilitates the latter process and therefore TiO_2 particles are produced, while only NH_4TiOF_3 mesocrystals are obtained at 4 ˚C at the same concentration of F127 (10%).

It is demonstrated in Chapter 6 that the ferroelectricity of NH_4TiOF_3 have

contributed to formation of NH_4TiOF_3 mesocrystals, where they assemble as a result of the dipole-dipole interaction of NH_4TiOF_3 nanocrystals in the absence of surfactant. The first-principle calculations by our collaborators suggest that the ferroelectricity of NH_4TiOF_3 arises from ordering of O and F atoms. PFM measurement reveals that the NH_4TiOF_3 mesocrystals exhibit both ferroelectric and piezoelectric behavior. Further studies by vector PFM suggest that the NH_4TiOF_3 mesocrystals show multi polarization domains. This observation of ferroelectricity for NH_4TiOF_3 complements the previous observation that once F is removed from NH_4TiOF_3, TiO_2 aggregates instead of mesocrystals are formed. The resultant weak short-range dipole-dipole interaction is also supported by the work in Chapter 5 that the steric hindrance exerted by PPO chains (PO_{70}) of F127 can easily retard the formation of NH_4TiOF_3 mesocrystals. Besides the typical applications forthe topotactic reaction product TiO_2 (anatase), e.g. photocatalysts, photovoltaics, NH_4TiOF_3 may therefore find promising applications in ferroelectric non-volatile random access memory (FRAM), when further developed.

CHAPTER 8. SUGGESTIONS FOR FUTURE WORK

8.1 Preparation of NH_4TiOF_3 Thin Films

Given the ferroelectric behavior of NH_4TiOF_3 mesocrystals demonstrated by the experimental observation in the present work, mesocrystals in thin film forms will be of interest to several applications. To prepare the NH_4TiOF_3 thin films, cautions must be exercised such that the substrate does not contain any fluorine scavenger; otherwise, TiO_2 may be produced instead.

8.2 Treatment With Water at High Temperature

Figure 8.1 shows that the NH_4TiOF_3 mesocrystals can be assembled into hierarchical structures with dramatic variations in morphology. However, due to the tiny amount of samples synthesized, phase identification by XRD has not been possible. However, according to our experimental experiences on the chemical instability of NH_4TiOF_3, these structures are likely to be TiO_2. The formation mechanism is however yet to be understood and such interesting morphologies may give rise to different performances in photocatalyst and photovoltaic applications.

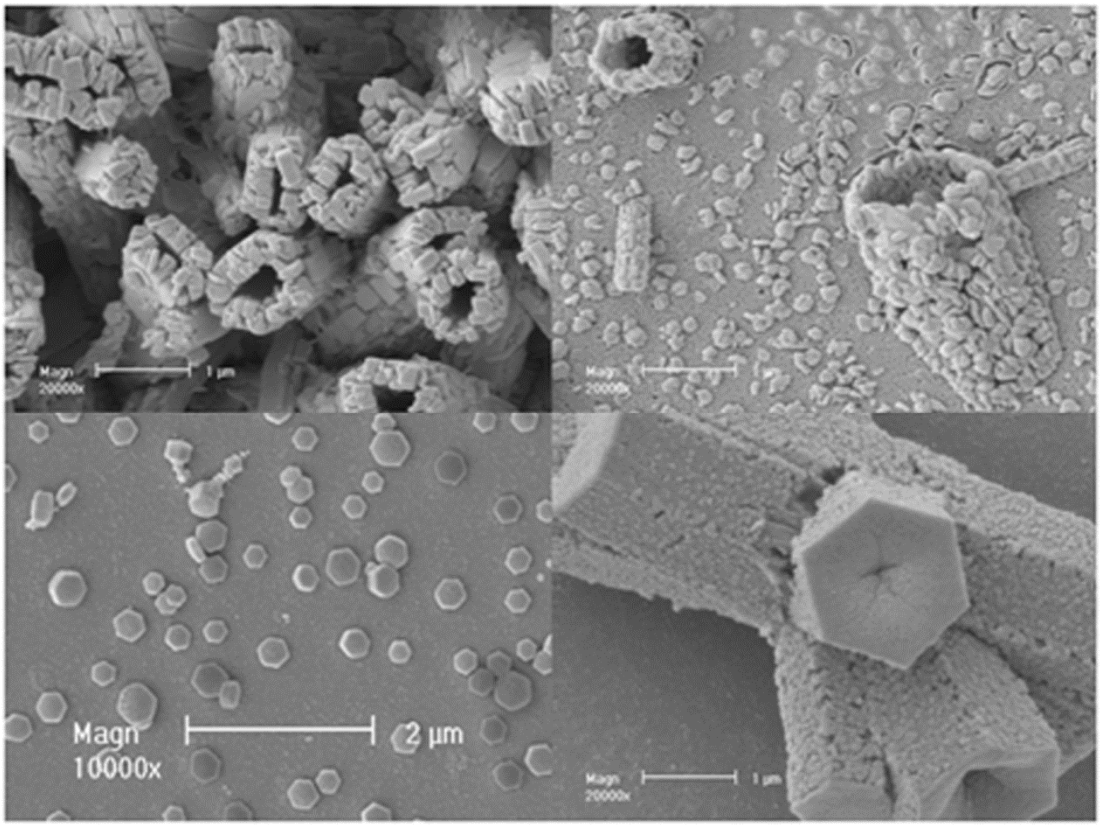

Figure 8.1 Various morphologies obtained by thermal treatment of the as-synthesized NH_4TiOF_3 mesocrystals up to 400 ˚C in water.

8.3 Treatment With Boric Acid

Treatment with boric acid leads to self-assembled hierarchical structures in various forms, as shown in Figure 8.2. According to Zhou et al., they are TiO_2 (anatase).[59] The formation mechanism is however far from being properly understood, and such assembled / layered structures may also give rise to interesting performances.

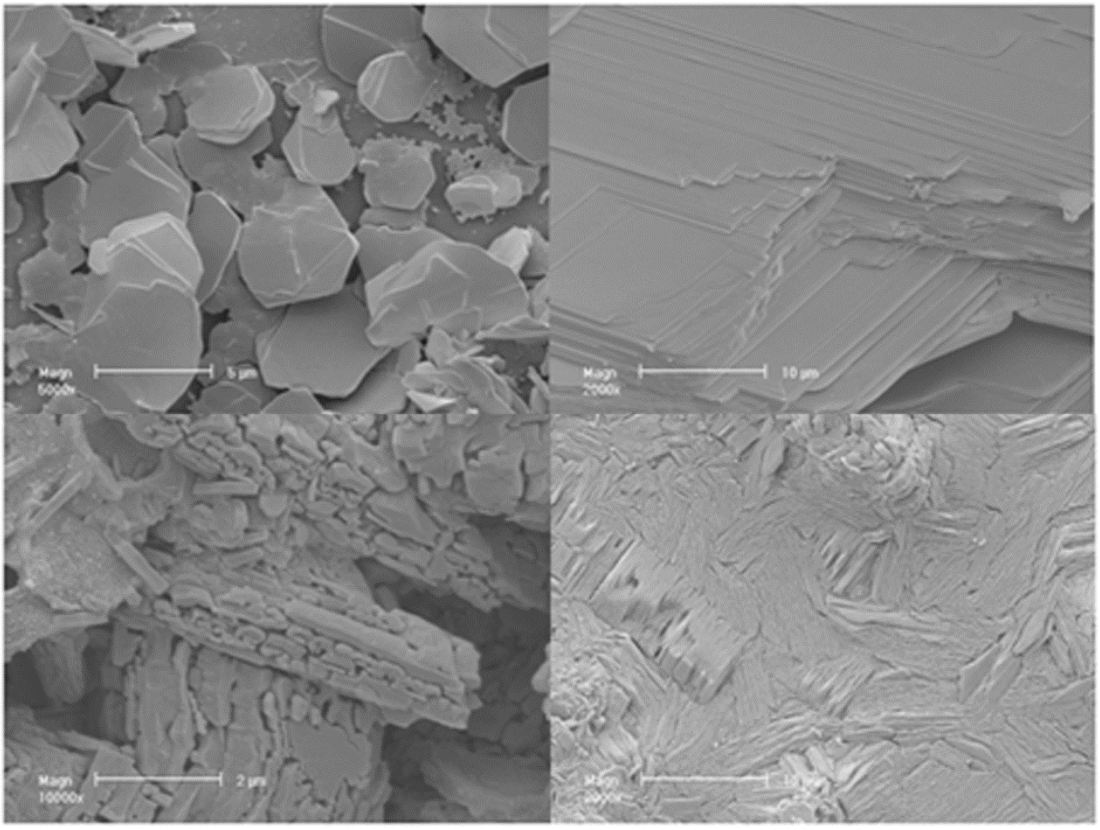

Figure 8.2 various morphologies obtained by treating the as-synthesized NH_4TiOF_3 mesocrystals in H_3BO_3 solution at room temperature.

8.4 Photocatalytic Performances of N and F Doped TiO_2

We have conducted some preliminary study on calcining NH_4TiOF_3 mesocrystals in different environment, i.e., air, nitrogen and argon. Yellowish TiO_2 (anatase) was obtained in air, and green TiO_2 (anatase) in nitrogen or argon. The color change indicates different level of nitrogen and fluorine doping and suggests a shift in band edge. Doping TiO_2 (anatase) with nitrogen and fluorine can be promising for visible light photocatalysis.

8.5 New Compound and Structure with Na^+ Precursors

When Na^+ precursors are introduced into the reaction solution, hexagonal rod shaped mesocrystals are obtained. TEM show single-crystal-like feature of them. XRD phase analysis however shows they are new compounds. In comparison to the elemental analysis results of NH_4TiOF_3, these mesocrystals show smaller amounts of nitrogen and hydrogen, and however a substantial amount of sodium. Na^+ ions may have replaced some NH_4^+ forming the new compounds. PFM shows that these mesocrystals are also ferroelectric, while they can also be converted to TiO_2 (anatase) in the same way as NH_4TiOF_3 mesocrystals are converted to TiO_2 (anatase). It would therefore be of considerable interst to clarify the effect of Na^+ ions on NH_4TiOF_3 mesocrystals.

BIBLIOGRAPHY

(1) Petres, J. J.; Dezelic, G.; Tezak, B. *Croat. Chem. Acta* **1969,** *41*, 183-186.

(2) Cölfen, H.; Mann, S. *Angew. Chem. Int. Ed.* **2003,** *42*, 2350-2365.

(3) Cölfen, H.; Antonietti, M. *Angew. Chem. Int. Ed.* **2005,** *44*, 5576-5591.

(4) Song, R.-Q.; Cölfen, H. *Advanced Materials* **2010,** *22*, 1301-1330.

(5) Li, H.; Estroff, L. A. *CrystEngComm* **2007,** *9*, 1153-1155.

(6) Inumaru, K. *Catal. Surv. Asia* **2006,** *10*, 151-160.

(7) Yu, S. H.; Cölfen, H.; Tauer, K.; Antonietti, M. *Nature Materials* **2005,** *4*, 51-55.

(8) Yu, S. H.; Cölfen, H.; Mastai, Y. *Journal of Nanoscience and Nanotechnology* **2004,** *4*, 291-298.

(9) Li, M.; Schnablegger, H.; Mann, S. *Nature* **1999,** *402*, 393-395.

(10) Feigin, R. I.; Napper, D. H. *J. Colloid Interface Sci.* **1980,** *75*, 525-541.

(11) Murphy, C. J.; Thompson, L. B.; Alkilany, A. M.; Sisco, P. N.; Boulos, S. P.; Sivapalan, S. T.; Yang, J. A.; Chernak, D. J.; Huang, J. *J. Phys. Chem. Lett.* **2010,** *1*, 2867-2875.

(12) Sun, Z.; Ni, W.; Yang, Z.; Kou, X.; Li, L.; Wang, J. *Small* **2008,** *4*, 1287-1292.

(13) Penn, R. L.; Banfield, J. F. *Geochim. Cosmochim. Acta* **1999,** *63*, 1549-1557.

(14) Pacholski, C.; Kornowski, A.; Weller, H. *Angew. Chem. Int. Ed.* **2002,** *41*, 1188-1191.

(15) Herng, T. S.; Kumar, A.; Ong, C. S.; Feng, Y. P.; Lu, Y. H.; Zeng, K. Y.; Ding, J. *Sci. Rep.* **2012,** *2*, 587.

(16) Polleux, J.; Pinna, N.; Antonietti, M.; Niederberger, M. *Adv. Mater.* **2004,** *16*, 436-439.

(17) Xu, A.-W.; Antonietti, M.; Yu, S.-H.; Cölfen, H. *Adv. Mater.* **2008,** *20*, 1333-1338.

(18) McGilly, L.; Byrne, D.; Harnagea, C.; Schilling, A.; Gregg, J. *Journal of Materials Science* **2009,** *44*, 5197-5204.

(19) Dang, F.; Kato, K.; Imai, H.; Wada, S.; Haneda, H.; Kuwabara, M. *CrystEngComm* **2010,** *12*, 3441-3444.

(20) Dang, F.; Kato, K.; Imai, H.; Wada, S.; Haneda, H.; Kuwabara, M. *Ultrason. Sonochem.* **2010,** *17*, 310-314.

(21) Cho, K.-S.; Talapin, D. V.; Gaschler, W.; Murray, C. B. *J. Am. Chem. Soc.* **2005,** *127*, 7140-7147.

(22) Fang, C.; van Huis, M. A.; Vanmaekelbergh, D. l.; Zandbergen, H. W. *ACS Nano* **2009,** *4*, 211-218.

(23) Klokkenburg, M.; Houtepen, A. J.; Koole, R.; de Folter, J. W. J.; Erné, B. H.; van Faassen, E.; Vanmaekelbergh, D. *Nano Lett.* **2007,** *7*, 2931-2936.

(24) Talapin, D. V.; Shevchenko, E. V.; Murray, C. B.; Titov, A. V.; Král, P. *Nano Lett.* **2007,** *7*, 1213-1219.

(25) Bolhuis, P. G.; Frenkel, D.; Mau, S.-C.; Huse, D. A. *Nature* **1997,** *388*, 235-236.

(26) Norris, D. J.; Arlinghaus, E. G.; Meng, L.; Heiny, R.; Scriven, L. E. *Adv. Mater.* **2004,** *16*, 1393-1399.

(27) Querejeta-Fernández, A.; Hernández-Garrido, J. C.; Yang, H.; Zhou, Y.; Varela, A.; Parras, M.; Calvino-Gámez, J. J.; González-Calbet, J. M.; Green, P. F.; Kotov, N. A. *ACS Nano* **2012,** *6*, 3800-3812.

(28) Tang, Z.; Kotov, N. A.; Giersig, M. *Science* **2002,** *297*, 237-240.

(29) Pradhan, N.; Xu, H.; Peng, X. *Nano Lett.* **2006,** *6*, 720-724.

(30) Liao, H.-G.; Cui, L.; Whitelam, S.; Zheng, H. *Science* **2012,** *336*, 1011-1014.

(31) Li, Z.; Geßner, A.; Richters, J.-P.; Kalden, J.; Voss, T.; Kübel, C.; Taubert, A. *Adv. Mater.* **2008,** *20*, 1279-1285.

(32) Mo, M. S.; Lim, S. H.; Mai, Y. W.; Zheng, R. K.; Ringer, S. P. *Adv. Mater.* **2008,** *20*, 339-342.

(33) Liu, Z.; Wen, X. D.; Wu, X. L.; Gao, Y. J.; Chen, H. T.; Zhu, J.; Chu, P. K. *J. Am. Chem. Soc.* **2009,** *131*, 9405-9412.

(34) Sun, S.; Zhang, X.; Zhang, J.; Song, X.; Yang, Z. *Cryst. Growth Des.* **2012,** *12*, 2411-2418.

(35) Ma, Y.; Cölfeh, H.; Antonietti, M. *J. Phys. Chem. B* **2006,** *110*, 10822-10828.

(36) Medina, D. D.; Mastai, Y. *Cryst. Growth Des.* **2008,** *8*, 3646-3651.

(37) Hod, I.; Mastai, Y.; Medina, D. D. *CrystEngComm* **2011,** *13*, 502-509.

(38) Simon, P.; Rosseeva, E.; Buder, J.; Carrillo-Cabrera, W. G.; Kniep, R. *Adv. Funct. Mater.* **2009,** *19*, 3596-3603.

(39) Simon, P.; Zahn, D.; Lichte, H.; Kniep, R. *Angew. Chem. Int. Ed.* **2006,** *45*, 1911-1915.

(40) Bazylinski, D. A.; Frankel, R. B. *Nat Rev Micro* **2004,** *2*, 217-230.

(41) Li, L.; Yang, Y.; Ding, J.; Xue, J. *Chem. Mater.* **2010,** *22*, 3183-3191.

(42) Rogach, A. L.; Talapin, D. V.; Shevchenko, E. V.; Kornowski, A.; Haase, M.; Weller, H. *Adv. Funct. Mater.* **2002,** *12*, 653-664.

(43) Yao, R.; Cao, C. *RSC Advances* **2012,** *2*, 1979-1985.

(44) Ryan, K. M.; Mastroianni, A.; Stancil, K. A.; Liu, H.; Alivisatos, A. P. *Nano Lett.* **2006,** *6*, 1479-1482.

(45) Gupta, S.; Zhang, Q.; Emrick, T.; Russell, T. P. *Nano Lett.* **2006,** *6*, 2066-2069.

(46) Lausser, C.; Zahn, D.; Cölfen, H. *J. Mater. Chem.* **2011,** *21*, 16978-16982.

(47) Ahniyaz, A.; Sakamoto, Y.; Bergström, L. *Proceedings of the National Academy of Sciences* **2007,** *104*, 17570-17574.

(48) Balela, M. D. L.; Yagi, S.; Matsubara, E. *Electrochem. Solid-State Lett.* **2011,** *14*, D68-D71.

(49) Soumare, Y.; Dakhlaoui-Omrani, A.; Schoenstein, F.; Mercone, S.; Viau, G.; Jouini, N. *Solid State Commun.* **2011,** *151*, 284-288.

(50) Kimura, T.; Kimura, F.; Yoshino, M. *Langmuir* **2006,** *22*, 3464-3466.

(51) Matsumoto, K.; Kimura, F.; Tsukui, S.; Kimura, T. *Cryst. Growth Des.* **2011,** *11*, 945-948.

(52) Kimura, F.; Mizutani, K.; Mikami, B.; Kimura, T. *Cryst. Growth Des.* **2010,** *11*, 12-15.

(53) Dey, A.; Bomans, P. H. H.; Müller, F. A.; Will, J.; Frederik, P. M.; de With, G.; Sommerdijk, N. A. J. M. *Nat Mater* **2010,** *9*, 1010-1014.

(54) Almora-Barrios, N.; De Leeuw, N. H. *Cryst. Growth Des.* **2011,** *12*, 756-763.

(55) Gehrke, N.; Nassif, N.; Pinna, N.; Antonietti, M.; Gupta, H. S.; Cölfen, H. *Chem. Mater.* **2005,** *17*, 6514-6516.

(56) GRASSMANN, O.; NEDER, R. B.; PUTNIS, A.; LÖBMANN, P. *Am.*

Mineral. **2003,** *88*, 647-652.

(57) Oaki, Y.; Kotachi, A.; Miura, T.; Imai, H. *Adv. Funct. Mater.* **2006,** *16*, 1633-1639.

(58) Miura, T.; Kotachi, A.; Oaki, Y.; Imai, H. *Cryst. Growth Des.* **2006,** *6*, 612-615.

(59) Zhou, L.; Smyth-Boyle, D.; O'Brien, P. *J. Am. Chem. Soc.* **2008,** *130*, 1309-1320.

(60) Zhou, L.; O'Brien, P. *Phys. Status Solidi A* **2008,** *205*, 2317-2323.

(61) Wang, Z.; Huang, B.; Dai, Y.; Zhang, X.; Qin, X.; Li, Z.; Zheng, Z.; Cheng, H.; Guo, L. *CrystEngComm* **2012,** *14*, 4578-4581.

(62) Zhou, L.; Boyle, D. S.; O'Brien, P. *Chem. Commun.* **2007**, 144-146.

(63) Lee, M. K.; Shih, T. H. *J. Phys. D: Appl. Phys.* **2010,** *43*, 025402.

(64) Yu, H.; Tian, B.; Zhang, J. *Chem.-Eur. J.* **2011,** *17*, 5499-5502.

(65) Feng, J.; Yin, M.; Wang, Z.; Yan, S.; Wan, L.; Li, Z.; Zou, Z. *CrystEngComm* **2010,** *12*, 3425-3429.

(66) Zhou, L.; Boyle, D. S.; O'Brien, P. *Chem. Commun.* **2007**, 144-146.

(67) Sengupta, A. K.; Adhikari, S. K.; Dasgupta, H. S. *Journal of Inorganic and Nuclear Chemistry* **1979,** *41*, 161-164.

(68) Patarin, J.; Marcuccilli-Hoffner, F.; Kessler, H.; Daniels, P. *European Journal of Solid State and Inorganic Chemistry* **1994,** *31*, 501-511.

(69) Laptash, N. M.; Merkulov, E. B.; Maslennikova, I. G. *Journal of Thermal Analysis and Calorimetry* **2001,** *63*, 197-204.

(70) Laptash, N. M.; Maslennikova, I. G.; Kaidalova, T. A. *Journal of Fluorine Chemistry* **1999,** *99*, 133-137.

(71) Laptash, N. M.; Fedotov, M. A.; Maslennikova, I. G. *Journal of Structural Chemistry* **2004,** *45*, 74-82.

(72) Schmitt, R. H.; Grove, E. L.; Brown, R. D. *J. Am. Chem. Soc.* **1960,** *82*, 5292-5295.

(73) Masuda, Y.; Sugiyama, T.; Seo, W. S.; Koumoto, K. *Chemistry of Materials* **2003,** *15*, 2469-2476.

(74) Masuda, Y.; Kato, K. *Thin Solid Films* **2008,** *516*, 2547-2552.

(75) Deki, S.; Aoi, Y.; Hiroi, O.; Kajinami, A. *Chem. Lett.* **1996,** *6*, 433-434.

(76) Masuda, Y.; Ohji, T.; Kato, K. *Crystal Growth and Design* **2010,** *10*, 913-922.

(77) Herman, A.; Addadi, L.; Weiner, S. *Nature* **1988,** *331*, 546-548.

(78) Yu, S.-H.; Cölfen, H.; Antonietti, M. *J. Phys. Chem. B* **2003,** *107*, 7396-7405.

(79) Li, J.; Zeng, H. C. *J. Am. Chem. Soc.* **2007,** *129*, 15839-15847.

(80) Tao, J.; Jiang, W.; Zhai, H.; Pan, H.; Xu, X.; Tang, R. *Cryst. Growth Des.* **2008,** *8*, 2227-2234.

(81) Soare, L. C.; Bowen, P.; Lemaitre, J.; Hofmann, H. *J. Phys. Chem. B* **2006,** *110*, 17763-17771.

(82) Li, F.; Ding, Y.; Gao, P.; Xin, X.; Wang, Z. L. *Angew. Chem. Int. Ed.* **2004,** *43*, 5238-5242.

(83) Penn, R. L.; Banfield, J. F. *Science* **1998,** *281*, 969-971.

(84) Chernyshov, B. N.; Shchetinina, G. P.; Kolzunov, V. A.; Ippolitov, E. G. *Russian Journal of Inorganic Chemistry* **1980,** *25*, 1468-1474.

(85) Snyder, R. C.; Doherty, M. F. *AlChE J.* **2007,** *53*, 1337-1348.

(86) Lasaga, A. C.; Luttge, A. *Science* **2001,** *291*, 2400-2404.

(87) Liang, Y.; Baer, D. R. *Surf. Sci.* **1997,** *373*, 275-287.

(88) Cölfen, H.; Antonietti, M. *Mesocrystals and Nonclassical Crystallization*. John Wiley & Sons Ltd: Chichester, UK, 2008; pp 240.

(89) Lausser, C.; Cölfen, H.; Antonietti, M. *ACS Nano* **2011,** *5*, 107-114.

(90) Stuart, B. H. *Infrared Spectroscopy: Fundamentals and Applications*. John Wiley & Sons Ltd: New York, USA, 2004; pp 96-97.

(91) Wu, H. B.; Chan, M. N.; Chan, C. K. *Aerosol Sci. Technol.* **2007,** *41*, 581-588.

(92) Okuda, J.; Herdtweck, E. *Inorg. Chem.* **1991,** *30*, 1516-1520.

(93) Shao, G. S.; Zhang, X. J.; Yuan, Z. Y. *Appl. Catal., B* **2008,** *82*, 208-218.

(94) Zhang, J.-Y.; Boyd, I. W.; O'Sullivan, B. J.; Hurley, P. K.; Kelly, P. V.; Sénateur, J. P. *J. Non-Cryst. Solids* **2002,** *303*, 134-138.

(95) Ding, Z.; Lu, G. Q.; Greenfield, P. F. *J. Phys. Chem. B* **2000,** *104*, 4815-4820.

(96) Baglio, V.; Ornelas, R.; Matteucci, F.; Martina, F.; Ciccarella, G.; Zama, I.; Arriaga, L. G.; Antonucci, V.; Aricò, A. S. *Fuel Cells* **2009,** *9*, 247-252.

(97) Delgado, A. V. *Interfacial electrokinetics and electrophoresis*. Marcel Dekker: New York, USA, 2002; Vol. 106, pp 750.

(98) Marek, K. *J. Colloid Interface Sci.* **2004,** *275*, 214-224.

(99) Malvern. Zeta Potential Characterisation of Concentrated Lipid Emulsions. http://www.malvern.com/malvern/kbase.nsf/allbyno/KB002399/$file/MRK1383-01.pdf (accessed Dec 13, 2011).

(100) Delgado, A. V. *Interfacial electrokinetics and electrophoresis*. Marcel Dekker: New York, USA, 2002; Vol. 106, pp 785.

(101) Miller, N. P.; Berg, J. C. *Colloids Surf.* **1991,** *59*, 119-128.

(102) Kavanagh, B. V.; Posner, A. M.; Quirk, J. P. *Faraday Discuss. Chem. Soc.* **1975,** *59*, 242-249.

(103) Iruthayaraj, J.; Poptoshev, E.; Vareikis, A.; Makuška, R.; Van Der Wal, A.; Claesson, P. M. *Macromolecules* **2005,** *38*, 6152-6160.

(104) Rubio, J.; Kitchener, J. A. *J. Colloid Interface Sci.* **1976,** *57*, 132-142.

(105) Wang, Q.; Chen, C.; Zhao, D.; Ma, W.; Zhao, J. *Langmuir* **2008,** *24*, 7338-7345.

(106) Suwanchawalit, C.; Patil, A. J.; Kumar, R. K.; Wongnawa, S.; Mann, S. *J. Mater. Chem.* **2009,** *19*, 8478-8483.

(107) Stylidi, M.; Kondarides, D. I.; Verykios, X. E. *Int. J. Photoenergy* **2003,** *5*, 59-67.

(108) Betianu, C.; Caliman, F. A.; Gavrilescu, M.; Cretescu, I.; Cojocaru, C.; Poulios, I. *J. Chem. Technol. Biotechnol.* **2008,** *83*, 1454-1465.

(109) Park, H.; Choi, W. *J. Phys. Chem. B* **2004,** *108*, 4086-4093.

(110) Yu, J.; Wang, W.; Cheng, B.; Su, B.-L. *J. Phys. Chem. C* **2009,** *113*, 6743-6750.

(111) Han, X.; Kuang, Q.; Jin, M.; Xie, Z.; Zheng, L. *J. Am. Chem. Soc.* **2009,** *131*, 3152-3153.

(112) Liu, S.; Yu, J.; Jaroniec, M. *Chem. Mater.* **2011,** *23*, 4085-4093.

(113) Maitani, M. M.; Tanaka, K.; Mochizuki, D.; Wada, Y. *J. Phys. Chem. Lett.* **2011,** *2*, 2655-2659.

(114) Yu, J.; Qi, L.; Jaroniec, M. *J. Phys. Chem. C* **2010,** *114*, 13118-13125.

(115) Yang, H. G.; Sun, C. H.; Qiao, S. Z.; Zou, J.; Liu, G.; Smith, S. C.; Cheng, H.

M.; Lu, G. Q. *Nature* **2008,** *453*, 638-641.

(116) Lee, M. K.; Shih, T. H.; Shih, C. M. *IEEE T. Nanotechnol.* **2007,** *6*, 316-319.

(117) Liu, G.; Sun, C.; Yang, H. G.; Smith, S. C.; Wang, L.; Lu, G. Q.; Cheng, H. M. *Chem. Commun.* **2010,** *46*, 755-757.

(118) Zheng, Z.; Huang, B.; Qin, X.; Zhang, X.; Dai, Y.; Jiang, M.; Wang, P.; Whangbo, M. H. *Chem.-Eur. J.* **2009,** *15*, 12576-12579.

(119) Zhang, D.; Li, G.; Wang, H.; Chan, K. M.; Yu, J. C. *Cryst. Growth Des.* **2010,** *10*, 1130-1137.

(120) Fang, W. Q.; Gong, X. Q.; Yang, H. G. *J. Phys. Chem. Lett.* **2011,** *2*, 725-734.

(121) Yang, W.; Li, J.; Wang, Y.; Zhu, F.; Shi, W.; Wan, F.; Xu, D. *Chem. Commun.* **2011,** *47*, 1809-1811.

(122) Yu, J.; Fan, J.; Lv, K. *Nanoscale* **2010,** *2*, 2144-2149.

(123) Zhang, H.; Han, Y.; Liu, X.; Liu, P.; Yu, H.; Zhang, S.; Yao, X.; Zhao, H. *Chem. Commun.* **2010,** *46*, 8395-8397.

(124) Chen, J. S.; Luan, D.; Li, C. M.; Boey, F. Y. C.; Qiao, S.; Lou, X. W. *Chem. Commun.* **2010,** *46*, 8252-8254.

(125) Sasidharan, M.; Nakashima, K.; Gunawardhana, N.; Yokoi, T.; Inoue, M.; Yusa, S.-i.; Yoshio, M.; Tatsumi, T. *Chem. Commun.* **2011,** *47*, 6921-6923.

(126) Sun, C. H.; Yang, X. H.; Chen, J. S.; Li, Z.; Lou, X. W.; Li, C.; Smith, S. C.; Lu, G. Q.; Yang, H. G. *Chem. Commun.* **2010,** *46*, 6129-6131.

(127) Song, R. Q.; Cölfen, H. *CrystEngComm* **2011,** *13*, 1249-1276.

(128) Napper, D. H. *Polymeric stabilization of colloidal dispersions*. Academic Press: London, 1983; pp 8-15.

(129) Wiśniewska, M. *J. Dispersion Sci. Technol.* **2011,** *32*, 1605-1623.

(130) Alexandridis, P.; Holzwarth, J. F.; Hatton, T. A. *Macromolecules* **1994,** *27*, 2414-2425.

(131) Myers, D. *Surfaces, Interfaces, and Colloids: Principles and Applications*. John Wiley & Sons: New York, 1999; pp 366.

(132) Alexandridis, P.; Hatton, T. A. *Colloids and Surfaces. A, Physicochemical and Engineering Aspects* **1995,** *96*, 1-46.

(133) Wanka, G.; Hoffmann, H.; Ulbricht, W. *Macromolecules* **1994,** *27*, 4145-4159.

(134) Kurumada, K.-i.; Robinson, B. *Prog. Colloid Polym. Sci.* **2004,** *123*, 12-15.

(135) Park, Y.; Whitaker, R. D.; Nap, R. J.; Paulsen, J. L.; Mathiyazhagan, V.; Doerrer, L. H.; Song, Y.-Q.; Hürlimann, M. D.; Szleifer, I.; Wong, J. Y. *Langmuir* **2012,** *28*, 6246-6255.

(136) Ba, J.; Feldhoff, A.; Fattakhova Rohlfing, D.; Wark, M.; Antonietti, M.; Niederberger, M. *Small* **2007,** *3*, 310-317.

(137) Lin, Y.; Alexandridis, P. *J. Phys. Chem. B* **2002,** *106*, 10834-10844.

(138) Soler-Illia, G. J. d. A. A.; Sanchez, C. *New J. Chem.* **2000,** *24*, 493-499.

(139) Killmann, E.; Maier, H.; Baker, J. A. *Colloids Surf.* **1988,** *31*, 51-71.

(140) Malmsten, M.; Linse, P.; Cosgrove, T. *Macromolecules* **1992,** *25*, 2474-2481.

(141)Nejadnik, M. R.; Olsson, A. L. J.; Sharma, P. K.; van der Mei, H. C.; Norde, W.; Busscher, H. J. *Langmuir* **2009,** *25*, 6245-6249.

(142) Zhang, X.; Zhang, Z.; Glotzer, S. C. *J. Phys. Chem. C* **2007,** *111*, 4132-4137.

(143) Tang, Z.; Zhang, Z.; Wang, Y.; Glotzer, S. C.; Kotov, N. A. *Science* **2006,** *314*, 274-278.

(144) Li, D.; Nielsen, M. H.; Lee, J. R. I.; Frandsen, C.; Banfield, J. F.; De Yoreo, J. J. *Science* **2012,** *336*, 1014-1018.

(145) Wohlrab, S.; Pinna, N.; Antonietti, M.; Cölfen, H. *Chemistry – A European Journal* **2005,** *11*, 2903-2913.

(146) Withers, R. L.; Brink, F. J.; Liu, Y.; Norén, L. *Polyhedron* **2007,** *26*, 290-299.

(147) Atuchin, V. V.; Gavrilova, T. A.; Kesler, V. G.; Molokeev, M. S.; Aleksandrov, K. S. *Chem. Phys. Lett.* **2010,** *493*, 83-86.

(148) Atuchin, V. V.; Gavrilova, T. A.; Kesler, V. G.; Molokeev, M. S.; Aleksandrov, K. S. *Solid State Commun.* **2010,** *150*, 2085-2088.

(149) KE, Q.; LU, W.; HUANG, X.; WANG, J. *J. Electrochem. Soc.* **2012,** *159*, G1-G4.

(150) Perdew, J. P.; Burke, K.; Ernzerhof, M. *Phys. Rev. Lett.* **1996,** *77*, 3865-3868.

(151) Perdew, J. P.; Burke, K.; Ernzerhof, M. *Phys. Rev. Lett.* **1998,** *80*, 891-891.

(152) Kresse, G.; Furthmüller, J. *Computational Materials Science* **1996,** *6*, 15-50.

(153) Blöchl, P. E. *Physical Review B* **1994,** *50*, 17953-17979.

(154) Kresse, G.; Joubert, D. *Physical Review B* **1999,** *59*, 1758-1775.

(155) Gonze, X.; Allan, D. C.; Teter, M. P. *Phys. Rev. Lett.* **1992,** *68*, 3603-3606.

(156) Baroni, S.; Resta, R. *Physical Review B* **1986,** *33*, 7017-7021.

(157) Brown, I. D. *Acta Crystallographica Section B* **1992,** *48*, 553-572.

(158) Kalinin, S. V.; Rodriguez, B. J.; Jesse, S.; Maksymovych, P.; Seal, K.; Nikiforov, M.; Baddorf, A. P.; Kholkin, A. L.; Proksch, R. *Mater. Today* **2008,** *11*, 16-27.

(159) Herng, T. S.; Wong, M. F.; Qi, D.; Yi, J.; Kumar, A.; Huang, A.; Kartawidjaja, F. C.; Smadici, S.; Abbamonte, P.; Sánchez-Hanke, C.; Shannigrahi, S.; Xue, J. M.; Wang, J.; Feng, Y. P.; Rusydi, A.; Zeng, K.; Ding, J. *Adv. Mater.* **2011,** *23*, 1635-1640.

(160) Zavaliche, F.; R. Das, R.; Kim, D. M.; Eom, C. B.; Yang, S. Y.; Shafer, P.; Ramesh, R. *Appl. Phys. Lett.* **2005,** *87*, 182912-3.